The Effects of Agitation on Convective Heat Transfer with Applications to Electronics Cooling

A DISSERTATION
SUBMITTED TO THE FACULTY OF
UNIVERSITY OF MINNESOTA
BY

SMITA AGRAWAL

IN PARTIAL FULFILLMENT OF THE REQUIREMENTS
FOR THE DEGREE OF
DOCTOR OF PHILOSOPHY

ADVISER: TERRENCE W. SIMON, CO-ADVISER: TIANHONG CUI

JANUARY, 2014

Acknowledgements

I would like to thank DARPA for funding this project. I would also like to thank Thermacore for their support during this project.

It was a great learning experience as a student at the University of Minnesota working with Dr. T.W. Simon. Regular discussions with Dr. Simon related to experiment design, fabrication, data collection and analysis helped me a lot in enhancing my knowledge in the field of heat transfer and fluid mechanics. Dr. Simon's patience in discussing issues related to my research taught me the importance of being patient and perseverant while carrying out experiments and data analysis. I would also like to thank Dr. T. Cui for his comments which were valuable for research progress.

Working on the DARPA MACE electronics cooling project required a team of efficient and capable students and post doctoral fellows. I thank Taiho Yeom, Longzhong Huang, Youmin Yu, Min Zhang, Congshun Wang, Xuelin Zhu, Tao Zhang who were a part of this team and provided valuable ideas for the project.

The agitator mock up experiment facility required great machining expertise which would not have been possible without the knowledge and skills of machinist Robin Russell. He was always present to help me with his valuable suggestions. It was a great learning experience working with him. Dave Hultman in the machine shop was always more than ready to help with the experiment facility fabrication process. I thank him for his constant support.

I would like to thank my family. They have always been a constant pillar of support for me. Their trust in my capabilities has always given me the courage to follow my dreams and be patient in difficult times. It would not have been possible to complete my education, had I not got the support of my father , my mother, my brother Nishant and my husband Praveen.

I thank my friends Shachi, Richa, Tanushree, Reetu, Lesley, Aditi, Pulkit, Caroline, Anh, Neha, Gysler, Madhura, Meenakshi, Rohini, Pradeep, Ranga, Venkat, Thaseem and Prahladh for giving me company during this phase and making it an enjoyable one.

Smita Agrawal

Abstract

With continuously increasing number of chips and smaller and smaller CPU sizes, heat fluxes that need to be dissipated from computers are on a rapid increase. CPU cooling being critical to the performance of electronic devices, this field demands considerable research focus. Researchers have been pushing existing computer cooling technologies to their limits and also developing new cooling techniques. Forced convection, spray jet cooling, boiling heat transfer are a few to name. Different technologies have their respective merits and limits in terms of their cooling capability, reliability, ease of manufacturing and durability. Forced convection using air has always been preferred due to its cost effectiveness and reliability. The traditional way of employing this technique has been by using a blower fan that cools the heat sink that dissipates heat from the chips. However, the current heat removal demands better performance than that can be provided by a blower fan alone.

Thus, a lot of research effort is being expended to push the air cooling technology further by developing methods that can either assist the blower fan or replace it. The current research work is an effort in the same direction. The channels of a heat sink are being cooled by translationally oscillating plates called agitators in conjunction with a throughflow fan. The idea is to vigorously agitate the flow in the cavity for better heat removal from the channel walls.

Agitation is a strong mixing mechanism that can disturb the near-wall flow, thin the thermal boundary layer and enhance the convective heat transfer. This thesis study carries a detailed study of agitation alone through a Large Scale Mock Up (LSMU) unit which is dynamically similar to a single channel of a heat sink. The LSMU has a translationally oscillating plate (agitator) inside the channel cavity. Time averaged heat transfer coefficients and time resolved velocity measurements have been made along different regions of the channel to characterize the convective cooling performance of the agitator. The ensemble-averaged mean velocity variations show periods of acceleration, deceleration and flow reversal during a cycle as a result of agitator movement. Turbulence is found to increase toward the end of the acceleration phase and persist through the deceleration phase. A parametric study has been done to explore the effects of agitator frequency (f), amplitude (A) and agitation velocity ($2\pi Af$) on heat transfer and flow mechanism. The heat transfer coefficient increases with the increase in frequency and amplitude. At a fixed agitation velocity, heat transfer coefficient is mainly governed by the agitation velocity irrespective of the value of amplitude or frequency.

Measurements have been made for channel surfaces augmented with cylindrical pin fins. An increase of 4-5%, based on total wetted area, was found in heat transfer coefficient, generally, when the pin fins were introduced. The change varied widely from one region to the next. A detailed parametric study was also done with the pin fin case.

An attempt to model the measured heat transfer coefficient and velocity has been made. A single predictor using the measured velocity has been used to model the measured heat transfer coefficient. The model performance varies along the different regions of the channel.

Simulations were done using ANSYS FLUENT to help design an efficient heat sink. Keeping the overall heat sink geometry fixed, the effect of channel width was explored. Heat sinks having narrower channels have a greater number of channels in total for the fixed size of heat sink and therefore greater heat transfer area than heat sinks with wider channels. This study helped in the design of an optimum heat sink using agitation. The power consumed to drive the agitators was also computed. An optimum geometry based on the thermal resistance and agitator power consumption was proposed.

Table of Contents

List of Tables

List of Figures

Nomenclature

Chapter 2

u	:velocity (equation 2-1) (m/s)
t	:time (equation 2-1) (s)
p	:pressure (equation 2-1) (N/m^2)
ρ	:density (equation 2-1) (kg/m^3)
u^*	:nondimensional velocity (equation 2-2)
p^*	:nondimensional pressure (equation 2-2)
ν	:kinematic viscosity (m^2/s)
f	:characteristic frequency used for specifying characteristic time (equation 2-2) (Hz)
L	:characteristic length scale (equation 2-2)(m)
U	:characteristic velocity (equation 2-2)(m/s)
Re	:Reynolds number
Va	:Valensi number
C_p	:specific heat capacity (J/kg.K)
T	:temperature (equation 2-5) (K)
k	:thermal conductivity (W/mK)
μ	:viscosity (kg/s.m)
Φ	:viscous dissipation (equation 2-5) (J/m^2kg)
Φ^*	:non dimensional viscous dissipation (equation 2-6)
Pr	:Prandtl number
Ec	:Eckert number
T_s	:surface temperature (equation 2-8, 2-9, 2-13) (K)
T_{sink}	:sink temperature (equation 2-8 , 2-9, 2-13) (K)
q_w	:heat flux at the wall (equation 2-9) (W/m^2)
y	:wall normal direction (equation 2-9) (m)
h	:heat transfer coefficient (equation 2-9 and 2-13) (W/m^2K)
Nu	:Nusselt number (equation 2-10)
T^*	:non dimensional temperature (equation 2-6 and 2-10)
t^*	:dimensionless time scale (equation 2-6)
y^*	:non dimensional length scale (equation 2-10)
u_{max}	:maximum agitator velocity, characteristic velocity for dimensional similitude (equation 2-11) (m/s)
£	:agitator to fin maximum distance, characteristic length for dimensional similitude (equations 2-11 and 2-12) (m)
ω	:agitator frequency (equation 2-12) (radian)
A_a	:amplitude of the agitator (mean-to-peak) (m)
f_a	:agitator frequency (Hz)
V	:measured voltage difference (equation 2-13) (V)
I	:current flowing in the heater (equation 2-13) (A)
A	:area of copper plate (equation 2-13) (m^2)

Q	:heat flux (equation 2-14) (W/m^2)
T_p	:temperature of copper plate (equation 2-14) (K)
T_{ns}	:near surface temperature (equation 2-14) (K)
Q_{steady}	:measured time averaged steady state heat flux (equation 2-15) (W/m^2)
c	:constant to calculate unsteady state heat flux (equation 2-15, 2-16)
Q_t	:instantaneous heat flux (equation 2-16) (W/m^2)
$U_i(t)$	:velocity at time, t, for cycle, i (equation 2-17) (m/s)
$U_{mean}(t)$	:ensemble-averaged mean velocity at time t (equation 2-17) (m/s)
$U'_{RMS}(t)$	: ensemble-averaged RMS fluctuating velocity at time t (equation 2-18) (m/s)
P	:power supplied to the heater (equation 2-19 and 2-20) (W)
$Q_{net,in}$	:total power inflow from neighboring copper plates (equation 2-17 and 2-21) (W)
Q_i	:heat flow from adjacent copper plate (equation 2-21 and 2-22) (W)
T_i	:temperature of neighboring copper plate (equation 2-22) (K)
T_c	:temperature of copper plate in consideration while calculating the heat flow from adjacent plates (equation 2-22) (K)
R	:thermal resistance between two copper plates (equation 2-22) (K/W)

Chapter 5

u'	:fluctuating velocity signifying turbulence level (equation 5-1) (m/s)
St'	:Stanton number in Maciejewski correlation (55,56) based on u' predictor (equation 5-1)
h	:heat transfer coefficient (equation 5-1) (W/m^2K)
ρ	:density (equation 5-1) (kg/m^3)
C_p	:specific heat capacity (equation 5-1) (kJ/kgK)
u_{max}	:maximum standard deviation in the streamwise component of velocity (equation 5-2) (m/s)
$U_{t,i}$	:velocity at time t for cycle i (equation 5-3, 5-4) (m/s)
$U_{mean}(t)$	:ensemble-averaged mean velocity at time t (equation 5-3) (m/s)
$U'_{RMS}(t)$	:ensemble-averaged RMS fluctuating velocity at time t (equation 5-4) (m/s)
Tu(t)	:turbulence intensity at time t (equation 5-5)
$U_{mean,RMS}$	:RMS variation of the mean velocity (equation 5-6) (m/s)
$U'_{RMS,avg}$	:average fluctuating velocity during a cycle (equation 5-6) (m/s)
Tu	:turbulence intensity (equation 5-5)

Chapter 6

A_{single}	:area of fin surface (equation 6-1) (mm^2)
$A_{agitator}$	:area of agitator surface (equation 6-3) (mm^2)
A_{total}	:total heat sink area (equation 6-5) (mm^2)
a	:operational amplitude of actuated plate (equation 6-4)(mm)
COP	:Coefficient of Performance (equation 6-6)
f	:vibrating frequency (equation 6-4) (Hz)

H	:fin height (mm)
h_{single}	:heat transfer coefficient for single channel (equation 6-1) (W/m^2k)
L	:channel length (mm)
p	:pressure (equation 6-3) (Pa)
P	:thermal power or fluid power (equation 6-3) (W)
q	:heat transfer rate (equation 6-1) (W)
R_{th}	:thermal resistance (equation 6-5) (K/W)
t	:agitator thickness (mm)
T	:temperature (equation 6-2) (K)
V	:agitator velocity (equation 6-3) (m/s)
W	:channel width (mm)
W_{fin}	:fin thickness (mm)
$P_{thermal}$	:thermal power removed from heat sink (equation 6-6) (W)
$P_{agitator}$	:power needed to drive agitator assembly (equation 6-6) (W)
k	:turbulence kinetic energy (mean kinetic energy per unit mass associated with eddies in turbulent flow, m^2/s^2)
ΔT	:channel log mean temperature difference (equation 6-2) (K)
δ_{min}	:minimum gap (mm)
δ_{tip}	:tip gap (mm)
θ	:cycle time (s)

Subscripts in Chapter 6

air_in	:channel inlet air
air_out	:channel outlet air
avg	:average
channel_in	:channel in the inlet region
channel_out	:channel in the outlet region

Chapter 1

Introduction

1.1 Review

1.1.1 Different Cooling Technologies for Electronics

There has been an exponential increase with successive generations in the number of transistors on a single chip. According to Moore, the number of transistors on a chip doubles every 2 years [1]. As the speed of operation and density of transistors increase, dissipation of heat from the chip rises, demanding continued attention. Without continued advancements in accommodating thermal dissipation, processing speed and reliability will be jeopardized. Thermal designers have traditionally used conventional fans to cool heat sink fin arrays that dissipate heat from chips in electronic devices. Considerable work has been done to improve cooling performance using blower fans. Various other cooling techniques have been developed and were in the process of improvement over the past decades to cope with the demand for more and more dissipation of heat over smaller CPU sizes. Devices such as high performance supercomputers and some military applications have heat dissipation requirements in the range 100-1000W/m^2K. An assessment of high heat flux cooling technologies was carried out by Mudawar [2]. Forced convection using air, liquid cooling, boiling, sprays, jet-impingement, microchannel and minichannel heat sinks are to name a few. Different cooling schemes have their respective merits and demerits depending on their cooling capabilities, ease of packaging, cost effectiveness and reliability. A cooling scheme could be chosen for a specific application depending on which of the above factors are critical to the

application. Agostini et al. [3] discussed developments in various cooling technologies over the last few decades. They reported high performance of impinging jets and the promise shown by two phase boiling in microchannels as a cooling technique for chips. Mahajan [4] discussed the current chip cooling requirements and challenges followed by improvements that can be made by better power management at the chip, cooling at package level, heat sink design and system level cooling. The advantages and disadvantages of various cooling technologies like enhanced convection, advanced spreader materials, liquid cooling and refrigeration were discussed. Though other technologies could provide better thermal performance, air cooling is still one of the most preferred as far as simple implementation and reliability are concerned. Most of the other cooling technologies were limited by cost effectiveness and reliability. Chu [5] carried out a review of various projects sponsored by IBM for electronics cooling. The review included different modes of cooling, like forced convection air cooling, liquid forced convection, pool boiling, falling films, flow boiling and liquid jet impingement.

1.1.2 Liquid Cooling

Liquid cooling has emerged as an effective cooling technology due to its high heat flux removal capability. IBM has employed hybrid air to water cooling or indirect water cooling for its large server systems [6, 7]. Liquid cooling using microchannels can remove high heat fluxes but requires tremendous pumping power. The average heat flux cooled by microchannel heat sinks with water is about 300 W/cm^2. However, due to reliability issues, manufacturers have concern over placing liquid loops directly inside the servers [3]. Prasher et al. [8] were able to cool high heat flux hotspots using single phase microchannel cooling, thus, obtaining low thermal resistances. However, they noted one

of the limitations of this technology being the high freezing point of water (0 °C). The freezing limit specified by electronics industry is -40 °C. This requires use of an antifreeze or a liquid mixture that can lower the freezing point. Naphon et al. [9] experimentally studied the heat transfer performance and pressure drop in microchannels with different geometries. They found that the microchannel geometry was a significant parameter in affecting heat transfer performance and pressure drop. Xie et al. [10] numerically investigated heat transfer performance that can be obtained in minichannels using water. They optimized the geometry of the channel in order to reduce pressure loss. They found that a narrow and deep channel gave good cooling performance that could cool a chip with a heat flux of 350 W/cm^2 with a pressure drop that is still high, but acceptable.

1.1.3 Phase Change Cooling

Phase change cooling with boiling is a very attractive cooling technology due to its high heat dissipation rates. However, the implementation of this technique is complicated and costly in comparison to other cooling techniques. Flow instabilities and accurate prediction of critical heat flux still remain challenges with this cooling technique. Much research effort is being put into addressing these issues and making this method more reliable [2, 3]. Thome [11] carried out a detailed study of boiling and two phase flows in microchannels. Emphasis was made on much research work to be done to better understand flow instability, flow-induced fluctuations and gather more critical heat flux data for accurate prediction. A need to develop more models to take into account the effects of non circular channel geometry and fluid properties was also noted. Bowers et al. [12, 13] carried out an optimization study for minichannel and microchannel heat sink

with two phase cooling. They developed a pressure model to assist in the design of heat sinks and also listed heat sink geometrical parameters that led to low thermal resistance without compromising strength of the heat sinks. Mudawar [14] carried out a detailed theoretical study of two phase flow in microchannel heat sinks listing their applications and limitations. Optimizing heat sink geometry for better heat transfer performance was listed as being more beneficial than applying proven heat transfer enhancement techniques for macro systems to microchannels. An emphasis for consolidated databases having information about critical heat flux, coolant thermophysical properties, microchannel geometries, pressure drop correlations and many more parameters critical to design of two phase flow cooling in microchannels was made in this study. They are similar to the requirements listed in some of the previous studies. A recommendation was made to employ hybrid cooling schemes that would combine merits of microchannel flow boiling and jet impingement amongst other cooling techniques.

1.1.4 Impingement Cooling

Impingement cooling is another method that has been employed for cooling of electronic devices. To attain more uniform surface temperatures, arrays of jets have been used [2, 3]. Fabbri et al. [15] carried out an optimization study for arrays of microjets using liquid cooling for high power electronics. They were able to attain a heat flux of 310 W/cm^2. Jang et al. [16] experimentally studied the fluid flow and heat transfer characteristics of a microchannel heat sink subject to an impinging jet. Under a fixed pumping power condition, they reported an enhancement of 21% for an optimized microchannel heat sink that was cooled by jets over one that was cooled by parallel flow. Sung et al. [17-19]

employed a hybrid cooling scheme using microchannel flow and impinging jets. High heat dissipation rates were reported using the hybrid dissipation scheme.

1.1.5 Heat Sink Design

Much focus has also gone on the design of heat sinks for better heat transfer performance. Fan et al. [20] proposed a cylindrical minichannel heat sink to fit over cylindrical heat sources and carried out a numerical and experimental study for fluid flow and heat transfer for such heat sinks. They found a reduction in average thermal boundary layer thickness because the periodic oblique cylindrical fin led to disruption of the hydrodynamic boundary layer. This led to an increase in heat transfer and a drop in pressure loss penalty. Egan et al. [21] carried out an experimental study for the design of finned and finless miniature heat sinks for forced convection air cooling using one of the smallest commercially available miniature fans. Due to the fan exit angle, the entering flow was not parallel to the heat sink, leading to large pressure losses. They proposed introducing a straightening diffuser which led to an increase of 20% in thermal performance. Kim et al. [22] experimentally studied fluid flow and heat transfer characteristics by introducing a cross cut on heat sink. The heat sink has several cuts called cross cuts, perpendicular to the direction of fluid flow. Under fixed pumping power and heat sink volume, they suggested an optimally designed heat sink. The performance of the optimized cross cut heat sink was found to be better than the performance of an optimized plate fin or square fin heat sink. Yang et al. [23] studied the heat transfer and pressure drop characteristics of heat sinks with plain, slit and louver fin pattern. The heat transfer performance of louver fins was found to be better than a slit fin or a plain fin, but the louver fin was accompanied by a higher pressure loss. The pressure

loss of the slit fin was comparable to that of the louver fin for certain geometries. When the fin spacing was small and the Reynolds number was lowered, a considerable drop in heat transfer performance was observed. Quinones et al. [24] proposed a new cylindrical heat sink device cooled by heat pipes having multiple heat sink assemblies and fans. Each heat sink assembly was cooled by a centrifugal fan. The heat sink could dissipate a heat flux of 125 W/cm^2. Egan et al. [25] compared the performance of small low profile heat sinks with and without fins. They tested the performance of the smallest commercially available fan with two different heat sinks. They suggested that a finless heat sink can be used when the fan is operating at low speeds while at the maximum fan speed of 8000 rpm, both provided similar performance. Also, a finless heat sink was better than a finned heat sink in terms of cost, lower acoustic levels and lesser fouling issues.

1.1.6 Piezoelectric Fans for Cooling Heat Sinks

Extensive research is being done on the thermal performance of piezoelectric fans for cooling heat sinks. Researchers have used a piezoelectric patch in a flapping mode as a replacement fan to cool finned heat sinks. Liu et al. [26] experimentally studied the heat transfer performance of horizontal and vertical arrangement of piezoelectric fans. They concluded that the heat transfer augmentation of piezofan was because of the entrained airflow during each oscillation cycle and the jet like air stream at the fan tip. They proposed a correlation applicable to vertical arrangement. Acikalin et al. [27] carried out a study to optimize and characterize the performance of miniature piezoelectric fans. They studied different parameters like fan amplitude, distance between the fan and heat source, fan length, frequency offset from resonance and fan offset from the center of the heat source to characterize the performance of the fans. They carried out a design of

experiment analysis that revealed the fan frequency offset from resonance and fan amplitude are the critical parameters. Kimber et al. [28] studied the heat transfer performance of a piezoelectric fan by placing the fan at a distance from a constant heat flux surface and varying the frequency and the distance of the fan from the surface. They found that the performance of the fan was best when the fan operated at an optimal separation distance from the heated surface. They discovered that the heat transfer performance of the fan was dependent only on the frequency and amplitude when the fan was operated at the optimal gap. They developed correlations that could predict well the thermal performance of the fan over the applied range of amplitude, frequency and fan dimensions. Kimber et al. [29] studied the heat transfer performance of arrays of piezoelectric fans in their first resonant mode. The local heat transfer coefficients were determined using infrared imaging. Parameters like vibration amplitude, fan pitch, and distance from the heat source were studied. A strong dependence of heat transfer coefficient on the fan pitch was found. Acikalin et al. [30] studied the performance of a vibrating cantilever placed near a heated surface. They carried out both a numerical and an experimental study. The flow field was visualized using the PIV technique. Numerical simulations were done using FLUENT software. The validity of the numerical results was established by comparing the flow field generated numerically with that created using PIV. The numerical results for the flow field and heat transfer were found to agree with the experimental data within 20%. Results from the numerical simulation were used to generate fan curves for the piezoelectric fans. Lin et al. [31] experimentally and numerically studied the three dimensional characteristics of a vibrating fan by considering two different configurations, horizontal and vertical. Their results displayed

the formation of two counter rotating flow circulations on either edge of the blade. Horizontal placement of the heat source showed slightly more heat transfer enhancement than vertical placement. Ma et al. [32] optimized the design of a heat sink, piezoelectric fan assembly by studying the effects of fan amplitude, frequency, fan arrangement and power consumption. An oscillating piezoelectric fan between two fins was found to disrupt the thermal boundary layer. They proposed a three dimensional transitional model for the flow field of the cooling system.

Since air cooling is preferred due to its cost effectiveness and relatively simple design, researchers have been trying to push this technology as far as possible by introducing new concepts. Some of the methods discussed earlier have been cleverly designed into heat sinks by introducing piezoelectric fans. Newer methods of disturbing the flow inside the heat sink are continuously being developed. A new design was proposed to efficiently utilize the traditionally used cooling space containing the fan and heat sink [33, 34]. The proposed scroll heat sink had rotating moving fins on a shaft integrated with the stationary cooling fins. This eliminated the need for a blower fan. Due to the movement of the rotating fins, coolant was sucked in the cavity between rotating and stationary fins. The coolant absorbed heat from the stationary fins and was discharged out of the heat sink. They also modeled the thermal resistance and pumping power for the heat sink. Under fixed pumping power, the optimized scroll heat sink was found to perform better than the optimized plate fin heat sink. Allison [35] et al. cooled a single layer of parallel plate heat exchanger using interdigitated impeller blades. This arrangement was found to perform better than conventional cooling schemes under a fixed pumping power condition.

1.1.7 Agitation for Cooling Heat Sinks

Our group's research was an effort in pushing the air cooling technology further by vigorously agitating the cavity between the heat sink fins. Oscillating plates called agitators were introduced between the channel walls to thoroughly mix the flow and break the development of thermal boundary layers. Yeom et al. [36] did experiments to test this idea for a single channel of the heat sink. They designed an oval loop shell with a piezo actuator to drive the agitator plates for translational oscillatory motion. The channel was cooled both by agitation and throughflow. Frequencies of around 1000 Hz and mm range amplitudes were achievable using this technology. They were able to observe an improvement in heat transfer rate of around 55% compared to the non agitated state. An effective Reynolds number was defined to characterize the combined effects of throughflow and agitation. They were able to predict the heat transfer performance by defining a Stanton number that used the effective Reynolds number. Yu et al. [37] numerically studied the factors influencing the heat transfer for channels cooled by translationally oscillating plates called agitators. Enhancements as high as 61% were observed. Heat transfer enhancement was found to increase with increases in amplitude and frequency. Under constant agitation velocity, which is governed by the product of amplitude and frequency, they found that heat transfer enhancement was primarily affected by the agitation velocity with amplitude being only slightly more important than frequency. Turbulence was found to be generated in the narrow gap between the channel base and the agitator plate. This turbulence was found to play a key role in flow mixing and thus increasing heat transfer. Yu et al. [38] numerically studied the heat transfer enhancement obtained when fan cooled heat sinks are assisted by active devices like

agitators and synthetics jets. This study was done for a single channel of the heat sink. An enhancement of around 80% was found when the performance was compared with the channel flow only case. In another study, Yeom et al. [39] found 91% enhancement when the throughflow cooled channel was assisted by agitation at a frequency of 1140 Hz, compared to a channel only case of 45 LPM. Yeom et al. [40] reported that a thermal resistance of 0.053 K/W could be achieved in a single channel with surface augmented with pin fins when the agitator operated at a frequency of 686 Hz and an amplitude of 1.4 mm and the cross flow velocity was 7.9 m/sec. They extended the idea to a full scale system with a 26 blade array to cool a multiple channel heat sink. Since the total blade mass was high when the single channel idea was implemented for multiple channel heat sink, a reduction in frequency was sought. To increase the frequency, they proposed using short blades. Where a long blade was mixing the flow along the entire channel length, a short blade acted as a vortex generator at the channel entry region. The vorticity generated by the short blade at the channel entry was carried downstream by cross flow. The long blade assembly had a frequency of 222 Hz. Reducing the blade length increased the operating frequency to around 800 Hz. It was found that the short blade agitator assembly operated at a higher frequency performed better than the long blade assembly at a lower frequency. Yu et al. [41] carried out a numerical study to compare the coefficient of performance when the channel was cooled by a long blade and short blade. It was found that the short blade had a better coefficient of performance compared to the long blade. The effect of agitation in a single channel of heat sink was studied in a Large Scale Mock Up unit that was dynamically similar to a single channel of the heat sink [42,43]. Agrawal et al. [42, 43] carried out detailed measurements to study the effectiveness of

agitation in mixing the flow and subsequently enhancing heat transfer along the channel wall. The study reported the effectiveness of agitation at different locations along the channel.

The objective of this thesis study is to enhance heat transfer in a large scale single channel which mimics a single channel of an electronics cooling heat sink. Factors such as frequency, amplitude, agitation velocity, surface characteristics have been studied to identify critical parameters important for heat transfer enhancement. The heat sink with agitators is shown in Figure 1.2 of Chapter 1. A single channel with the agitator is shown in Figure 1.3. The oscillating agitator plate flow and heat transfer characteristics are significantly different in different parts of the channel. The different parts of the channel are shown in Figure 2.4 of Chapter 2. Three different channel regions have been identified, namely the entry region, from where the flow enters and leaves the channel, the central region is in the center of the channel which has a straight geometry and is secluded from entry effects or any bend effects, and the base region is close to the base of the channel. The base region has a sharp 90° bend in its geometry. The base region also has a narrow gap between the agitator tip and the channel base. Time averaged heat transfer and time resolved velocity measurements have been made in each of these regions. As can be seen from the geometry description, flow characteristics are significantly different in each of the three regions, leading to different heat transfer rates. This requires a literature study of oscillating flow and heat transfer phenomena. Heat transfer literature for oscillating flow in a channel is rather scarce. This calls for study of related topics like pulsatile flows, entry flows in round channels, bend flows and turbulent heat transfer for steady and unsteady cases.

1.1.8 Heat Transfer Studies for Unsteady Flows

Bauer et al. [44] carried out steady and unsteady heat transfer studies for entry flow in a pipe for straight and curved pipe geometries that were similar to practical spark ignition engine geometries. The engine intake flow mimics half a sine wave followed by a stagnation phase that is thrice as long. Unsteadiness in the flow was found to significantly enhance heat transfer, between 50% to 100%. Time-resolved heat flux measurements showed a delay in comparison to the onset of the flow. Time–resolved, axially-averaged Nusselt numbers were correlated with Reynolds number. The stagnation phase of the flow was found to make a comparable contribution to the heat transfer as that of the pulsatile phase of the flow. This was explained by the slow decay during the stagnation phase of the turbulence generated during the pulsatile phase. Davidson and Parker [45] studied the time-averaged heat flux in the presence of fully-developed pulsatile flow by expanding the temperature as a Fourier series. The effect of pulsation frequency was studied. It was found the local heat flux was dependent on the ratio of the characteristic thermal diffusion time to the disturbance time and the average deviation in velocity from that of mean flow. Some locations were found to show an increase whereas others a decrease in heat flux when compared to the steady flow case. Jin et al. [46] studied heat transfer enhancement due to pulsatile flow agitation in a triangular grooved channel. Heat transfer enhancement was found to decrease with an increase in Reynolds number. A PIV study was done to explain the observed heat transfer trends and characteristics. It was found that the heat transfer was enhanced due to the generation and spreading of the vortex at the beginning of each pulsation cycle. Vortex generation led to flow mixing. Heat transfer was found to be maximum when the pulsation flow period matched the time

taken by vortex generation, its growth and finally ejection into the main flow. Qiu et al. [47] experimentally studied oscillatory flow fluid mechanics and heat transfer phenomena in a pipe. Time resolved velocity and temperature profiles were recorded at various axial locations. Transition to turbulence caused by near-wall flow instabilities as well as the effects of the arrival of highly turbulent flow from the pipe entrance were documented. In the laminar regime, the near-wall flow behaved like a thin and growing boundary layer under an accelerating core whereas in the turbulent regime, the flow assumed the behavior of a fully-developed turbulent tube flow. Gbadebo et al. [48] developed local and average Nusselt number correlations for steady and pulsatile flows in the entry region of a pipe. The developed correlations matched their collected experimental data under conditions of uniform heat flux. Zohir et al. [49] examined heat transfer characteristics for laminar and turbulent pulsating pipe flows under different conditions of pulsator location, frequency, Reynolds number and tube diameter. Better heat transfer performance was obtained when the valve was closer to the test section inlet. Lower values of the relative mean Nusselt number were obtained for the upstream location compared to the downstream location at a particular Reynolds number. Larger tube diameters led to better heat transfer performance. Habib et al. [50] examined heat transfer characteristics in a pulsating turbulent pipe flow under varying frequencies and amplitudes. An enhancement in heat transfer rate was found along the entire pipe section by the introduction of pulsation. It was found that the enhancement was maximum when the imposed pulsation frequency was close to the turbulence bursting frequency. Akdag et al. [51] studied heat removal from a surface placed in a vertical column having reciprocating flow. Instantaneous and time- averaged measurements of temperature were

made. Operating frequencies and heat flux were varied while keeping the amplitude constant. A correlation was developed for time-averaged Nusselt number with the kinetic Reynolds number. Haddad et al. [52] developed a correlation for predicting heat transfer coefficients in pulsating flow. A combined dimensionless number was identified that constituted the flow Reynolds number and the dimensionless frequency. The new dimensionless number for flow was used for correlation of the thermal behavior. The correlation worked well for steady and pulsating turbulent heat transfer. Barker et al. [53] developed a model that predicted the heat transfer performance in a transient, unsteady flow that constituted turbulent and relaminarizing phases. An alternate frequency parameter was defined for modeling. The model performed well for the turbulent part but failed for the relaminarizing part. Flow relaminarization was found to reduce heat transfer enhancement for some unsteady flows. For application to electronics cooling [54], Azar studied the effect of flow oscillation in a channel that had an electronic circuit pack. The effects of various parameters, like the channel width, flow velocity and oscillating blade angle were examined. Oscillatory flow was found to be promising in causing convective cooling. It was found that the channel depth was an important parameter. Also, the existence of a groove frequency at which maximum cooling occurred was emphasized. This indicated the need to optimize channel geometry to determine how cooling would be maximized.

1.1.9 Studies Correlating Heat Transfer with Velocity for Flows with Free Stream Turbulence

Maciejewski et al. [55] experimentally studied boundary layer heat transfer with high free stream turbulence by placing a constant-temperature surface at different locations in front

of a turbulent free jet. They made both heat transfer and velocity measurements. The problem was of interest to them since numerical codes underpredicted heat transfer rates in highly turbulent flows. With Reynolds number constant, free stream turbulence of up to 60% was found to augment heat transfer as much as 4 times that predicted using numerical correlations for low free stream turbulence boundary layer flow. Maciejewski et al. [56] found that they could correlate heat transfer data to within 15% from different studies using the Stanton number correlation they devised. The Stanton number was found to be a constant if it were scaled with u', the RMS fluctuating velocity in the free stream. This was an important development since the heat transfer coefficient could be predicted using u' alone without any descriptors from the experimental rig to account for the length scales. Barrett et al. [57] studied the effect of length scale and intensity on heat transfer by imposing grid-generated, small-scale, free-stream turbulence on turbulent boundary layers. The turbulence intensities were in the range 0.1-8%. A significant increase in heat transfer was reported as a result of subjecting turbulent boundary layers to moderate intensity free stream turbulence. Barrett et al. [58] developed a new heat transfer correlation for turbulent boundary layers subjected to free stream turbulence. The correlation used only free stream parameters, mean velocity, turbulence intensity and length scale and was able to correlate data from many authors to within 11%. They found that the previously defined Stanton number, St' based on the fluctuation in velocity in the free stream, also depended on the length scale. The new Stanton number was found to be a constant in the two-region boundary layer model that was used for the correlation. Their work suggested that the response of the boundary layer to the local free stream turbulence was self similar. The near wall flow response was driven by the outer layer flow. Qiu et

al. [59] experimentally studied oscillatory flow fluid mechanics and heat transfer phenomena in a pipe. Time resolved velocity and temperature profiles were recorded at various axial locations. Transition to turbulence caused by near-wall flow instabilities as well as the effects of the arrival of highly turbulent flow from the pipe entrance were documented. In the laminar regime, the near-wall flow behaved like a thin and growing boundary layer under an accelerating core whereas in the turbulent regime, the flow assumed the behavior of a fully-developed turbulent tube flow. Simonich et al. [60] reported that the temperature field was affected by free stream turbulence, as opposed to conclusions made in earlier studies. At a momentum thickness Reynolds number of 6000, they found that the Stanton number increased by about 5% for each percentage increase in rms intensity. Within the scope of their study, they found that for a given turbulence intensity, Stanton number decreased as the length scale increased. Blair [61] experimentally studied the influence of free stream turbulence on heat transfer and skin friction coefficient on zero-pressure-gradient, fully-turbulent boundary layer flow. Velocity and temperature profiles and convective heat transfer coefficients were measured for turbulence intensities in the range of ¼% to 7% with a free stream velocity of 30m/s. Free stream turbulence was found to increase convective heat transfer coefficients and skin friction values to 20%. Blair [62] found that the logarithmic region of the temperature and velocity profiles had a rather weak dependence on free stream turbulence levels. The Reynolds analogy factor was found to increase linearly with increases in free stream turbulence, showing that the Stanton number increased more rapidly with a free stream turbulence increase than did skin friction coefficient. Free stream turbulence had a weaker effect on heat transfer for low Reynolds number flows, a

dependence on dissipation length scale was found and led to a better correlation for skin friction coefficient and Stanton number. Thole et al. [63] carried out boundary layer measurements for turbulence intensities in the range of 10-20% to study the effect of free stream turbulence. Details of mean and rms velocities, power spectra, velocity correlation coefficients and power spectra were reported. Free stream turbulent eddies were found to enter the boundary layer. Thole et al. [64] measured heat transfer and skin friction enhancement due to free stream turbulence. The measured values were compared with correlations in the literature for turbulence intensities in the range of 10-20%. It was found that in this range of turbulence intensities, both turbulence levels and dissipation length scales were needed for modeling. However, for turbulence intensities greater than 20%, the St' correlation by Maciewjeski was found applicable and was preferred, due to its simplicity. At turbulence intensities greater than 10%, free stream turbulence was found to penetrate the boundary layer and was found to be effective in removing heat from the wall. Ames [65] experimentally investigated the effect of large scale turbulence on vane heat transfer. A dependence on length scale was found in the stagnation region and the pressure surface when experiments were done for four different turbulence levels at the inlet. The heat transfer data correlated well with a parameter based on the Reynolds number, turbulence intensity and length scale. Castro [66] studied the effect of free stream turbulence on boundary layers with low Reynolds number. It was found that for low Reynolds number flows the effect of free stream turbulence was weaker and boundary layer showed a stronger Reynolds number effect. This effect reduced as the Reynolds number rose. A modified correlation having dependence both on turbulence intensity and length scale was proposed. Carullo [67] et al. experimentally studied the

effects of free stream turbulence, turbulence length scale and Reynolds number on turbine blade surface heat transfer. Heat transfer augmentation of around 20-30% was found in the presence of free stream turbulence when compared with the no free stream turbulence case for the pressure and suction sides of the blade.

1.1.10 Turbulence in Unsteady Flows

He et al. [68] investigated ramp-type transient turbulent flow in a pipe using laser Doppler anemometry to measure axial, radial, and circumferential components of local velocity. Three types of delayed responses were reported: delay in turbulence production, delay in redistribution of turbulence energy among its components, and delay in radial propagation of turbulence. The axial component of turbulence was found to be faster in response. This response spread to the central portion of the pipe through turbulent diffusion. The three components of turbulence responded in a similar manner to one another in the core region. Turbulence intensity was found to be larger in the decelerating flow and less in the accelerating flow due to the delayed responses mentioned above. Hino et al. [69] studied reciprocating oscillatory flow in a rectangular duct. Mean velocity, turbulence intensity, Reynolds stresses, and turbulence energy production rates were compared for the accelerating and decelerating phases for the cycle. In the accelerating phase, turbulence was found to be triggered by shear instabilities at some distance from the wall but could not be sustained. In the decelerating phase, turbulence was generated near the wall and propagated toward the central part of the duct. Turbulence energy production was extremely high in the decelerating phase. Along with this was a high level of dissipation. It was found that, though the characteristics of

oscillatory flow are different from steady flow, the basic processes of maintaining turbulence production were the same for oscillatory and steady flows.

Akhavan et al. [70] presented experimental results for turbulent oscillatory flow in a circular pipe for a Reynolds number range of 550-2000. A two-color laser Doppler anemometer was used to gather information on radial and axial velocity and velocity fluctuation components during different phases of a cycle. Turbulence was found to explosively appear during the end of the acceleration phase and was sustained through the deceleration phase. Turbulence production was found to be restricted to near the wall of the pipe. During the early part of acceleration, production of turbulence was limited to very low levels and the flow exhibited a nearly laminar flow behavior. Zhao et al. [71] experimentally studied the turbulence and frictional losses in an oscillatory turbulent pipe flow. It was found that a change from favorable pressure gradient to adverse pressure gradient at high kinetic Reynolds number was responsible for the onset of turbulence during the deceleration phase of the cycle. A correlation in terms of the dimensionless kinetic Reynolds number and the fluid oscillation amplitude was formulated to predict the onset of turbulence. Ahn et al. [72] carried out a two dimensional analysis for oscillatory flow in Stirling engine heat exchangers for both laminar and turbulent cases. The results of the anaylsis were compared with experimental results done by researchers previously. The simulation for laminar flow regime was found to be accurate. Transitional flow modeling could not be done by using the standard k-ε turbulence model. The standard model could model the fully turbulent regime within limits of error. A need for better and more rigorous model was emphasized for modeling of transitional flow.

1.1.11 Heat Transfer with Surface Modifications

Augmented surface like pins can lead to enhanced mixing. Pin fins have been used both in electronics cooling and gas turbine industry for enhanced heat transfer by generation of vortices, free shear layers and turbulence transport. Heat transfer experiments were done in the presence of a channel wall augmented with pin fins in the present study. Anderson et al. [73] predicted the adiabatic heat transfer coefficient from pressure drop alone for an array of flat packs with variable channel height and inlet velocity. The heat transfer coefficient based on the adiabatic wall temperature was shown to be independent of the heating distribution in the channel. It is defined in terms of an element's temperature and its own unheated temperature. The maximum turbulence fluctuation in the channel was calculated using the pressure drop. The heat transfer coefficient based on the adiabatic wall temperature was then correlated with the maximum turbulence fluctuation level in the channel. This correlation was found to fit data from channels, containing different geometries of protrusions, including an array of cubes, an array of flat packs, ribs and a staggered array of cubes. Wirtz et al. [74] conducted heat transfer, velocity and pressure drop experiments in a channel with rectangular transverse ribs. They found that a shear layer existed above the top of the ribs where the rms fluctuating velocity, u', was maximum. They found a linear correlation between convective heat transfer and u'. This was an important development since heat transfer data for channels containing both two and three dimensional protrusions could be correlated with u' without taking any other quantity, like length scale, into account. Garimella at al. [75] explored the onset of transition for protruding elements on a channel wall. These protruding elements were simulating flow passages between an array of chip carrying circuit boards. Accurate

modeling of heat transfer required knowledge of the flow regime. The element height was kept constant while varying channel height and streamwise spacing between the elements. Transition was documented by flow visualization and velocity measurements using LDV. Transition was found to be dependent on the flow rate, channel height and location in the array. Channel height was found to influence the transition process in two ways, by affecting the mean velocity (which reduced with the increase in channel height) and by affecting the scales of turbulence. Also, the element height was found to strongly affect the process of transition, since protruding elements were primarily responsible for turbulence production.

Roeller et al. [76] made average heat transfer measurements and detailed flow measurements using LDV around three-dimensional protrusions in a flow channel. This study had application in electronics cooling. They found an increase in heat transfer with the increase in protrusion height. This increase was attributed to flow acceleration in the narrow passages caused by the increase in protrusion height. Also, an increase was found with a decrease in protrusion height. This was due to the increased three dimensionality of the flow and increased mixing due to the turbulence generated. Thus, there were two competing effects that led to an increase in heat transfer, increased flow acceleration and increased turbulent mixing. Siw et al. [77] studied heat transfer and pressure drop characteristics with pin fins in a rectangular channel, with the pins detached from one of the endwalls. The channel simulated the internal cooling passage of a gas turbine airfoil. They experimentally studied the heat transfer performance by measuring the heat transfer coefficient over all surfaces including the endwall and the pin surface. The pins were detached from one of the endwalls to promote turbulent convection and generate

separated shear layers. This led to enhanced mixing and therefore greater heat transfer. An optimal gap value from the endwall was found at which the heat transfer was maximum, with a reduced pressure drop. Moores et al. [78] studied the effect of tip clearance on a pin fin array. The clearance was introduced between the pin tip and the surrounding shroud. They reported an increase in mean heat transfer and a drop in pressure for arrays with $0.5 \leq H/D \leq 1.1$, with the introduction of small gaps (<10% of pin height). They explained that the increase in heat transfer was due to the additional surface area exposed to the flow. Enhancement expected from three dimensional effects due to the introduction of pins was offset by the lower heat transfer efficiency of the tip area, in comparison to a whole array. Small et al. [79] evaluated thermal performance of heat sinks with and without dimples. They reported an improvement in the performance of heat sinks with dimpled rectangular fins in a staggered configuration. They reported that both experiments and simulation reported an increase in heat transfer performance of heat sinks with dimples. The only drawback that dimples gave was an increase in the pressure drop of the air flow. Silva et al. [80] explored the possibility of improving heat transfer performance by using dimpled surfaces in heat sinks. They developed a numerical model for the Nusselt number for use on dimpled surfaces in microelectronics cooling. They also reported an improvement in heat transfer performance and an increase in pressure drag due to dimples. Huang et al. [81] experimentally studied flow characteristic and heat transfer properties of rectangular channels with staggered ribs on opposite walls. They reported arrangements of staggered ribs that could give enhanced heat transfer on the walls. Vorticity, turbulence intensity, wall shear stress and Nusselt number measurements and calculations were made. Yang et al. [82] evaluated the

performance of heat sinks with plate, slit and louver fin patterns. They found that the louver or slit fin performed better than the plain fin when fin spacing was large. A drop in the heat transfer performance of all fins was found at lower Reynolds numbers and lower fin spacings. Elyyan et al. [83] carried out large eddy simulation for channel flows with dimples and protusions on opposite walls with the flow in the laminar regime and in the weakly-turbulent to fully-turbulent regime. They found that the dimples and protusions did not add much to the heat transfer augmentation when the flow was in the laminar regime. The heat transfer augmentation by enhanced surfaces was found to be more when the flow was turbulent. Korichi et al. [84] carried out a detailed numerical study to explore the effects of obstacles mounted both on lower and upper walls on heat transfer and pressure drop in a rectangular channel. They found that obstacle width led to an enhancement in heat transfer whereas the obstacle height and spacing showed no general trend in heat transfer enhancement. The overall Nusselt number was found to be higher on the horizontal face than on the left and right ones. An increase in the overall Nusselt number was found with the increase in Reynolds number. Ames et al. [85] experimentally investigated the flow field in a staggered array of pin fins at varying Reynolds numbers by making hot-wire anemometry measurements with both single and cross wire probes. Using a commercial CFD code, they made detailed 3D calculations. Flow shedding was found near the surfaces of the pins, which led to generation of unsteadiness. The shedding was found to increase with increasing Reynolds number. Separation was found to occur in the first two rows, whereas the turbulence levels were higher for later rows which showed unsteady separation. The commercial CFD code was found to underpredict heat transfer enhancement and pressure drop, attributed to the

turbulence model. Armstrong and Winstanley [86] carried a review of heat transfer in staggered pin fin arrays for turbine cooling applications. The row-resolved heat transfer rates were higher for the first few rows, followed by a decrease for the downstream rows, reaching an asymptotic, fully-developed value. Heat transfer rates for the pin fin and endwall appeared to be of the same magnitude. Below a certain value of the pin height-to-diameter ratio, the ratio did not seem to affect the heat transfer rate significantly. However, above this value, the heat transfer rate was found to increase with increasing pin height to diameter ratio. Yang [87] numerically explored heat transfer enhancement in a channel with obstacles having an oscillating bar at the channel entrance. This study was done for application to electronics cooling. The oscillating bar generated vortices at the channel entrance that travelled downstream. The vortices generated by the oscillating bar interacted with the vortices generated by the obstacles leading to heat transfer enhancement when the bar moved upward and a drop in heat transfer when the bar moved downward. The overall effect of the oscillating bar mechanism combined with the channel obstacles was an increase in heat transfer. The heat transfer enhancement increased with increasing oscillation amplitude; however, the oscillation speed was found to not have a significant effect. Heat transfer enhancement increased with increasing Reynolds number. Korichi et al. [88] numerically studied heat transfer in a channel with periodic obstacles mounted both on upper and lower walls. At low Reynolds number, flow was found to be steady and stable. However, as Reynolds number increased, it was found that the periodic contraction and expansion in channel cross section lead to generation of Tollmien-Schlichting waves. These waves helped in enhancing heat transfer by leading to more transport between the main channel flow and the interobstacle

grooves. Increasing Reynolds number led to increases in unsteadiness, which led to heat transfer enhancement. It was found that having obstacles on both walls led to greater heat transfer than having obstacles on one wall. Lyall et al. [89] studied heat transfer enhancement for pin fins with a height-to-diameter ratio of unity and different spanwise spacings for Reynolds numbers in the range of 5000 to 30000. Their study revealed that heat transfer enhancement in their experiment, compared to open channel flow, was higher for lower Reynolds number and smaller spanwise spacings. Also, pin fin heat transfer was found to be higher than endwall heat transfer. Garimella et al. [90] studied heat transfer enhancement for staggered and inline pin fin arrays with water cooling. For the fourth row and beyond, a fully developed condition with respect to heat transfer was found. With increasing channel-height-to pin-height ratios, Nusselt number was found to decrease and then reach an asymptotic value. Streamwise spacing was found to be more significant in affecting heat transfer enhancement, compared to the spanwise spacing. Staggered arrangements led to greater heat transfer enhacement. Azar et al. [91] studied the effects of pin fin density on thermal resistance of heat sinks for different air velocities. It was found that an optimum pin fin density existed at which thermal resistance was minimum. Increasing pin fin density did not lead to a decrease in thermal resistance. There was an optimum point beyond which increasing pin fin density led to an increase in thermal resistance. Liu et al. [92] studied the heat transfer performance of staggered pin fin heat sinks using deionized water as the coolant. They found that both the Nusselt number and the pressure drop increased with increasing Reynolds number. The rate of increase of Nusselt number decreased with increasing Reynolds number. Won et al. [93] experimentally documented spatially resolved heat transfer and flow

characteristics for array of pin fins on two surfaces of a channel. Primary and secondary horseshoe vortices upstream of individual pins, beneath pin wakes and in shear layers led to high Nusselt numbers. Nusselt numbers were found to be high in the presence of pins when compared to those of a plain surface. Also, Nusselt numbers were found to vary with Reynolds numbers. Larson et al. [94] carried out a study to determine the interpin spacing and pin height that led to lowest thermal resistance under conditions of constant pumping power and constant fin to airstream temperature difference. In the range of data they covered, they discovered that the thermal resistance was lowest when the pins were longest and the inter fin spacing was smallest. Lawson et al. [95] experimentally studied the effects of spanwise and streamwise spacing on pin fin heat transfer for Reynolds numbers varying between 5000 and 30000. They found that pin fin heat transfer was more affected by streamwise spacing than spanwise spacing. Tahat et al. [96] experimentally studied the effects of geometrical changes and airflow rate changes on forced convection heat transfer from pin fin arrays. They identified optimal spanwise and streamwise spacings for which heat transfer was maximum. A Nusselt number correlation based on spanwise spacing, streamwise spacing and Reynolds number was suggested.

1.2 Motivation for Research

The increasing demand on the performance of electronic devices has led to requirements of higher heat fluxes to be dissipated over smaller areas. Some of the technologies for electronic equipment cooling like air cooling, liquid jet impingement and boiling have been discussed in Section 1.1. As has been discussed, air cooling has always been the preferred method due to its cost effectiveness and reliability. Most of the air cooling methods used so far have been by conducting the heat generated on a chip through a

finned unit that is cooled by a centrifugal fan. Figure 1.1 shows such a device, an integrated fan heat sink assembly.

Figure 1.1: Microprocessor heat sink with fan (Image by Tyco Electronics)

Piezoelectric patches have been used as fans in the flapping mode of motion to cool a heated surface. Much research has been done on the use of piezoelectric patches as fans [26-32].

Most of the above-mentioned chip cooling techniques do not have a vigorous active cooling technology. Most of the active cooling technology is in the form of a fan either as a centrifugal blower or as a piezoelectric patch in the flapping mode. The need for todays electronics cooling demands better methods in developing active cooling modules. Our research group explored the possibility of making use of a piezoelectric stack to vibrate a blade in the translational mode, so that it cools the channel not only at its base but also the side. The aim is to agitate the flow highly and disrupt boundary layer development on the channel walls. A translational mode provides benefits in that it can also cool the side walls of the channel, which have a much large area compared to the base of the channel.

A twenty six finned channel heat sink as shown in Figure 1.2 has been designed by our research group. The figure does not show all twenty six channels. The channels shown are just a representative of how the actual module would look. Each channel of the fin is being cooled by an agitator blade driven translationally by a PZT patch. The end of the fin is cooled by using synthetic jets. Figure 1.3 shows a single unit fin channel cooled by the agitator and synthetic jets. Figure 1.3 gives an understanding that the agitator blade cools the side and the tip walls of the channel whereas the synthetic jet cools the side wall portion of the base of the channel.

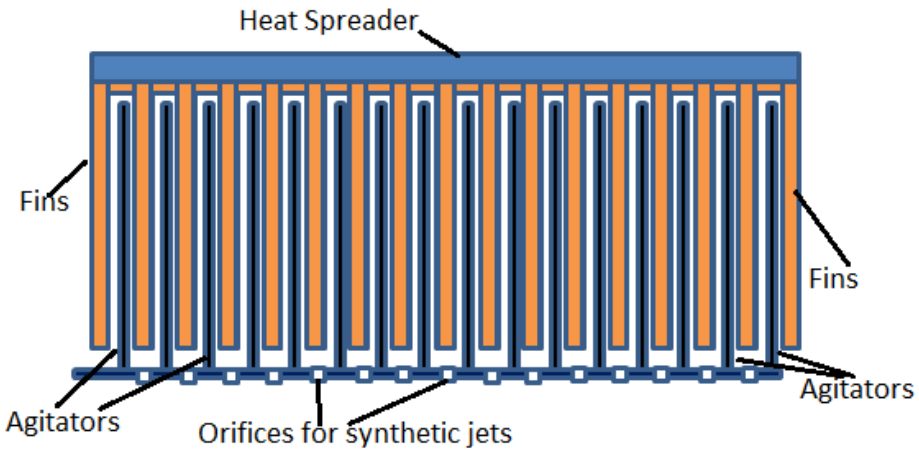

Figure 1.2: Schematic figure of the Active Heat Sink Cooling Module

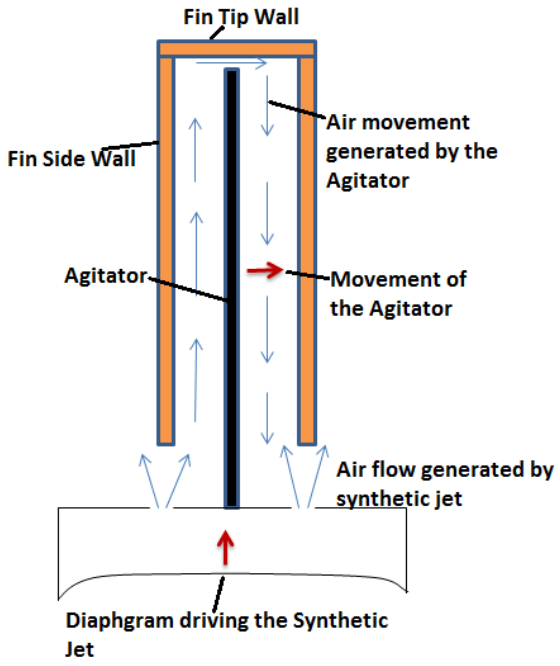

Figure 1.3: Schematic figure showing the convective cooling of a single fin unit by agitator and synthetic jet

The benefits of this module would be that it can provide lower thermal resistances than have been obtained so far, by using active heat sink technology. It will use the benefits provided by the motion of a piezoelectric stack in a more novel way than has been used so far.

The actual heat spreader is 89 mm X 102 mm (3.5" X 4.6") with 26 channel units. The actual dimensions of each unit are very small and would not be large enough to carry out detailed heat transfer measurements. Factors like frequency of vibration of the agitator, amplitude of the agitator, the tip gap between the agitator blade and fin tip are important parameters. The surfaces of the fins can be plain or with ribs. The nature of the finned surface also significantly affects the heat transfer performance. In order to study these parameters in detail, a single fin unit was scaled up to carry out the heat transfer study to help find a better design for the small scale unit. Figure 1.4 shows a representative

example of the kind of flow field generated by the agitator blade as it translates back and forth inside the fin cavity.

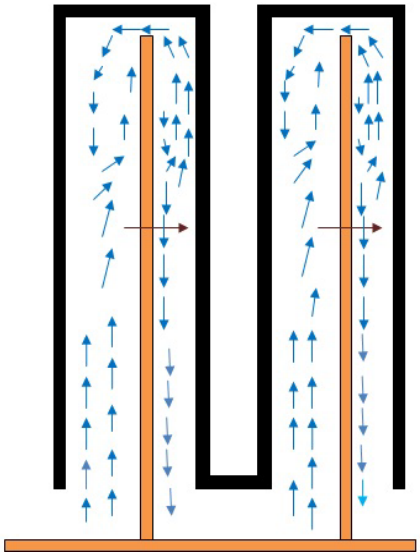

Figure 1.4: Schematic diagram showing the agitator movement inside fin channels

The aim of this study is to document the cooling of a single fin unit by the motion of the agitator alone. The actual module also has throughflow and synthetic jets. This thesis study will focus on the convective heat transfer due to the motion of the agitator. To do this efficiently, the fin unit must be scaled up. Thus, this study scaled up a single fin unit with the agitator in order to learn more about the heat transfer and flow phenomena inside the unit. The purpose of this study is to identify important parameters that can lead to heat transfer enhancement due to the motion of the agitator inside the fin cavity.

Chapter 2

Experiment Design

2.1 Dimensional Analysis

A 26-channel heat sink is being designed having channel walls that are cooled by translating blades called agitators. In addition to agitation, the heat sink also has fan induced throughflow. The heat sink with agitators and throughflow is shown in Figure 2.1.

A large-scale mock-up test facility was constructed in a fashion that made it dynamically similar to a single channel that could be one of an array of channels used in an electronics cooling heat exchanger. The objective behind the present study is to document in detail the convective heat transfer as augmented by agitator motion. The large scale test facility allows high resolution both in time and space. In the present study, the test channel is a rectangular cavity open on one end to allow inflow and outflow of air as driven by the agitator movement. Thus, the facility allows study of agitation alone, with all flow driven by the agitator itself. Both heat transfer and velocity measurements were made in the channel cavity. Time-averaged heat transfer is measured over selected regions of the channel. Velocity measurements using laser Doppler velocimetry were made within the same regions in which the heat transfer measurements were made to quantify flow agitation produced by the agitator and help explain velocity field effects on heat transfer augmentation.

The scale for the Large Scale Mock Up experiment was decided using dynamic similitude. The equations used for deciding the important dimensions for experimental setup are:

Momentum equation:

$$\frac{\partial u}{\partial t} + u.\nabla u = -\frac{\nabla p}{\rho} + \nu\nabla^2 u \tag{2-1}$$

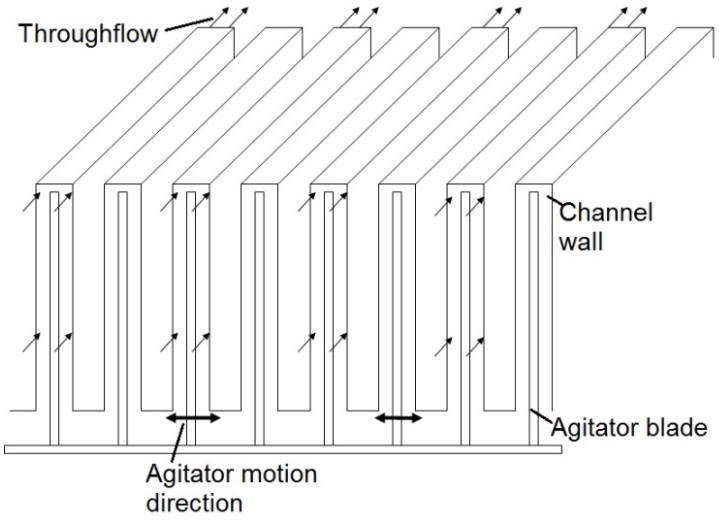

Figure 2.1: Heat sink with agitator and throughflow

Momentum equation in non-dimensional form:

$$\frac{f\mathrm{L}^2}{\nu}\frac{\partial u^*}{\partial t} + \frac{U£}{\nu}u^*.[\nabla u^*] = -\frac{U\mathrm{L}}{\nu}\nabla p^* + \nabla^2 u^* \tag{2-2}$$

Dimensionless numbers from equation 2-2 are the Reynolds number:

$$Re = \frac{U\mathrm{L}}{\nu} \tag{2-3}$$

and the Valensi number:

$$Va = \frac{f\mathrm{L}^2}{\nu} \tag{2-4}$$

The energy equation is:

$$\rho C_p \frac{DT}{Dt} = k\nabla^2 T + \mu\varphi \tag{2-5}$$

The non-dimensional form of the energy equation is:

$$\frac{DT^*}{Dt^*} = \frac{1}{Re.Pr}\nabla^2 T + \frac{Ec}{Re}\varphi^* \quad (2\text{-}6)$$

Dimensionless numbers from equation 2-6 are the Prandtl number:

$$Pr = \frac{\nu}{\alpha} \quad (2\text{-}7)$$

and the Eckert number:

$$Ec = \frac{U^2}{C_p(T_s - T_{sink})} \quad (2\text{-}8)$$

At the fin wall, the heat transfer equation can be written as:

$$q_w = -k\frac{\partial T}{\partial y} = h(T_s - T_{sink}) \quad (2\text{-}9)$$

The non-dimensional form of the above equation is:

$$Nu = \frac{h£}{k} = -\frac{\partial T^*}{\partial y^*} \quad (2\text{-}10)$$

The important dimensionless parameters from the above analysis are the Reynolds number (*Re*), Valensi number (*Va*), and the Nusselt number (*Nu*). Since the viscous dissipation term in equation 2-6 is small, the Eckert number (*Ec*) can be ignored. If the system is scaled so that the Reynolds number and Valensi number are equal for the actual scale and the mock up, then the Nusselt number for both the systems will be equal. The important flow characteristics are captured by both the Reynolds number and the Valensi number. The Reynolds number captures the characteristic flow velocity for the system whereas the Valensi number captures the unsteady effects.

The parameters for the actual scale single-fin unit with the agitator were known. The scaling was done using an actual-scale agitator operating in the frequency range 1000Hz-2000Hz. Numerical values of the dimensional numbers used in this study for an agitator frequency of 1000 Hz are:

$$Re = \frac{u_{max}£}{\nu} = 330 \quad (2\text{-}11)$$

$$Va = \frac{\omega £^2}{\nu} = 570 \quad (2\text{-}12)$$

where ω is the agitation frequency, u_{max} is the maximum agitation velocity, equal to $A_a\omega$, $£$ is the distance between the agitator and the fin wall when the agitator is in its mean position, ν is the kinematic viscosity of air. Using the dimensionless parameters in equations 2-11 and 2-12 and the small-scale module parameters, the scale and the agitation frequency of the Large Scale Mock Up were calculated. The scale of the mock up is 38.8 times the actual scale. The parameters for the mock up and the actual scale are in Table 2.1. Figure 2.2 shows the dimensions of the actual scale and the mock up units.

Table 2.1: Mockup experiment and actual size module parameter values

Parameter	Mock Up	Actual Scale
Fin length (ℓ)	640 mm	16.5 mm
Agitator cavity width (w)	132 mm	3.4 mm
Agitator thickness (t_a)	38.8 mm	1 mm
Amplitude (A_a)	27 mm	0.7 mm
Tip gap (δ_{tip})	19.4 mm	0.5 mm
Frequency (f_a)	0.665 Hz	1000 Hz
Agitator to fin maximum distance (£)	46.6 mm	1.2 mm

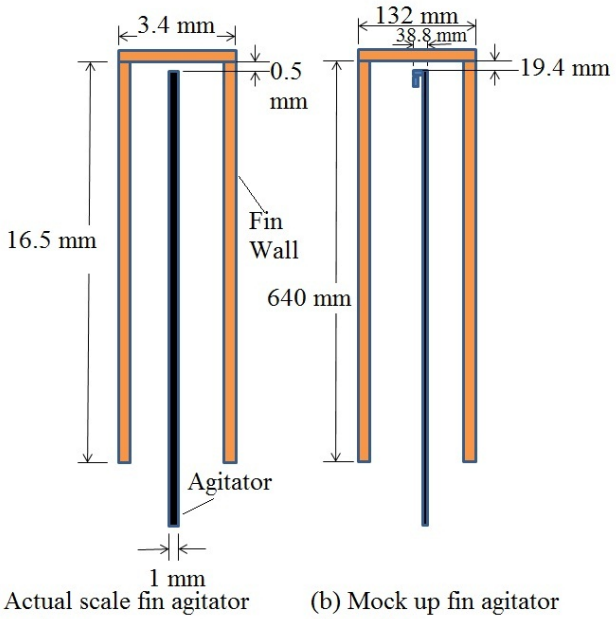

Figure 2.2: Dimensions of the actual scale unit and the mock up unit representing one channel of Fig. 2.1

2.2 Experiment Setup

The experiment set up with the agitator is shown in Figures 2.3a and 2.3b. A Scotch yoke facility is used to drive the agitator plate. A channel was simulated in the mock-up unit using polycarbonate sheets. The right and the tip walls have copper plates embedded in them for heat transfer measurements. Plates adjacent to the test plates are for guard heating. The right wall (Figure 2.3b) of the channel cavity is the wall used for heat transfer measurements. Flow measurements are made in the channel between this wall and the agitator plate. The left and bottom walls are entirely polycarbonate sheets and are, thus, adiabatic. The top wall has glass windows embedded into it to allow passage of laser beams for velocity measurements.

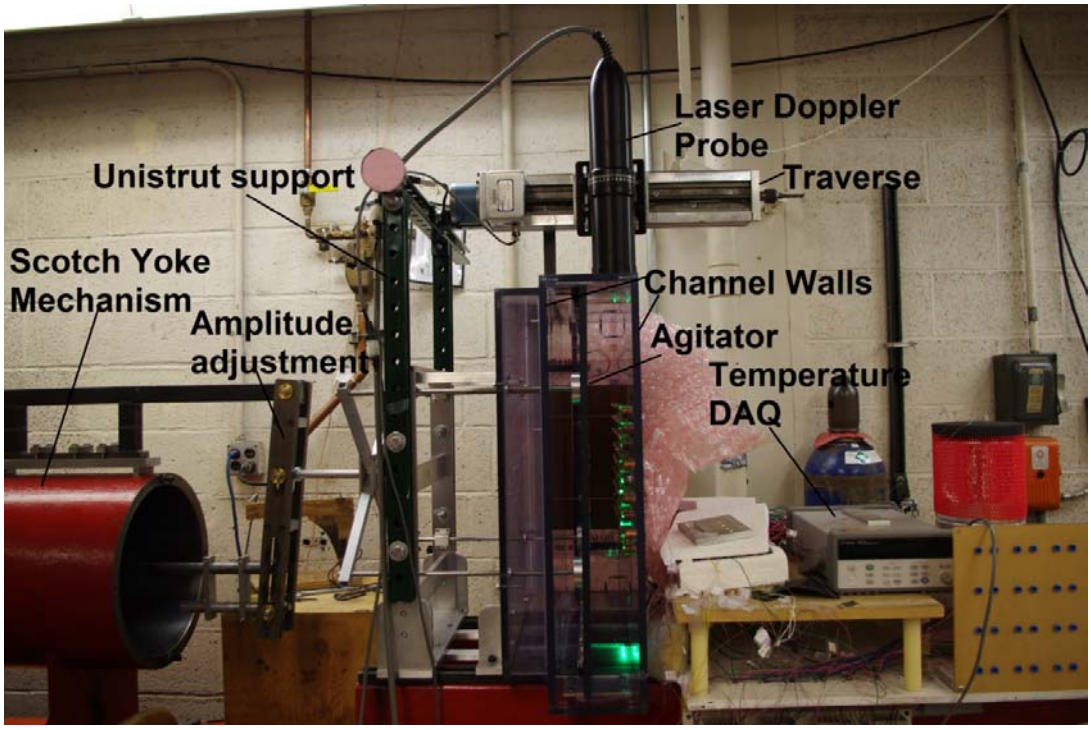

Figure 2.3a: Large scale mock up unit with the agitator driven by a Scotch yoke mechanism

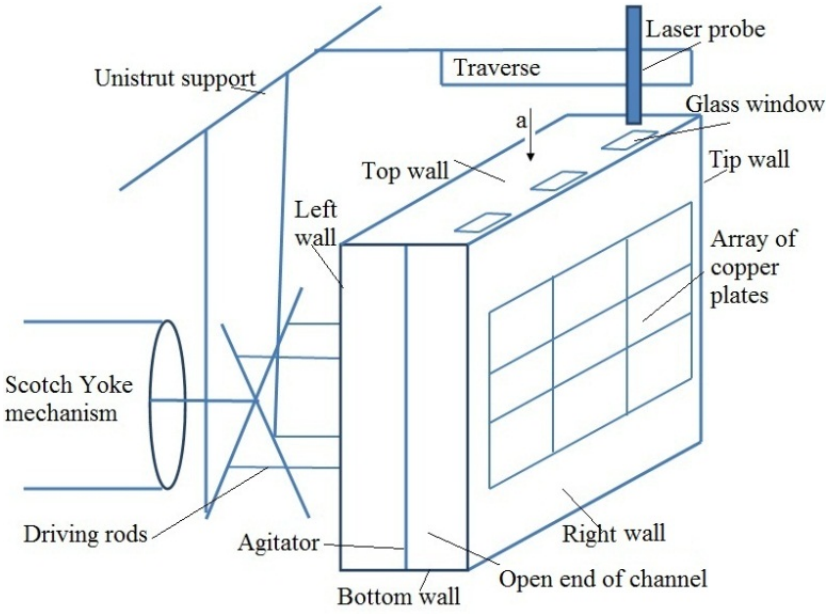

Figure 2.3b: Schematic view of the mock up unit with the agitator driven by a Scotch yoke mechanism

The two edges of the agitator adjacent to the top and bottom walls in Figure 2.3b, are sealed with brush seals. If we look at the channel in the direction of the arrow marked “a” in Figure 2.3b, we get a two-dimensional view similar to that shown in Figure 2.4. As can be seen in that figure, the right wall is divided into three regions: the entry region, the central region, and the base region. The discussion of measurements has been given with reference to these three regions. The aim is to study the performance of the agitator in generating flow unsteadiness, and consequently, enhancing heat transfer in these three regions. The unsteadiness characteristics and heat transfer rates are quite different in these three regions, as will be discussed. The glass windows for optical access are installed so that velocity measurements can be taken in each of these three regions. In Figure 2.4, it can be seen that thermocouples, T1, T2, T3, are attached on the agitator plate to measure local air temperatures corresponding to sink temperatures for wall heat transfer coefficients in these three regions. An important point to note in Figure 2.4 is that the agitator does not extend all the way to the tip wall. There is a narrow gap between the agitator tip and the tip wall. This narrow gap plays an important role in disturbing the flow by generating high-speed flows, free shear layers, and vortices in the base region, as will be shown by the experimental results in the later sections.

2.3 Measurement Method

2.3.1 Heat Transfer Coefficient Measurement

Figure 2.5 shows details of the test plates and guard plates for the right wall (instrumented wall). The placement of the heaters and the copper plates into the polycarbonate wall is shown in the edge view. The middle row of copper plates is used

for heat transfer measurements. The other two rows of copper plates are used for guard heating to provide appropriate boundary conditions for the middle row of test plates.

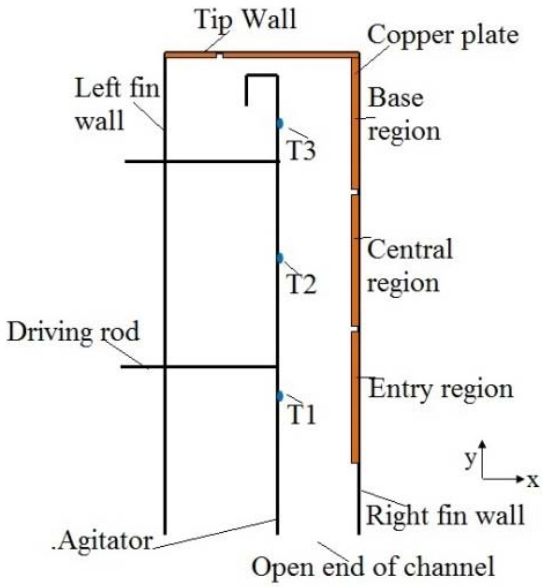

Figure 2.4: Channel in two dimension view

Test plate 2 is used to measure the heat transfer coefficients for the entry region, plate 5 for the central region and plate 8 for the base region. The tip wall also has copper plates embedded into it to provide appropriate boundary conditions for the flow in the base region. Each of the copper plates shown in Figure 2.5 has thermocouples embedded in it to measure the temperature of the plate. The plates are heated using resistance heaters glued on the back of the plates. At the start of the experiment, power is supplied to each copper plate through the heaters attached to it. The agitator is then allowed to oscillate inside the channel cavity to agitate the air and cool the heated plates. Meanwhile, the power supplied to each of the plates is adjusted to maintain steady state with all the plates having the same temperature, thus maintaining an isothermal wall. As shown in Figure 2.4, the local sink temperature, corresponding to each region, is measured by a thermocouple attached on the unheated agitator in the vicinity of that region. The voltage

and current delivered to each heater segment are measured. The heat transfer coefficient is obtained as:

$$h = \frac{VI}{A(T_s - T_{sink})} \tag{2-13}$$

where h is the heat transfer coefficient, V is the measured voltage, I is the current, A is the area of the heated plate segment, T_s is the surface temperature, and T_{sink} is the local sink temperature.

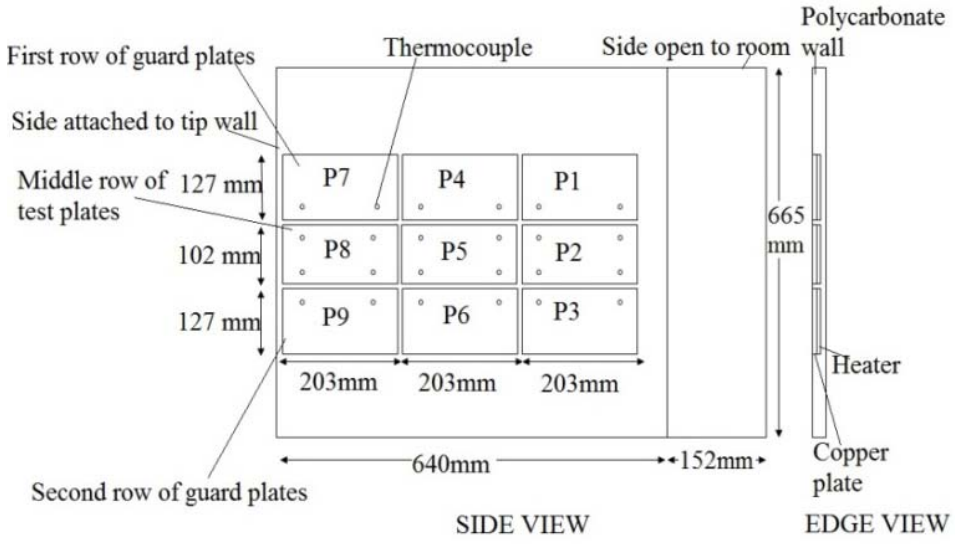

Figure 2.5: Right wall of the test section

Since the measurement is made far from the top and the bottom adiabatic walls, the end wall and corner effects are avoided and the flow can be said to be nominally two-dimensional. The flow domain of interest corresponds to the two-dimensional view shown in Figure 2.4.

2.3.2 Unsteady Heat Flux Measurements

The unsteady heat flux is measured using fine-gauge thermocouples. Type E thermocouples of 25 μm (0.001 inch) thickness were mounted on the test copper plates using a very small dab of glue, as shown in Figure 2.6. This was done so that the

thermocouple measures a near-surface temperature (T_{ns}) which, when subtracted from the signal from the embedded thermocouple in the wall gives a signal that is proportional to the near wall, wall normal temperature gradient.

Thus, the heat flux (Q) can be said to be proportional to the difference in temperature of the body of the copper plate (T_p) to the near-surface temperature (T_{ns}).

$$Q \propto (T_p - T_{ns}) \tag{2-14}$$

The temperature of the copper plate T_p is measured once steady state is reached. The temperature T_p being the bulk temperature of the plate does not change during the cycle. The near-surface temperature T_{ns} is influenced by the flow and varies during the cycle. The variation of the unsteady near-surface temperature T_{ns} is measured. The difference $(T_p - T_{ns})$ is averaged during the cycle and is said to be proportional to the measured time-averaged steady state heat flux Q_{steady}.

$$Q_{steady} = c\,(T_p - T_{ns})_{avg} \tag{2-15}$$

Once the constant c is obtained from the above equation, it is used to calculate the unsteady heat flux by multiplying it with the instantaneous temperature difference $(T_p - T_{ns})_t$, a function of time, with it. In this calculation, it is assumed that the constant of proportionality, c, does not vary with time. Thus, at any time, the instantaneous heat flux Q_t can be calculated as:

$$Q_t = c(T_p - T_{ns})_t \tag{2-16}$$

Figure 2.6: Thermocouple mounted on copper plate with a small dab of glue

Figure 2.7: Thermocouple mounted on copper plate with a small dab of glue. The thermocouple is then connected to a thicker gauge thermocouple of 76 μm (0.003 inch) diameter of the same type (top of figure), to transfer the emf as measured by the smaller gauge thermocouple

2.3.3 Velocity Measurements

Velocity measurements are made using a single-component from the two-component laser Doppler probe. The streamwise direction corresponds to the y axis direction shown in Figure 2.4. For this, the probe is mounted above the channel, as shown in Figures 2.3a and 2.3b. Glass windows 3.2 mm (0.125 inch) thick are installed in the top polycarbonate wall to allow the laser beam to reach the measuring volume inside the channel. These windows have been installed at the three regions of interest, the entry region, the central region, and the base region. The laser probe is attached to a traverse. A water atomizer is used to seed the flow.

For any flow measurement, velocity data are collected for a number of cycles, approximately 80. The flow measurement software acquires a continuous string of data for every cycle. Data in the time interval (0.01 sec) within the oscillation period, are averaged to get a representative value for that interval. As an example, data within the time interval t-0.01 and t are averaged to get a representative value for time t within the cycle for that particular cycle. The ensemble-averaged mean velocity at any instant, t, within the cycle is then calculated as:

$$U_{mean}(t) = \frac{1}{n}\sum_{i=1}^{i=n} U_i(\mathrm{t}) \qquad (2\text{-}17)$$

where i is the cycle number and t is the particular time from the beginning of the cycle. The quantity $U_i(t)$ is a velocity data point at that particular time from the beginning of cycle number i.

The ensemble averaged RMS fluctuating velocity is calculated as:

$$U'_{RMS}(t) = \left(\frac{1}{n}\sum_{i=1}^{n}\left(U_{mean}(t) - U_i(t)\right)^2\right)^{1/2} \qquad (2\text{-}18)$$

where $U'_{RMS}(t)$ is the ensemble-averaged RMS fluctuating velocity at time, t, from the beginning of the cycle.

2.4 Test Section Details

2.4.1 Heat Transfer Measurements

The walls of the test section and the agitator are polycarbonate 12.25 mm (0.5 inch) thick. The copper plates for guard heating and test heating are 6.35 mm (0.25 inch) thick and embedded into the polycarbonate walls with a heater. The heaters 2, 5, 8, 12, and 13 are heater elements in rubber 101.6 mm x 203.2 mm (4 inch x 8 inch) with resistance of 82.7 Ω. The guard heaters 1, 4, 7, 3, 6, 9 are heater elements in Kapton 127 mm x 203.2 mm (5 inch x 8 inch) with resistance of 132.25 Ω. The guard heaters 10, 11, 14, and 15 are 76.2 mm x 101.6 mm (3 inch x 4 inch) in dimension with resistance of 440.8 Ω. Type E thermocouples are used for temperature measurements. Each guard plate on the side and tip walls has two thermocouples. Each test plate on the side wall has four embedded thermocouples whereas the test plate on the tip wall has five thermocouples. The temperatures from the thermocouples on each plate are averaged to get the temperature of the plate. Their variations are less than 1˚C. Power is supplied to each of the heaters via variable transformers. The voltage difference across each heater is measured. Precision resistors with resistance 0.2 Ω are placed in series with the power supply of each plate heater. The voltage across each power resistor is measured to calculate the current going to the respective heater. The power supplied to each heater is then calculated using the measured voltage and current. Experience with these heaters indicates a unity power factor; thus P=VI. An Agilent 34790A data acquisition unit is used to record the

thermocouple voltages. The thermocouples have been calibrated against a precision liquid-in-glass thermometer.

The unsteady temperature T_{ns} is measured by using the Agilent 34970A data acquisition unit. The data acquisition unit triggers the thermocouple 23 times during each cycle to measure the surface temperature. Data are collected for around 60 to 70 cycles. The temperatures from these cycles are then averaged to get ensemble-averaged, unsteady, near-surface temperatures. The ensemble-averaged, unsteady, near-surface temperatures are then used to calculate the unsteady heat flux values, as described above.

2.4.2 Velocity Measurements

A TSI TR 60 series, two-component laser Doppler velocimetry system is used to make velocity measurements. The wall-parallel component of velocity is measured using the argon ion laser beams of wavelength 514.5 nm. The laser beam diameter is 2.65 mm.

2.5 Pin Fin Measurements

Some measurements were done with augmentation of the channel surface heat transfer using pin fins. This was done to study the convective heat transfer enhancement obtained by adding pins to the fin wall. Both heat transfer and velocity measurements were done to quantify the pin fin performance. A staggered configuration of pin fins was used. A set of parameters was chosen from the actual scale heat sink. This set of parameters was found to give optimal performance for the actual scale heat sink, thus it was chosen for study in the mock up [97].

Actual scale design: H=250 μm, D=500 μm, S=1500 μm

Corresponding Large Scale parameters: H=9.7 cm (0.382”), D= 19.4 cm (0.764”), S= 58.2 cm (2.29”)

Actual parameters in large scale: H=10 cm (0.4”), D= 19 cm (0.75”), S= 58.4 cm (2.3”)

Actual parameters for large scale are slightly different from the corresponding large scale parameters due to limits on material availability and ease of machining.

Pin fin Fabrication process

From a 19 cm (3/4 inch) copper rod to make the pin fins, copper pieces 10 cm (0.4”) in height were cut. The copper surface was then made smooth by using sandpaper as shown in Figure 2.8.

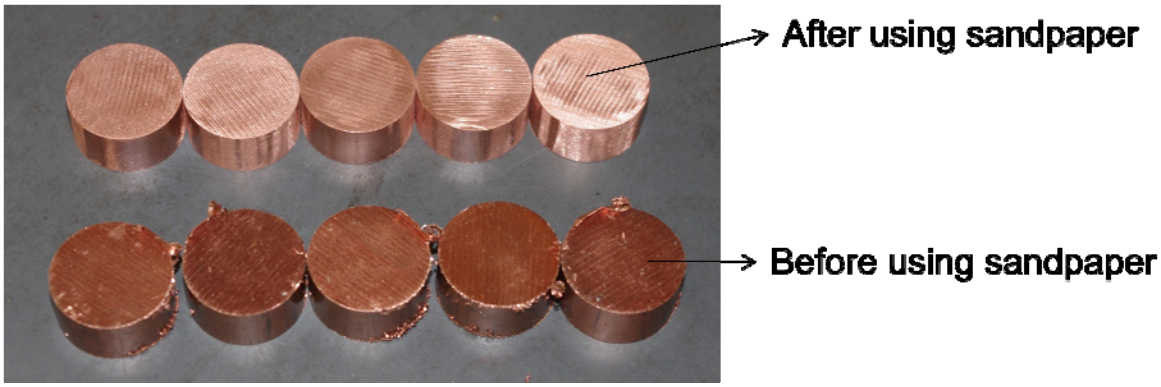

Figure 2.8: Copper pieces smoothened by using sandpaper. These pieces have been used to make a staggered configuration of pin fin array

The pieces shown in Figure 2.8 were glued on the fin wall using double-sided conductive tape. The thermal conductivity of the tape is 1.4 W/mK and thermal impedance is 0.25° C in^2/W. A template was used to attach the pieces on the fin wall. The template is as shown in Figure 2.9. The fin wall with staggered configuration of pin fins is shown in Figure 2.10. The thermal resistance due to the tape junction was calculated as 0.57 K/W, which is much lower than the average convective resistance of the pin fin surface of around 60 K/W.

Figure 2.9: Template used to attach copper pieces on the fin wall

Figure 2.10: Staggered configuration of pin fins on the channel wall

2.6 Uncertainty in Measurements

The uncertainties associated with measurements of heat transfer coefficients, h, were calculated using the equation:

$$\delta h = \left[\left(\frac{\partial h}{\partial P}\delta P\right)^2 + \left(\frac{\partial h}{\partial Q_{net,in}}\delta Q_{net,in}\right)^2 + \left(\frac{\partial h}{\partial T_{sink}}\delta T_{sink}\right)^2 + \left(\frac{\partial h}{\partial T_s}\delta T_s\right)^2 + \left(\frac{\partial h}{\partial A}\delta A\right)^2\right]^{1/2} \quad (2\text{-}19)$$

The uncertainties are: temperature, 0.3 K; voltage, 2% of reading, plus 2counts; precision resistor, 1% of specified resistance of 0.2 Ω. The largest term of equation 2-19 is the power uncertainty. The uncertainty associated with area is small and can be neglected in comparison to the uncertainty produced by measurement of temperature and voltage. The uncertainty associated with each measured heat transfer coefficient is in the range 6-13%.

2.7 Conduction Correction

The experimental procedure calls for attaining an isothermal wall at steady state. However, the temperature differences between adjacent plates may be as large as 1˚C. Thus, a conduction correction has been added to the calculation of the final heat transfer coefficient.

$$h = \frac{P + Q_{net,in}}{A(T_s - T_{sink})} \quad (2\text{-}20)$$

where P is the power supplied at steady state, $Q_{net,in}$ is the power flowing into the copper plate from neighboring copper plates. $Q_{net,in}$ is calculated as:

$$Q_{net,in} = \sum Q_i \quad (2\text{-}21)$$

Where Q_i are heat flows from adjacent copper plates to the copper plate under consideration. Q_i is calculated as:

$$Q_i = \frac{T_i - T_c}{R} \quad (2\text{-}22)$$

where T_i is the temperature of the neighboring copper plate and T_c is the temperature of the copper plate under consideration. The resistance between any two copper plates is R.

It has been calculated using a 2D FLUENT simulation. The conduction correction on plate power is always under 4% of the plate power.

2.8 Natural Convection Correction

The aim of this study is to document the convective heat transfer performance of the agitator without contribution from other sources like natural convection. A test was made to assess the contribution of natural convection to the measured heat transfer coefficient. For this purpose, heat transfer coefficient measurements were made at different wall-to-sink temperature differences. The heat transfer coefficients of test plates 2, 5 and 8, which are being used to measure heat transfer coefficients for the entry region, central region and base region, did not change with changing wall-to-sink temperature difference after taking the conduction correction into account. Thus, it was considered that natural convection had no significant contribution to the measured heat transfer coefficient. As an example, the heat transfer coefficients for base region at three temperature differences are plotted at a frequency of 0.665 Hz and an amplitude of 27 mm in Figure 2.11.

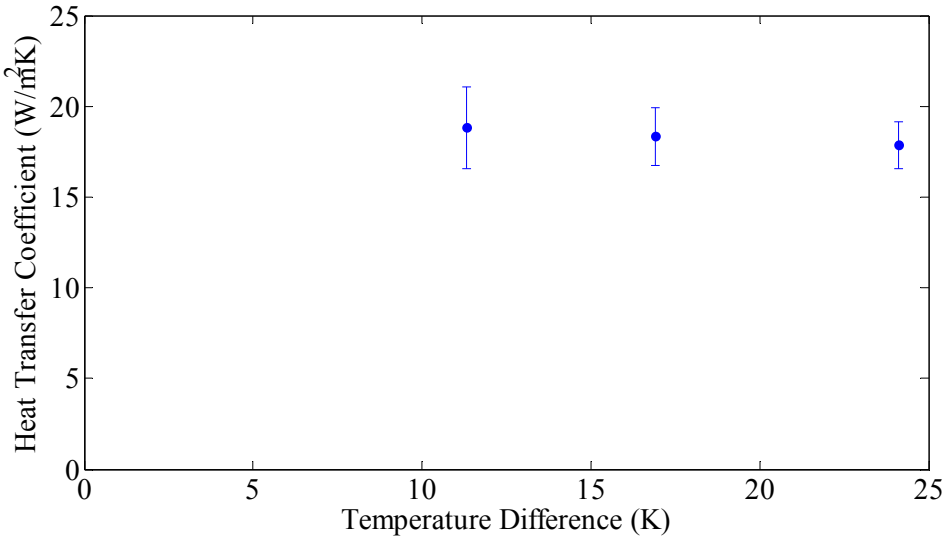

Figure 2.11: Heat transfer coefficient variation with temperature difference for base region

Chapter 3

Plain Wall Velocity and Heat Transfer Measurements

Agitation leads to much activity inside the channel by periodically accelerating and decelerating the flow and generating turbulence. The motivation behind using the agitator inside the channel cavity is to create considerable flow mixing and, thus, to enhance convective heat transfer. As the agitator moves back and forth inside the channel cavity, the flow has an opportunity to escape and enter through two locations, the open end of the channel in the entry region and the narrow tip gap in the base region. Thus, at the same instant within the cycle, the flow has different streamwise directions along different regions of the channel. Different mean and fluctuating velocity dynamics lead to variations of convective heat transfer along the channel length. The heat transfer and velocity variations in each of the three regions are described in detail in the following sections. As shown in Figure 3.1, the agitator motion can be divided into four different phases: phase 1 - as the agitator moves from the mean position to the right wall, phase 2 - as the agitator moves from the right wall back to the mean position, phase 3 - as it moves from the mean position to the left wall and phase 4 as it moves from the left wall back to the mean position. Figure 3.2 shows the variation of agitator velocity as it oscillates back and forth inside the channel.

3.1 Heat Transfer Variation in the Three Regions

Experiments were conducted at three different agitator frequencies, 0.665 Hz, 1 Hz and 1.33 Hz in the large-scale experimental setup. These are the operating frequencies of the Scotch yoke drive used to drive the agitator in the test facility. The amplitude of oscillation of the agitator for the measurements was 27 mm and 33 mm (mean to peak). The time-and area-averaged heat transfer coefficients are shown in Figure 3.3.

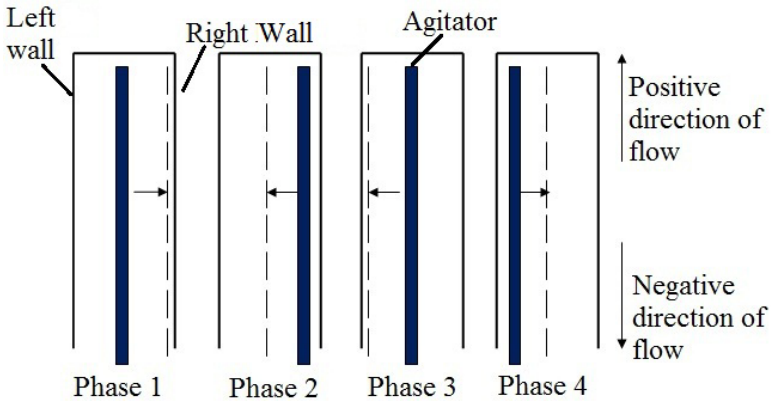

Figure 3.1: Four phases in agitator motion

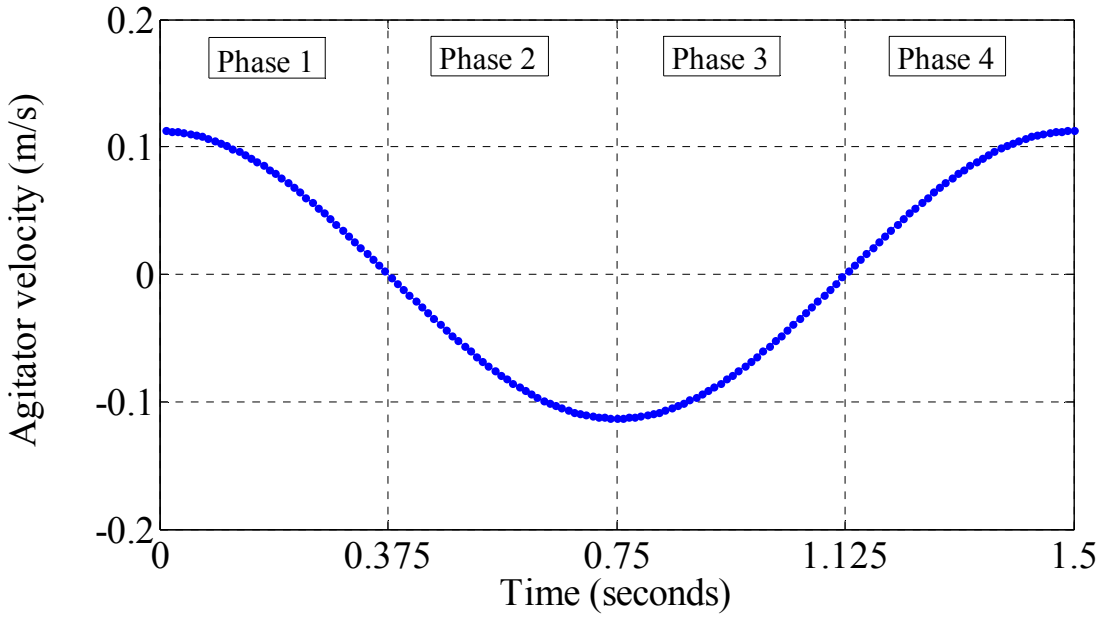

Figure 3.2: Variation of agitation velocity with time for a frequency of 0.665 Hz and an amplitude of 27 mm (mean to peak)

From Figure 3.3, it can be seen that the base region shows high heat transfer coefficients followed by the entry region and the central region, respectively. The variation of heat transfer coefficients along the channel length can be explained by studying the variation of ensemble-averaged mean velocity and the ensemble-averaged RMS fluctuating velocity over a cycle. The mean velocity, fluctuating velocity and turbulence intensity plots in Figures 3.4 to 3.6 show that the ensemble-averaged mean velocity and RMS fluctuating velocities are highest in the base region, followed by the entry region and the central region. The velocity characteristic in each of these regions is discussed in detail in section 3.2. The heat transfer coefficient augmentation in each region can be attributed to two components:

1) Flow sloshing owing to the unsteady mean velocity during a cycle.
2) Flow turbulence due to the RMS fluctuating velocity at every instant within the cycle.

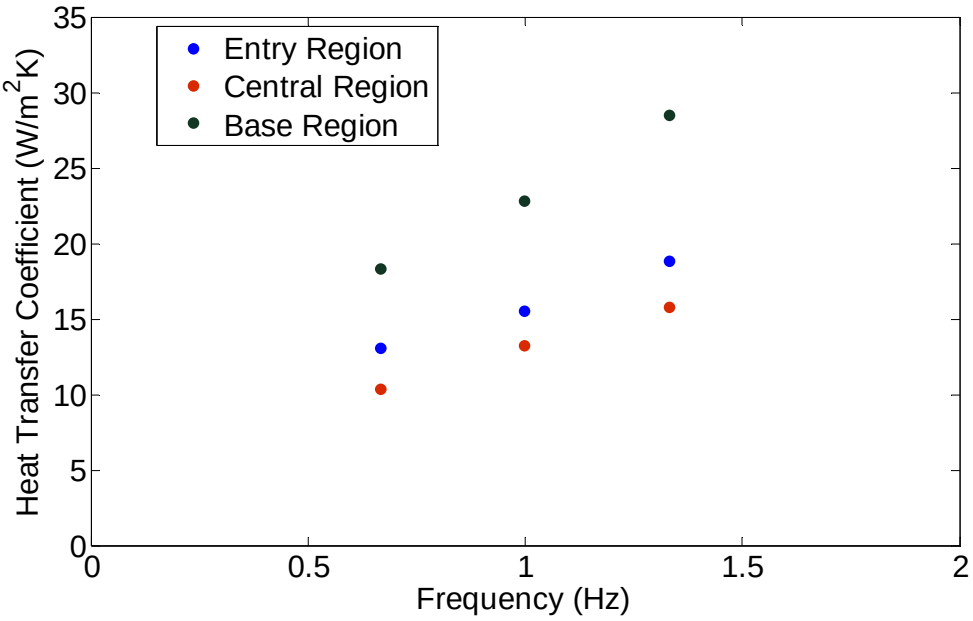

Figure 3.3: Variation of heat transfer coefficients with frequency for entry region, central region and base region, amplitude of 27mm (mean to peak)

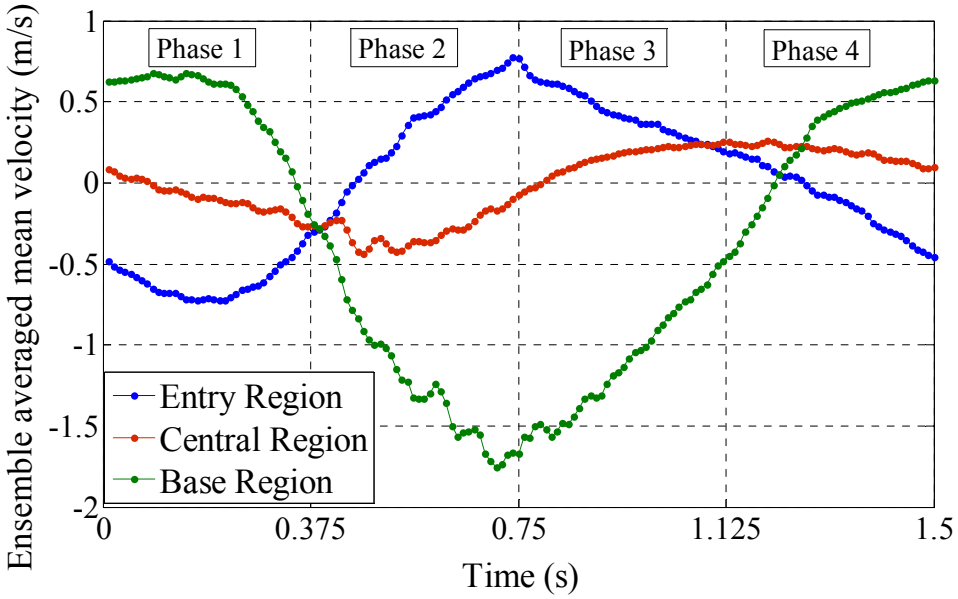

Figure 3.4: Variation of ensemble averaged mean velocity for entry region, central region and base region at a frequency of 0.665 Hz and an amplitude of 27 mm

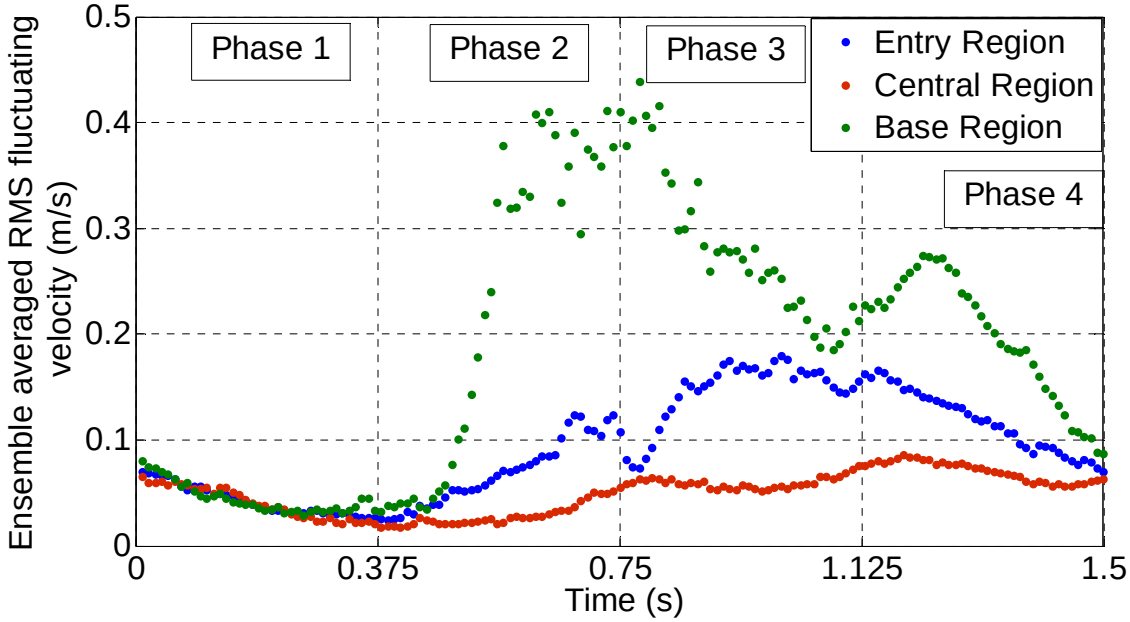

Figure 3.5: Variation of ensemble averaged RMS fluctuating velocity for entry region, central region and base region at a frequency of 0.665 Hz and an amplitude of 27 mm

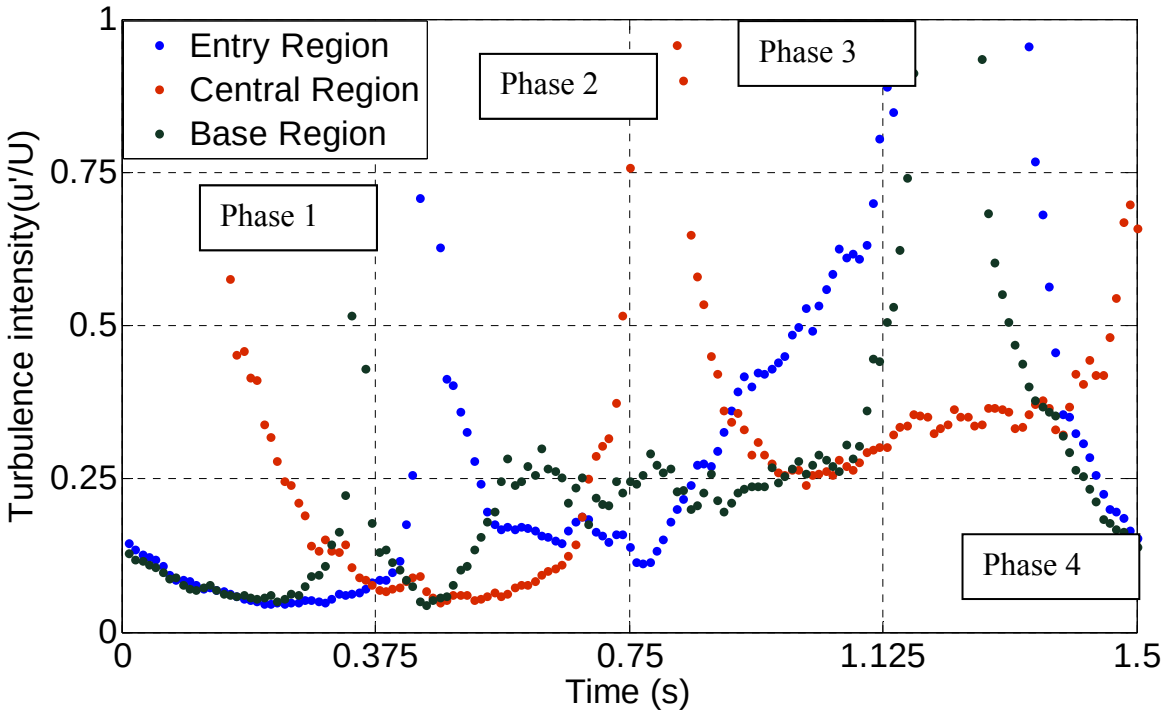

Figure 3.6: Variation of turbulence intensity for entry region, central region and base region at a frequency of 0.665 Hz and an amplitude of 27 mm

3.2 Velocity Characteristics in the Three Regions

3.2.1 Velocity Characteristics in the Entry Region

The ensemble averaged mean velocity for the entry region is shown in Figure 3.4. As can be seen, during phase 1, when the agitator moves from its mean position towards the right wall with deceleration, the flow in the entry region gets sloshed out of the channel through the open end of the channel, first with streamwise acceleration and then with deceleration. During phase 2, the agitator reverses its direction after reaching the extreme towards the right wall, as can be seen from Figures 3.1 and 3.2. Flow in the entry region continues to be sloshed out of the channel for the initial part of phase 2 and then it gets drawn into the channel for the remaining part. It appears that the flow shows some delay in response to the agitator motion. As the right side channel cavity continues to expand during phase 2, flow accelerates as it gets drawn into the channel. Peak positive velocity

is reached as phase 2 ends and phase 3 begins. At this instant, the agitator is at its mean position and has reached its peak velocity as can be seen from Figure 3.2. During phase 3 as the agitator moves toward the left wall and the right side cavity is expanding to its maximum size, flow continues to get drawn into the channel, but with deceleration. At the end of phase 3 and beginning of phase 4, when the agitator reaches the other extreme near the left wall and starts reversing its motion toward the right wall, flow continues to be drawn into the channel, with deceleration for the initial part of phase 4. This again is due to the delayed response of the flow to the agitator motion. It then gets sloshed out of the channel with acceleration for the remaining part of phase 4 as the right side cavity of the channel starts narrowing.

Figure 3.6 shows the turbulence intensity plot for the entry region. The variation of ensemble averaged RMS fluctuating velocity can be seen in Figure 3.5. It can be seen that during phase 1, for the initial part, the turbulence intensity is decreasing as the flow is accelerating. Toward the later part of phase 1, as the flow decelerates, the turbulence intensity starts increasing. During the initial part of phase 2, turbulence intensity tends to very high values. That is because the flow is decelerating and the mean velocity magnitude is going to zero. During the latter part of phase 2, when the core flow is accelerating, the turbulence intensity shows a decrease followed by an increase during the deceleration of phase 3. During the later part of phase 4, turbulence intensity again drops down when the mean flow starts accelerating. From Figure 3.5, it can be seen that the fluctuating velocity increases in magnitude as the flow is accelerating in phase 2. This increase in fluctuating velocity is carried over to the deceleration phase, as can be seen in the deceleration of phase 3. As the flow is decelerating in phase 4, fluctuation in velocity

decreases and the flow seems to be stabilized, as the acceleration phase is approached. Turbulence production is generally high during the deceleration phase and drops down during the acceleration phase.

3.2.2 Velocity Characteristics in the Central Region

As the agitator starts moving, the flow has an opportunity to enter or escape through the open end of the channel near the entry region or through the narrow tip gap region in the base region. The central region being in the center of the entry region and base region gets influenced by either of these during different parts of the flow cycle. Due to two open ends through which flow can enter or leave, the agitator creates quite complex flow dynamics. At the same instant, flow direction might be positive in certain regions and negative in other regions. Core flow might be going through acceleration for some streamwise length along the channel wall, whereas it might be undergoing deceleration at other locations.

During phase 1, when the agitator just starts moving toward the right wall, the flow in the central region seems to be more influenced by the base region for the initial part, thus flow direction is positive (toward the base region). Note that Fig 3.1 shows the positive and negative flow directions. Following the initial part of phase 1, it seems to be more influenced by the entry region flow. Thus, flow is escaping the channel cavity in the negative y direction, with acceleration which is similar to entry region characteristic. During phase 2, when the agitator is moving away from the right wall toward the mean position, flow in the central region continues to move toward the open end of the channel first with acceleration and then with deceleration. Thus, in phase 2, flow in the central region is dominated by base region characteristics. During phase 3 when the agitator

moves from its mean position toward the left wall, the flow direction is positive, showing that the central region is affected by the fluid drawn into the channel from the open end close to the entry region. Phase 4 also has fluid motion in the positive y-direction, though with deceleration. From Figure 3.6, it can be seen that for central region, the turbulence intensity rises when the flow decelerates during phases 2 and 4, and the turbulence intensity drops during the acceleration phases 1 and 3. This shows that deceleration triggers turbulence production and acceleration leads to stabilizing the flow.

3.2.3 Velocity Characteristics in the Base Region

During phase 1, when the agitator starts moving from the mean position toward the right wall, the flow in the base region gets drawn out of the right side channel cavity through the tip gap, with deceleration for the latter portion of the phase. During phase 2, as the agitator moves from the right wall toward the mean position, flow gets drawn into the channel cavity through the tip gap, corresponding to the negative y direction. Phase 2 has flow accelerating into the channel cavity over the tip gap region due to the expanding right side cavity. As the right side cavity continues to expand during phase 3, due to the movement of the agitator from the mean position toward the left wall, flow continues to be drawn into the cavity through the tip gap but with deceleration. As the agitator reaches the extreme toward the left wall and reverses its direction, during phase 4, flow still continues to get drawn into the agitator cavity for the initial part. This is because the flow shows some delay to the agitator motion. For the remaining part of phase 4, flow is sloshed out of the channel cavity with acceleration, as the right side cavity of the channel is contracting.

As can be seen in Figures 3.5, the magnitude of the fluctuating velocities change over the different phases. The magnitude of fluctuating velocity increases toward the end of acceleration phase in phase 2 and continues to be high in the deceleration phase. Toward the end of deceleration in phase 3, fluctuating velocity again starts decreasing; thus, the flow starts stabilizing towards the beginning of the acceleration phase. From Figure 3.6, it can be seen that the turbulence intensity starts increasing toward the latter part of phase 2, which marks the end of the mean flow acceleration phase. Turbulence intensity is high during phase 3, which corresponds to decelerating core flow. Turbulence intensity starts reducing toward the end of phase 4 when the flow shows acceleration. As noted earlier, turbulence production is generally high during the deceleration phase.

3.3 Parametric Study

A parametric study was conducted to study the effects of frequency, amplitude and velocity of agitation in generating flow unsteadiness and enhancing convective heat transfer. Heat transfer and velocity measurement results are presented and discussed in the following sections.

3.3.1 Frequency Study

Figure 3.3 shows the variation of heat transfer coefficient for the entry region, central region and base region at three different frequencies of 0.665 Hz, 1.0 Hz and 1.33 Hz. As expected, an increase in frequency leads to an increase in heat transfer coefficient. Figure 3.7(a)-(c) shows the variation of ensemble-averaged mean velocity with frequency for each of the three regions. The mean velocity has been plotted against the scaled time, since the cycle time is different for each of the three frequencies. A fair comparison for velocity characteristics during different phases can be made only if the time is scaled with

the actual cycle time. As can be seen from the figure, the ensemble-averaged mean velocity increases with an increase in frequency. There is no change in velocity characteristics in terms of flow acceleration/deceleration with a change in frequency. The mean velocity shows the same trend for each of the four phases irrespective of the change in frequency. The increase in the mean velocity is proportional to the increase in frequency. Thus, it can be said that the mean velocity directly scales with the frequency, amplitude of agitation being constant.

Figure 3.8(a)-(c) shows the variation of ensemble averaged RMS fluctuating velocity with frequency for entry region, central region and base region, respectively. As was observed for the mean velocity, the RMS fluctuating velocity more or less directly scales with frequency without showing any change in characteristics during each of the four phases.

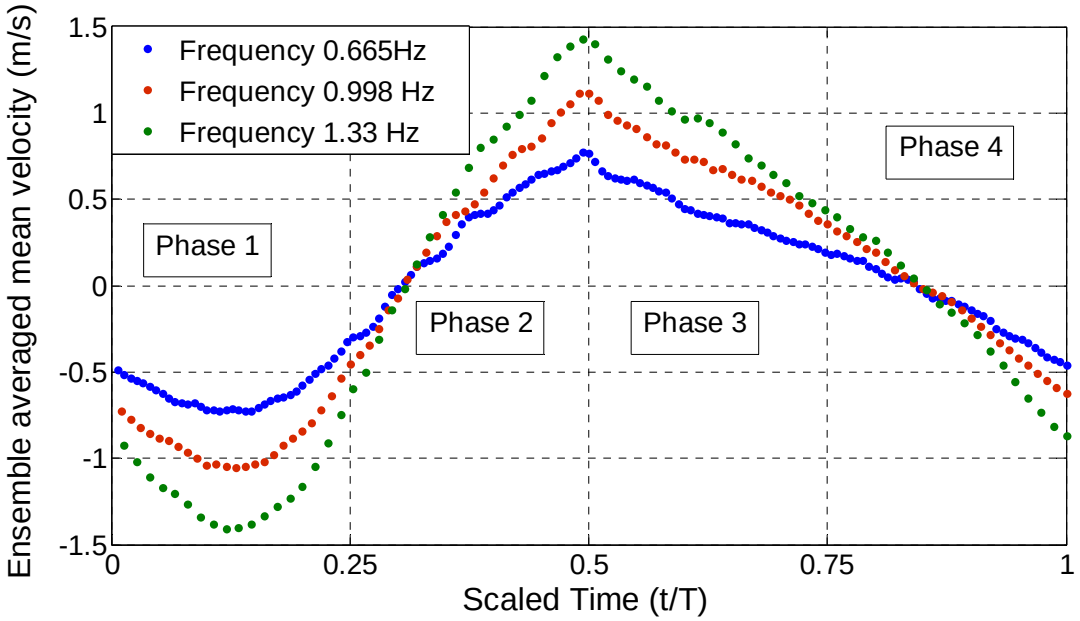

3.7(a) Entry region

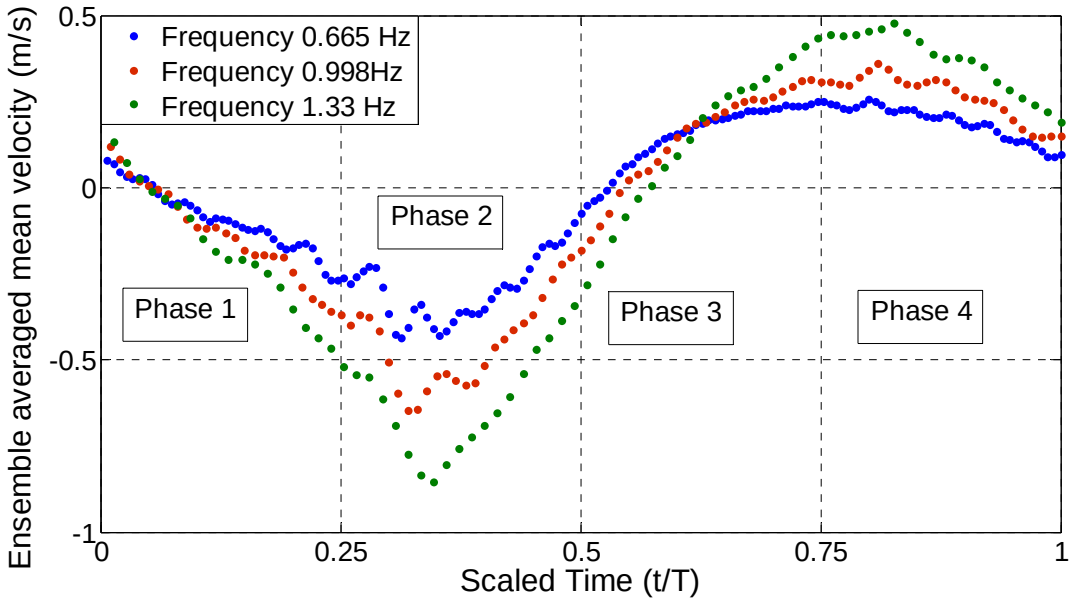

3.7(b) Central region

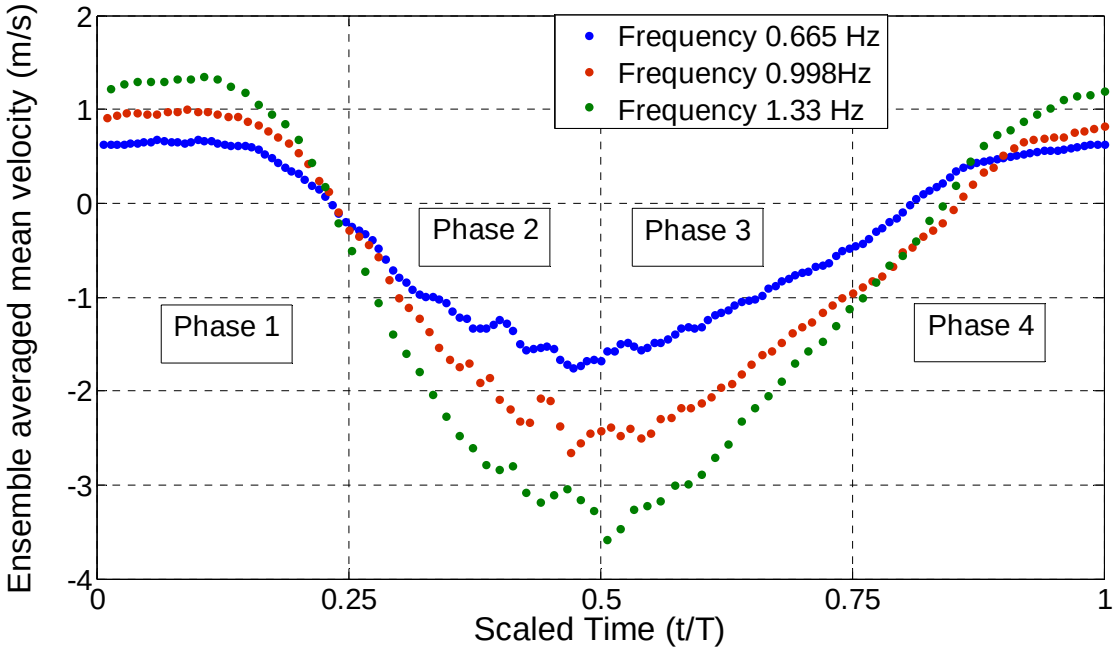

3.7(c) Base region

Figure 3.7: Variation of ensemble averaged mean velocity with frequency

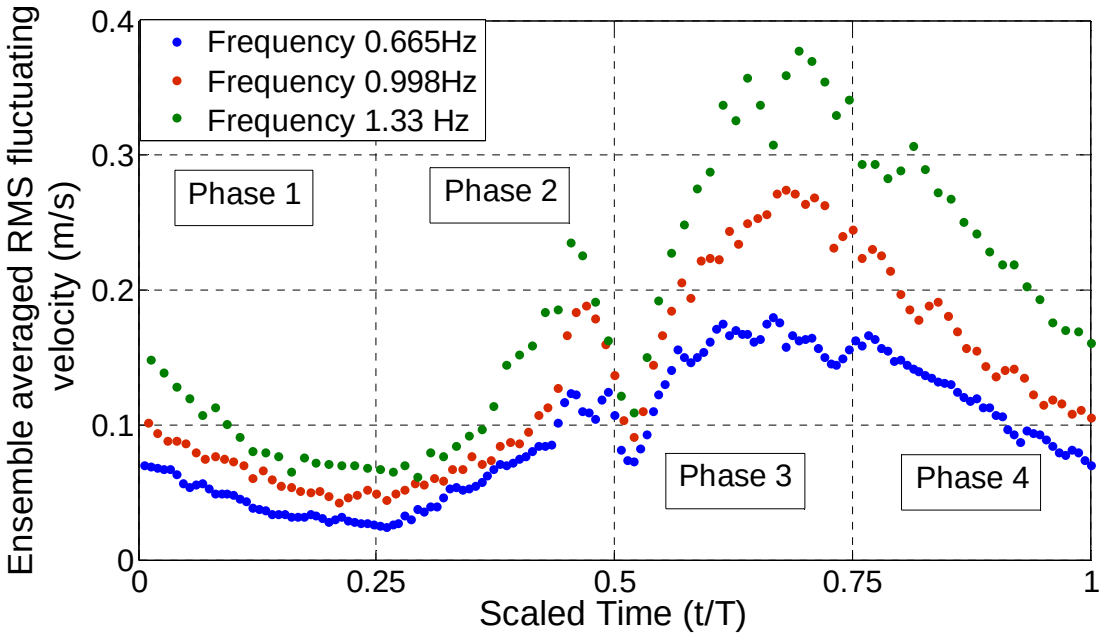

3.8(a) Entry Region

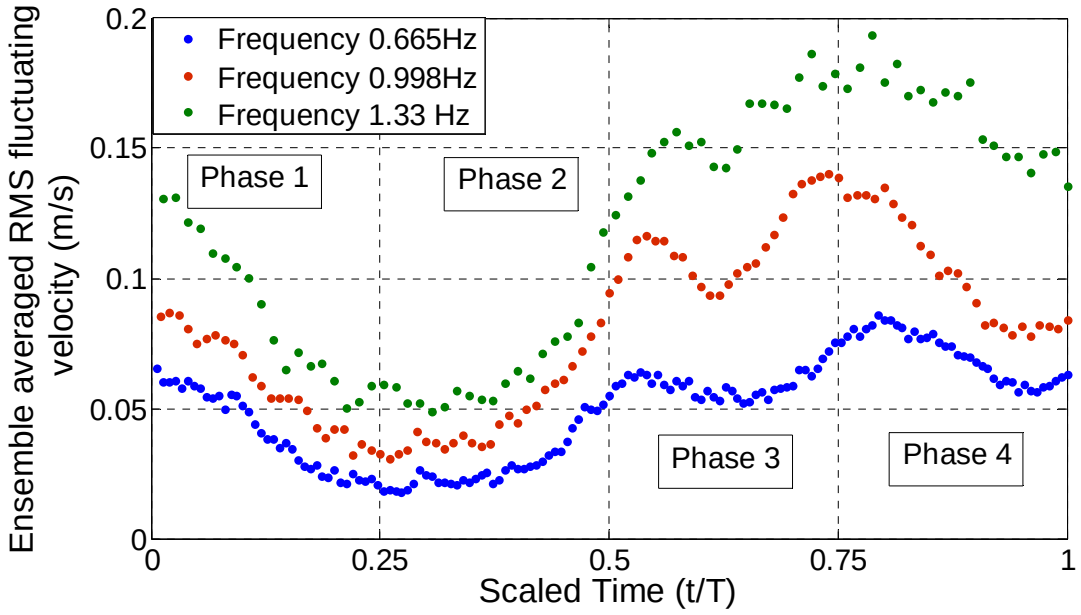

3.8(b) Central Region

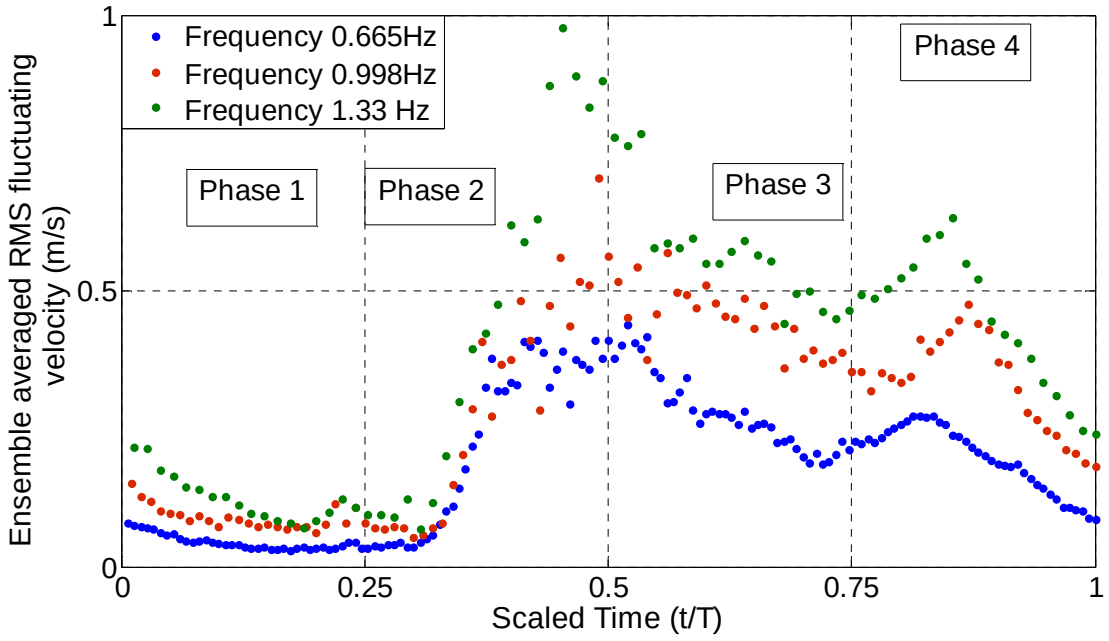

3.8(c) Base Region

Figure 3.8: Variation of ensemble averaged RMS fluctuating velocity with frequency

3.3.2 Amplitude Study

The effect of varying amplitude on heat transfer was studied for each of the three regions, entry, central and base at a fixed frequency of 0.665 Hz. Table 3.1 lists the heat transfer coefficients at two amplitudes of 27 mm and 33 mm (mean-to-peak). An increase in heat transfer coefficient is observed with the increase in amplitude, the increase is not so significant in the central region.

Figure 3.9(a)-(c) shows the variation of ensemble-averaged mean velocity with amplitude. From Figure 3.9(a), it can be seen that the mean velocity magnitude increases with increase in amplitude for the entry region. A slight change can also be observed in the flow characteristics at the end of phase 2 and beginning of phase 3. With an amplitude of 27 mm, one sees a sharp bump right at the beginning of phase 3, when the acceleration phase ends and deceleration phase begins; however, the change is more

smooth for an amplitude of 33 mm. Figure 3.10(a) shows the fluctuating velocity trends for entry region at two different amplitudes. There is an increase in velocity fluctuation with increasing amplitude, the increase being more during phase 3, which marks flow deceleration for the entry region. Turbulence production is generally high during the deceleration phases, higher amplitude enhances turbulence production during such phases.

Figure 3.9(b) shows the variation of mean velocity with amplitude for the central region. During phase 1, the mean velocity curves mostly overlap for the two amplitudes, with the higher amplitude showing more fluctuations. There is a slight increase in mean velocity during phase 2 for the higher amplitude case. However, toward the end of phase 3 and all of phase 4, there is a decrease in mean velocity with higher amplitude. Higher amplitude increases deceleration rate of the flow during phases 3 and 4. This leads to higher turbulence during phases 3 and 4, as can be seen from the fluctuating velocity plots in Figure 3.10(b). Table 3.1 shows that the increase in heat transfer coefficient with increase in amplitude is not very significant for the central region. This could be due to a decrease in magnitude of mean velocity in phases 3 and 4 with the increase in amplitude. There is an increase in the magnitude of fluctuating velocity but probably the increase in fluctuating velocity is offset by the decrease in mean velocity, the net result being a minor increase in heat transfer coefficient with the increase in amplitude.

The variation of mean velocity with amplitude for the base region can be seen in Figure 3.9(c). Higher amplitude leads to an increase in the mean velocity without significant changes in flow characteristics. The fluctuating velocity plots closely overlap for the two amplitude cases for the base region, as can be seen in Figure 3.10(c). This shows that

increasing amplitude primarily leads to increase in mean velocity without generating more turbulence in the base region. It appears that for the base region, higher amplitude might provide flow blockage; thus with increasing amplitude, one does not see enhanced turbulence production.

Table 3.1: Variation of heat transfer coefficient with amplitude at a fixed frequency of 0.665 Hz

	Amplitude 27 mm	**Amplitude 33 mm**
Entry Region	13.02	15.33
Central Region	10.42	11.06
Base region	18.33	21.15

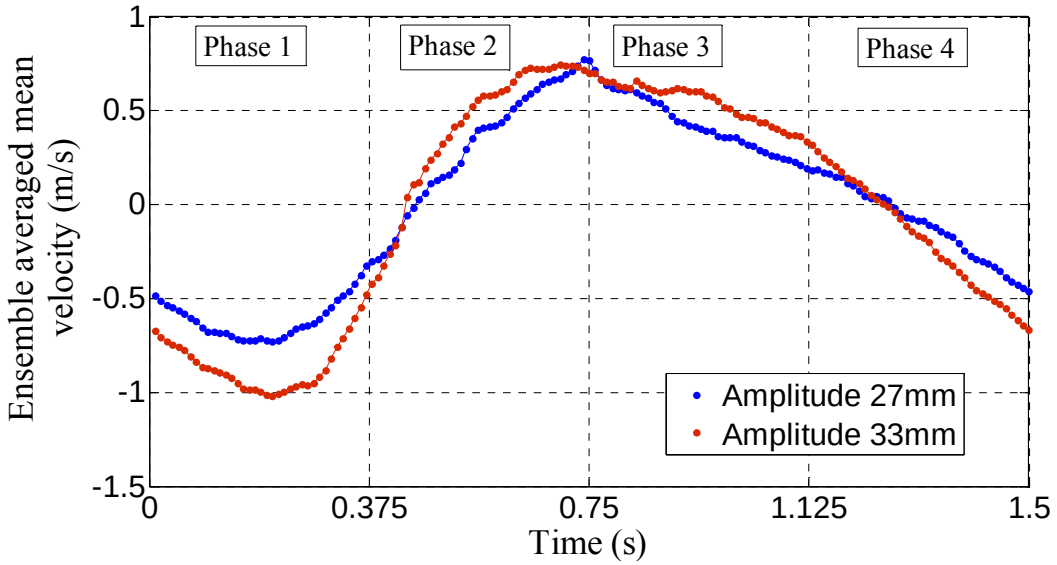

3.9(a) Entry Region

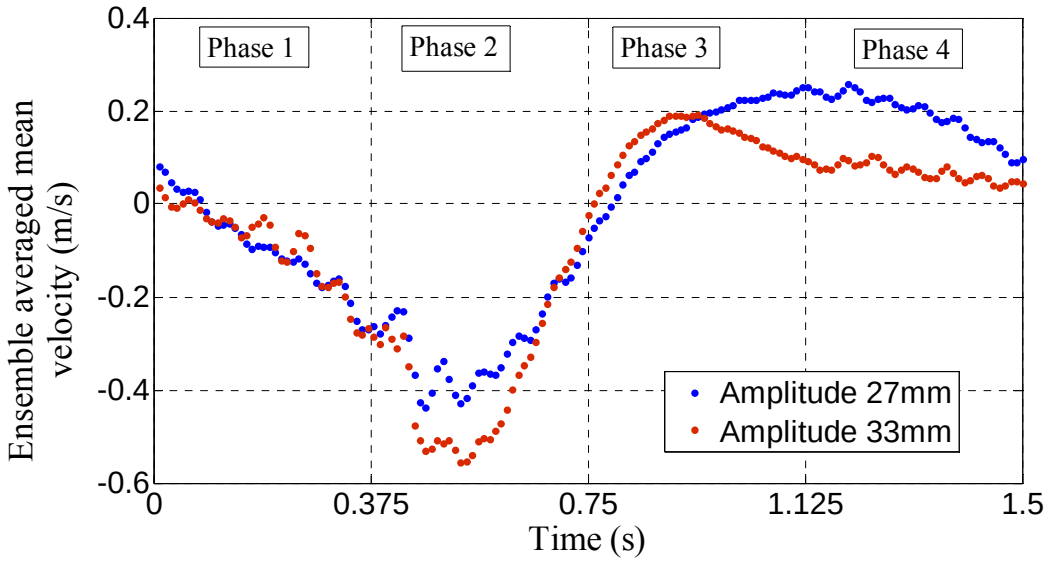

3.9(b) Central region

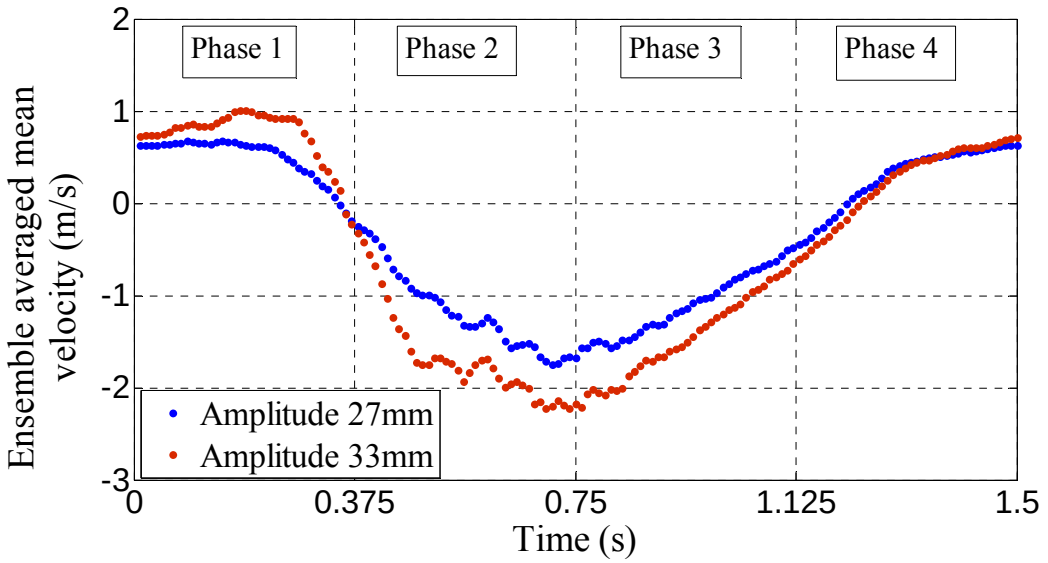

3.9(c) Base Region

Figure 3.9: Variation of ensemble averaged mean velocity with amplitude at a fixed frequency of 0.665 Hz

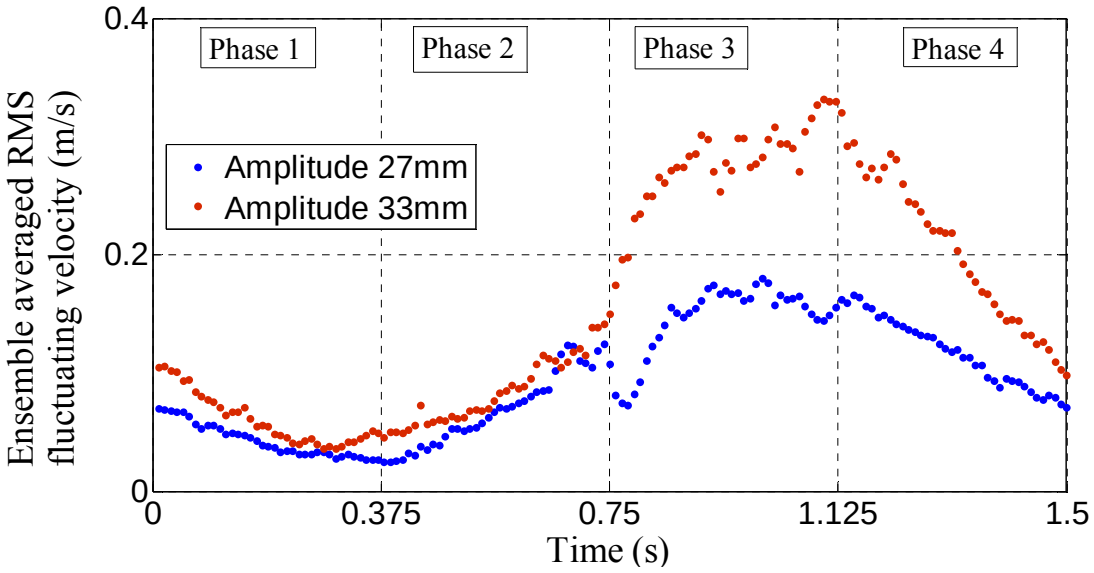

3.10(a) Entry Region

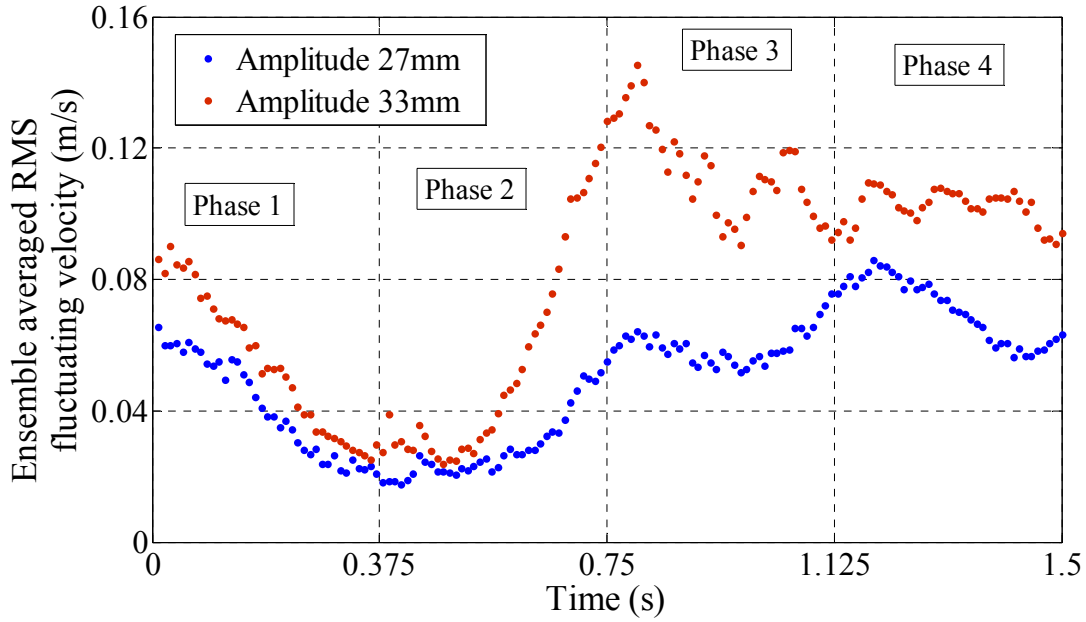

3.10(b) Central Region

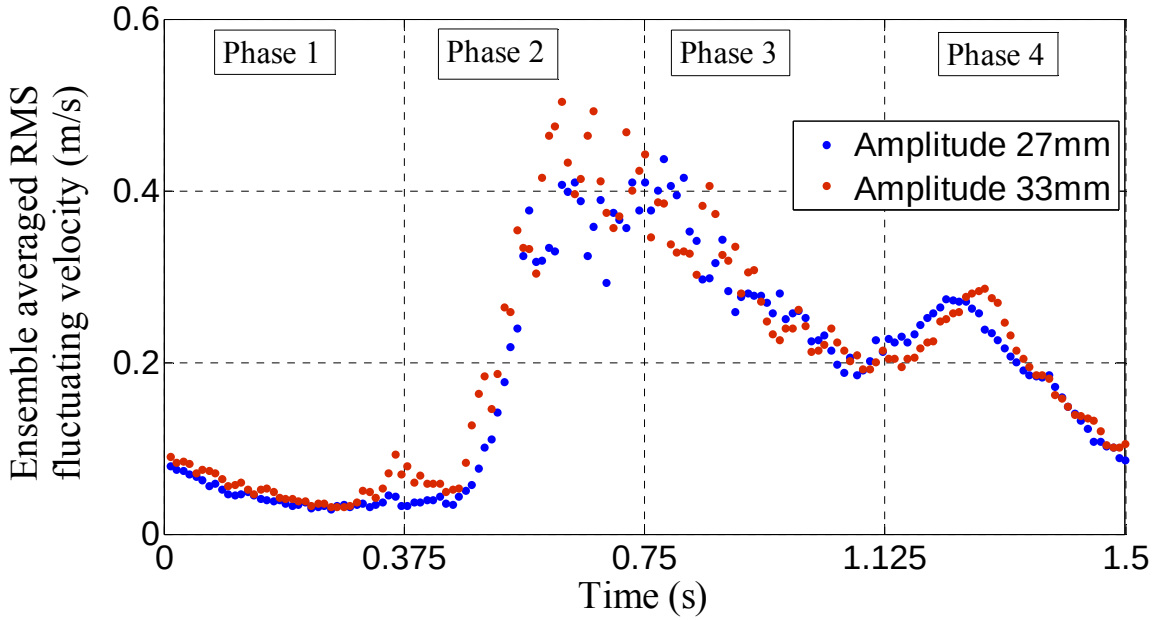

3.10(c) Base Region

Figure 3.10: Variation of ensemble averaged RMS fluctuating velocity with amplitude at a fixed frequency of 0.665 Hz

3.3.3 Agitation Velocity Study

A study was done to document the effect of agitation velocity on heat transfer and velocity. The agitator peak velocity can be given as :

$$V_{peak}=2\pi Af \qquad (3\text{-}1)$$

where V_{peak} is the peak agitation velocity, A is the amplitude of oscillation and f is the frequency of oscillation. We were interested in discerning if the convective heat transfer was simply governed by the peak agitation velocity irrespective of the amplitude and frequency of agitation, separately. That is, under a fixed agitation velocity, "is amplitude or frequency more important than the other?"

Table 3.2 shows the cases being studied and the corresponding agitation velocities.

Table 3.2: Agitation velocities and amplitude/frequency values for the corresponding velocities

Agitation velocity (m/s)	Amplitude(mm) Mean to peak	Frequency (Hz)
0.11	27	0.665
0.11	33	0.547
0.17	27	1
0.17	33	0.82
0.23	27	1.3
0.23	33	1.1

From Figure 3.11(a), it can be seen that within limits of experimental uncertainty, the heat transfer coefficient for the entry region is mainly governed by agitation velocity. At a fixed agitation velocity, amplitude seems to be only slightly effective in enhancing heat transfer but that increase is within limits of experimental uncertainty. From Figure 3.12(a), it can be seen that the ensemble-averaged mean velocity data for the entry region show an overlap for cases with different frequencies and amplitudes but with the same agitation velocity, with slight variations during certain phases. During phase 1, the higher amplitude case has a slightly higher velocity whereas at the end of phase 2 and beginning of phase 3, the higher frequency case has a higher mean velocity. However, these slight differences do not seem to be affecting the heat transfer coefficient in a major way. From Figure 3.13(a), it can be seen that during phases 3 and 4, the higher amplitude case has a higher fluctuating velocity. During phase 3, the mean flow is decelerating; therefore

turbulence production is high. Higher amplitude is leading to production of more turbulence. This was also noticed in section 3.3.2 and Figure 3.10(b). However, this slightly higher production of turbulence for one phase of the cycle, does not contribute to significant enhancement in heat transfer, as seen in Figure 3.11(a).

From Figure 3.11(b), for the central region, it can be seen that for certain agitation velocities, amplitude is slightly more effective in enhancing heat transfer, but that the increase is again within limits of experimental uncertainty. For a specific agitation velocity, the mean velocity curves (Figure 3.12(b)) mostly overlap well for the central region, except during phase 4, when higher amplitude case approaches a deceleration phase faster than in the lower amplitude case. This faster approach of the deceleration phase during phase 4 in Figure 3.12(b) was also noted in Figure 3.9(b) when the mean velocity curves were compared for two amplitudes at the same frequency. From Figure 3.13(b), it can be seen that higher amplitude case shows higher fluctuation velocities during phases 2 and 3 for the central region. Phase 2 has decelerating mean flow for cases having the same agitation velocity but different amplitude and frequency combinations. At the same agitation velocity, phase 3 has an accelerating flow for lower amplitude and a more rapidly approaching decelerating phase for the higher amplitude. Higher amplitude favors more turbulence production during the decelerating phases. This might lead to slight increases in heat transfer, as observed in Figure 3.11(b), but the slight increase is within the limits of experimental uncertainty, as noted earlier.

As seen in Figure 3.11(c), the base region has overlapping heat transfer coefficients at a fixed agitation velocity, except for the higher velocity case. With the highest agitation velocity, it can be seen that a higher frequency case has slightly higher heat transfer

coefficients, but, again, within the limits of experimental uncertainty. From Figure 3.12(c), it can be seen that the mean velocity curves generally overlap well for higher and lower amplitude cases at a fixed agitation velocity. At higher agitation velocities, for the higher amplitude case, the mean velocity is slightly higher during parts of phases 1 and 2. From Figure 3.13(c), it can be seen that the fluctuating velocity curves overlap well for two cases at fixed agitation velocities, except for at higher agitation velocities when the higher frequency case shows slightly more velocity fluctuation during phases 3 and 4.

In general, it can be concluded that agitation velocity is the governing factor for enhancing heat transfer, as described earlier and observed in Figure 3.11. This is also supported by the mean and ensemble-averaged velocity plots shown in Figures 3.12 and 3.13 with slight variations during certain phases.

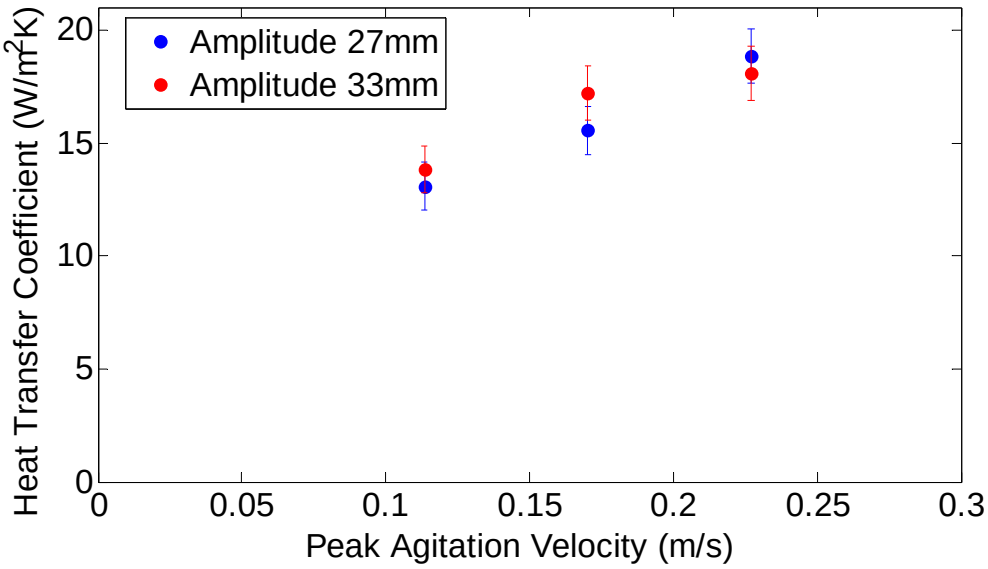

3.11(a) Entry Region

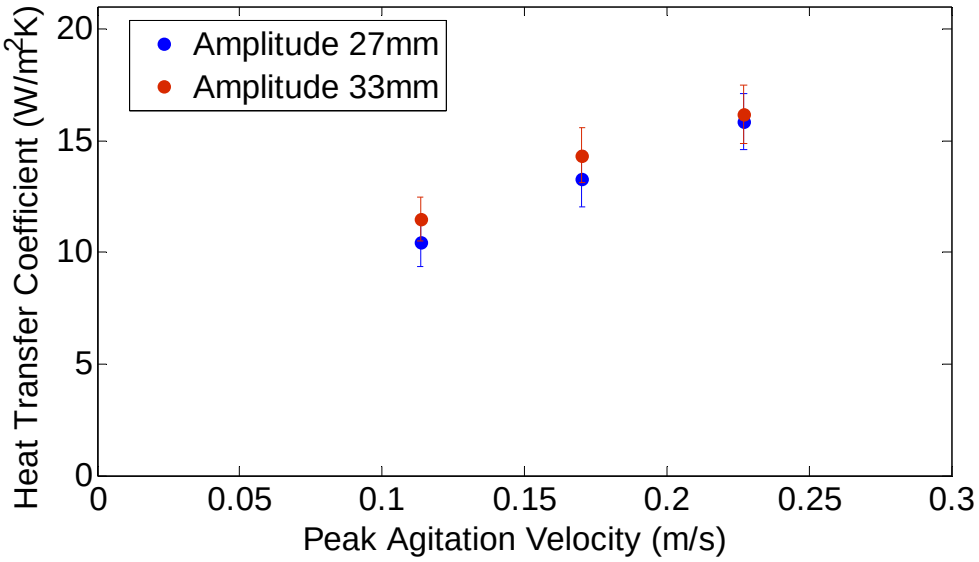

3.11(b) Central Region

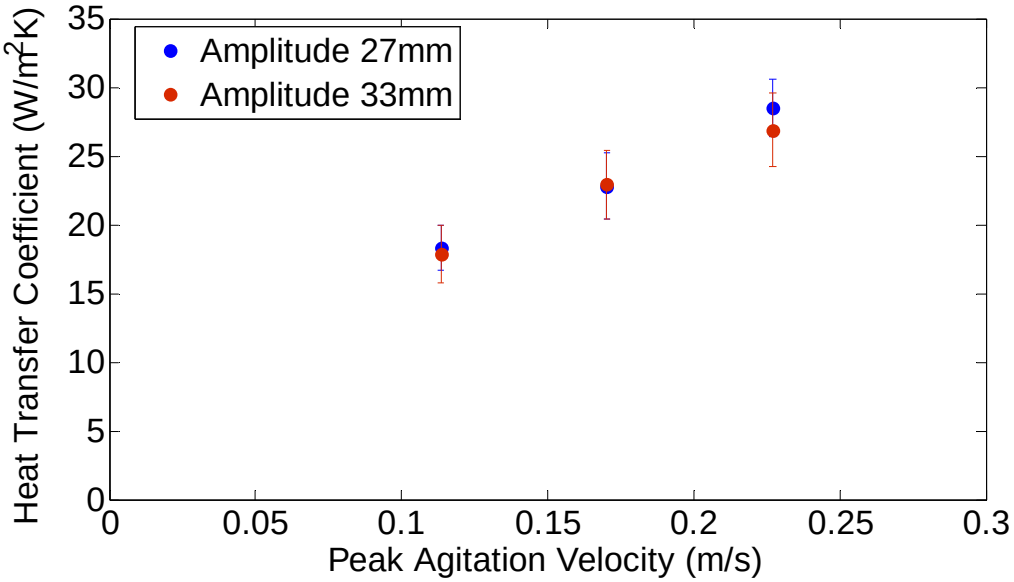

3.11(c) Base Region

Figure 3.11: Variation of heat transfer coefficient with peak agitation velocity

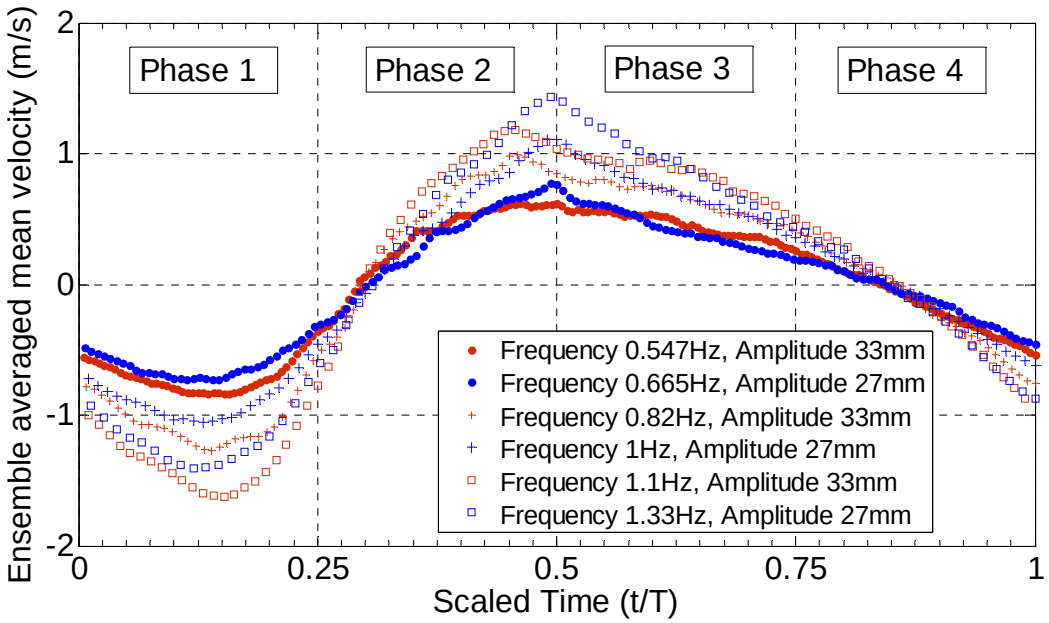

3.12(a) Entry Region

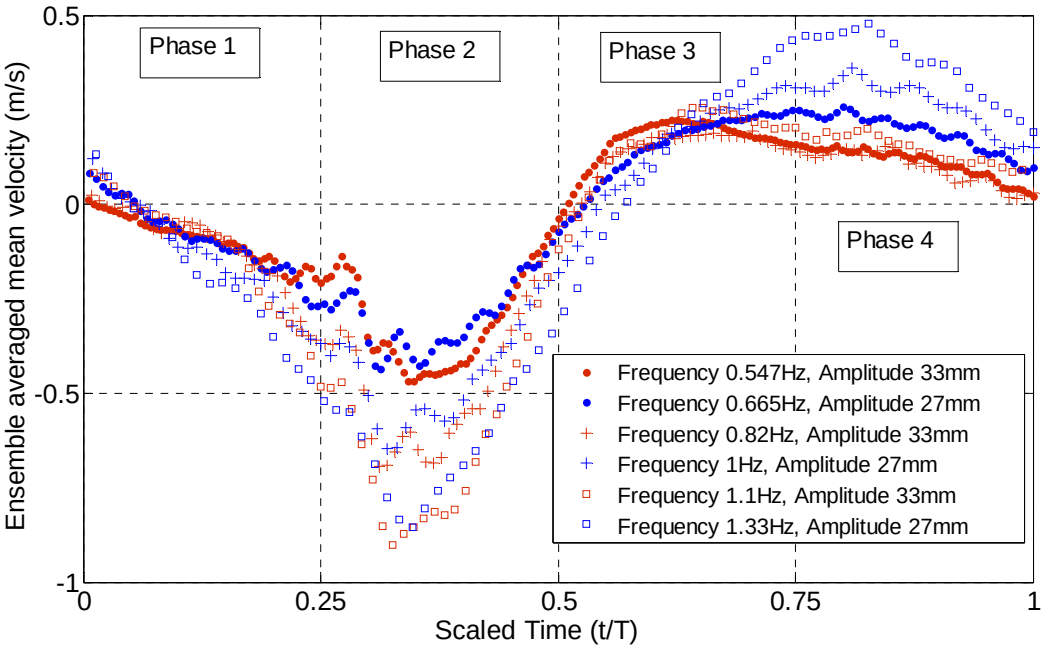

3.12(b) Central Region

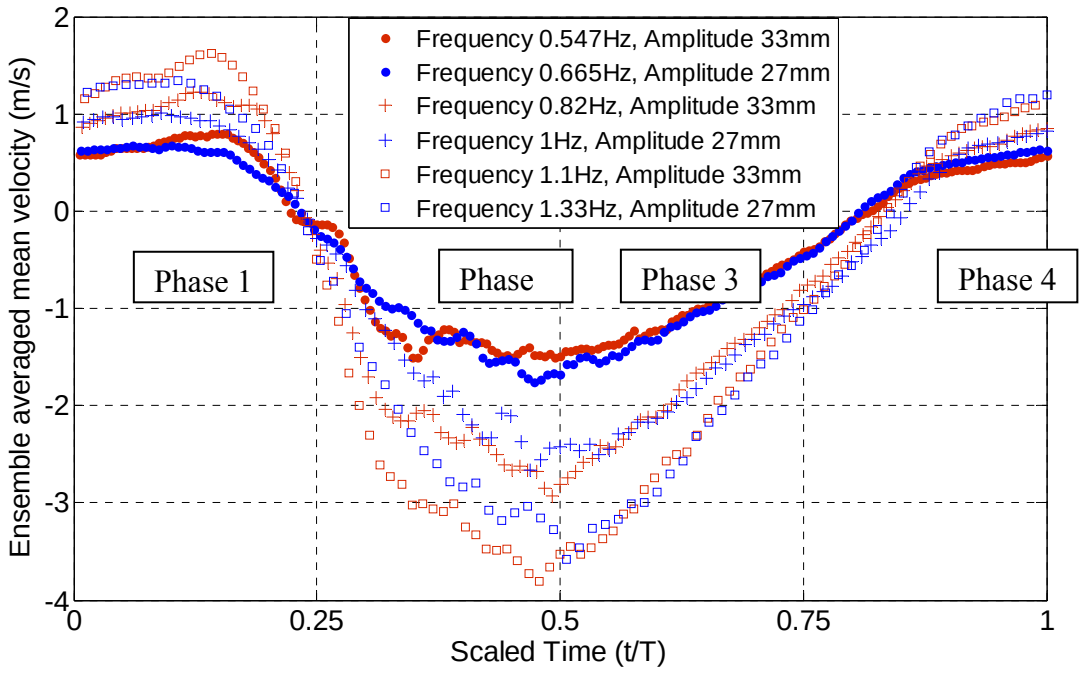

3.12(c) Base Region

Figure 3.12: Variation of ensemble averaged mean velocity with agitation velocity; agitation velocity=0.11 m/s (top two of legend), agitation velocity=0.17 m/s (middle two of legend), agitation velocity=0.23 m/s (bottom two of legend)

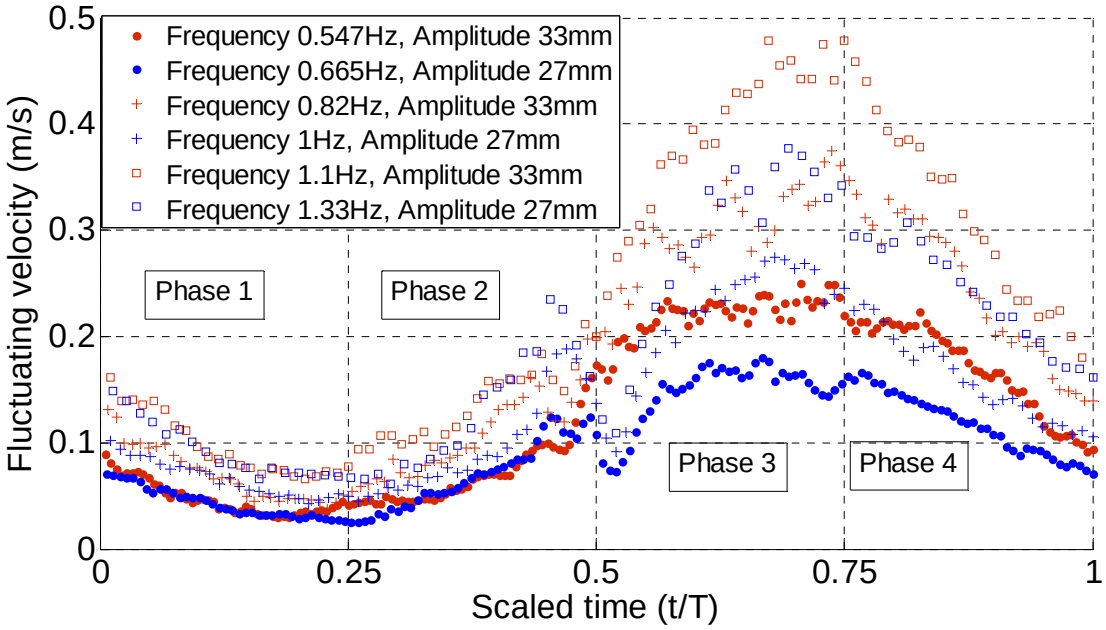

3.13(a) Entry Region

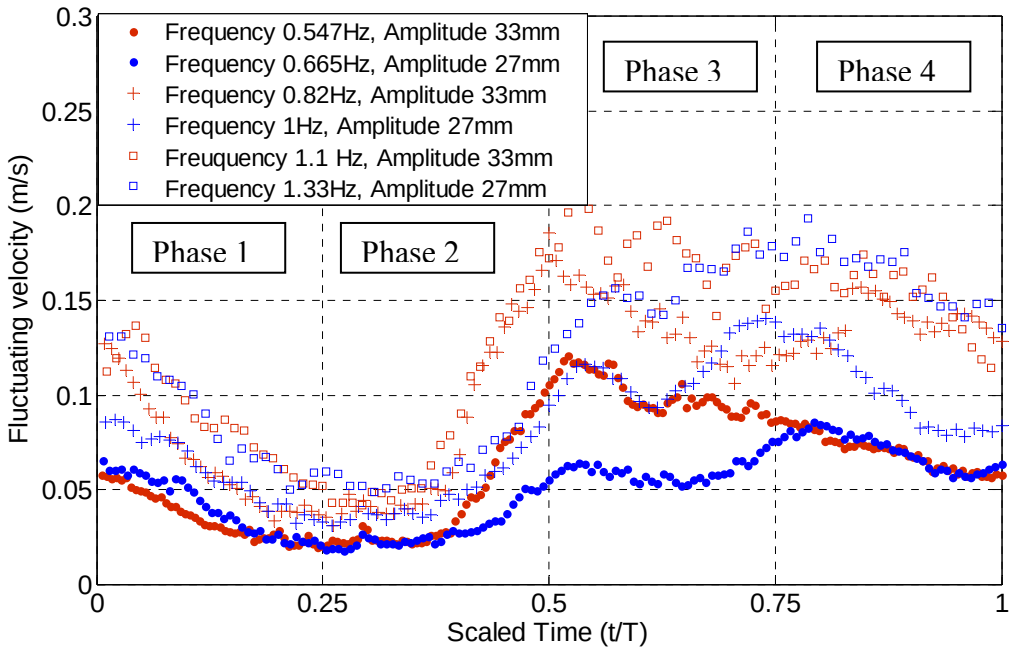

3.13(b) Central Region

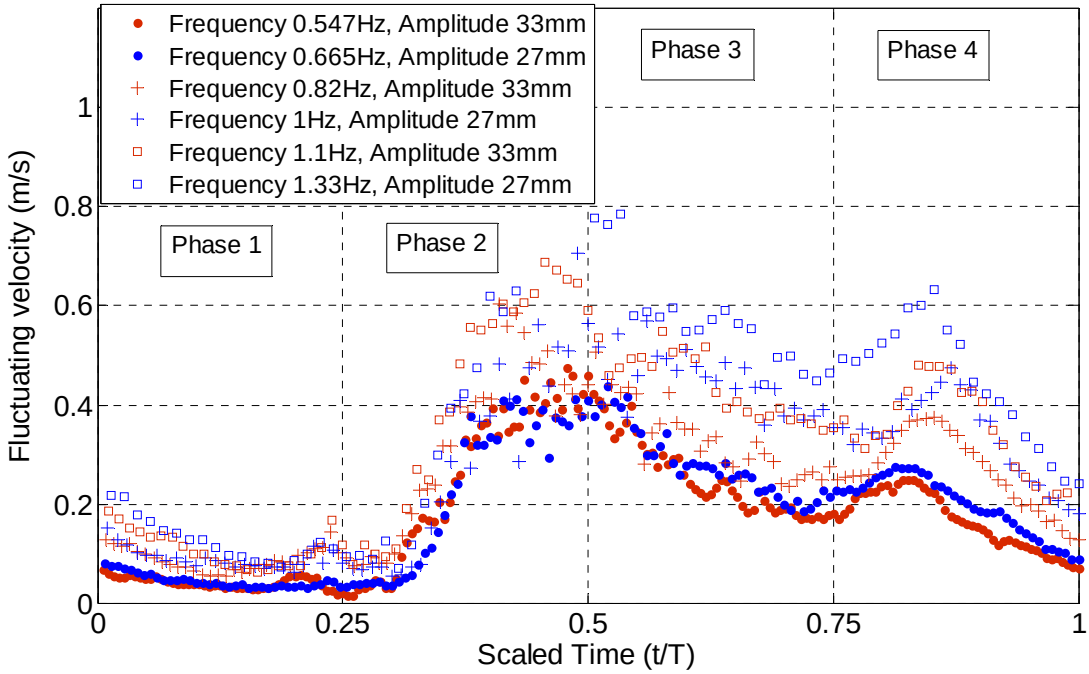

3.13(c) Base Region

Figure 3.13: Variation of ensemble averaged RMS fluctuating velocity with agitation velocity; agitation velocity=0.11 m/s (top two of legend), agitation velocity=0.17 m/s (middle two of legend), agitation velocity=0.23 m/s (bottom two of legend)

3.4 Unsteady Heat Flux

Unsteady heat flux measurements were done on all the three regions for a frequency of 0.665 Hz and an amplitude of 27 mm.

As can be seen from Figure 3.14(a) for entry region, the unsteady heat flux peaks at the end of phase 3 and beginning of phase 4. When compared with the ensemble averaged fluctuating velocity plot in Figure 3.5, it can be seen that the fluctuating velocity peaks during phase 3 and starts to drop down during phase 4 of the agitator motion. It appears that the heat flux in the entry region is affected by the ensemble averaged fluctuating velocity. The unsteady heat flux shows a lag in response to the fluctuating velocity curve.

For central region, from Figure 3.14(b), it can be seen that the unsteady heat flux reaches a maximum value when phase 1 ends and phase 2 begins. The unsteady flux also reaches a peak value within phase 3. Compared with the ensemble averaged mean velocity plots for the central region in Figure 3.4, it can be seen that the ensemble averaged mean velocity reaches a peak value during phase 2 and at the end of phase 3. Thus, the unsteady heat flux in the central region is more affected by acceleration and deceleration of the flow than by turbulence. In the central region, the flow is a pressure-gradient-driven sloshing flow. The near-wall region responds faster than the core flow, and the heat transfer correlates better with the near-wall flow. This is the reason that, when the mean velocity plot and the unsteady heat flux plot are compared, it can be seen that the mean velocity plot shows a lag behind the unsteady heat flux plot.

From Figure 3.14(c) for base region, it can be seen that the unsteady heat flux shows a peak during phase 3 whereas from Figure 3.5 it can be seen that the fluctuating velocity peaks at the end of phase 2 and beginning of phase 3. The heat transfer in the base region

is more affected by the fluctuating velocity and therefore it is more influenced by the turbulence. The unsteady heat flux shows a lag with the fluctuating velocity curve.

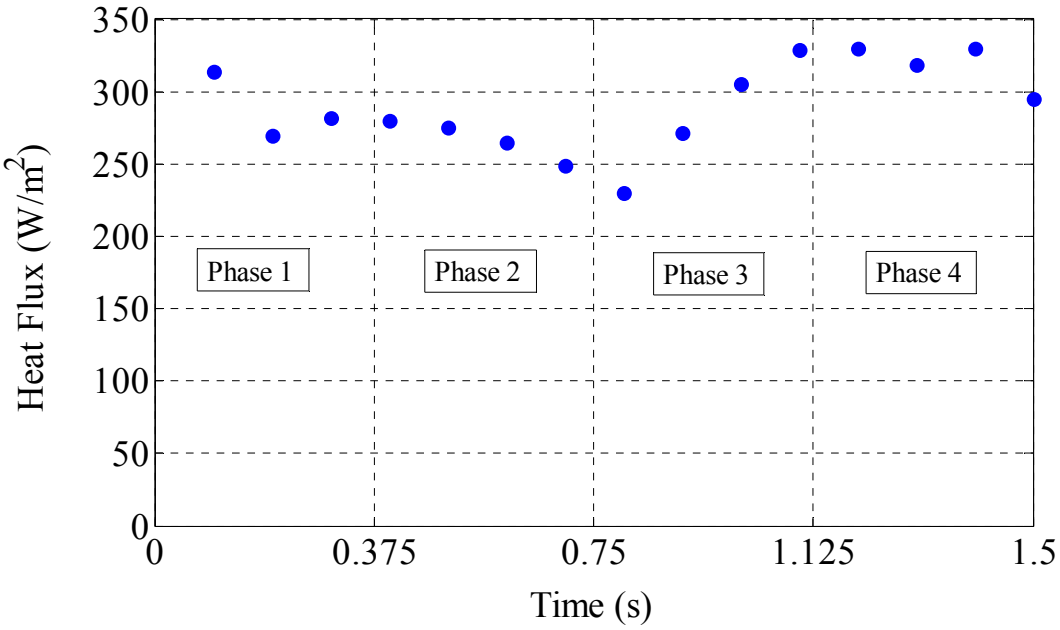

3.14(a) Entry Region

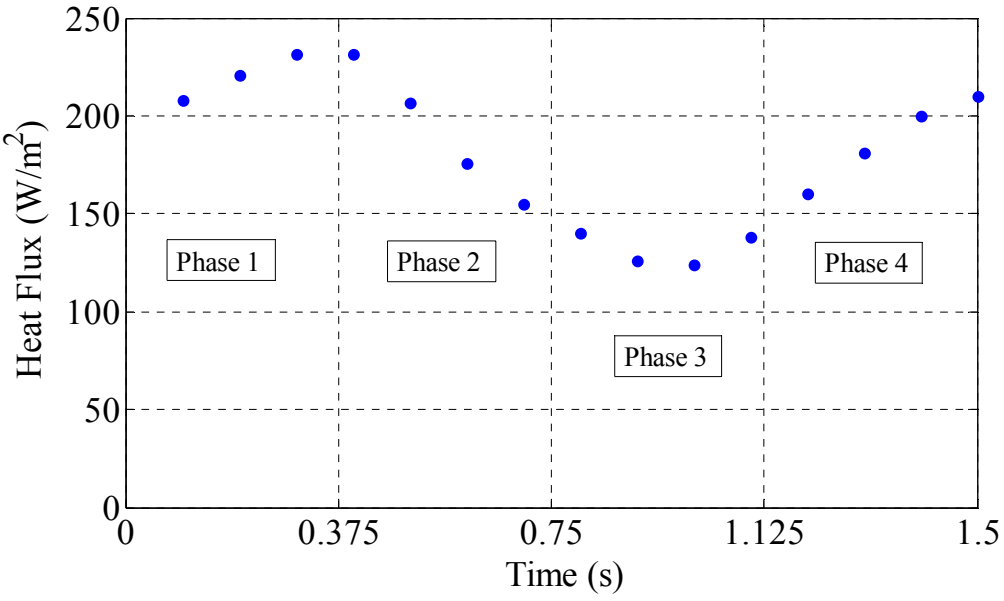

3.14(b) Central Region

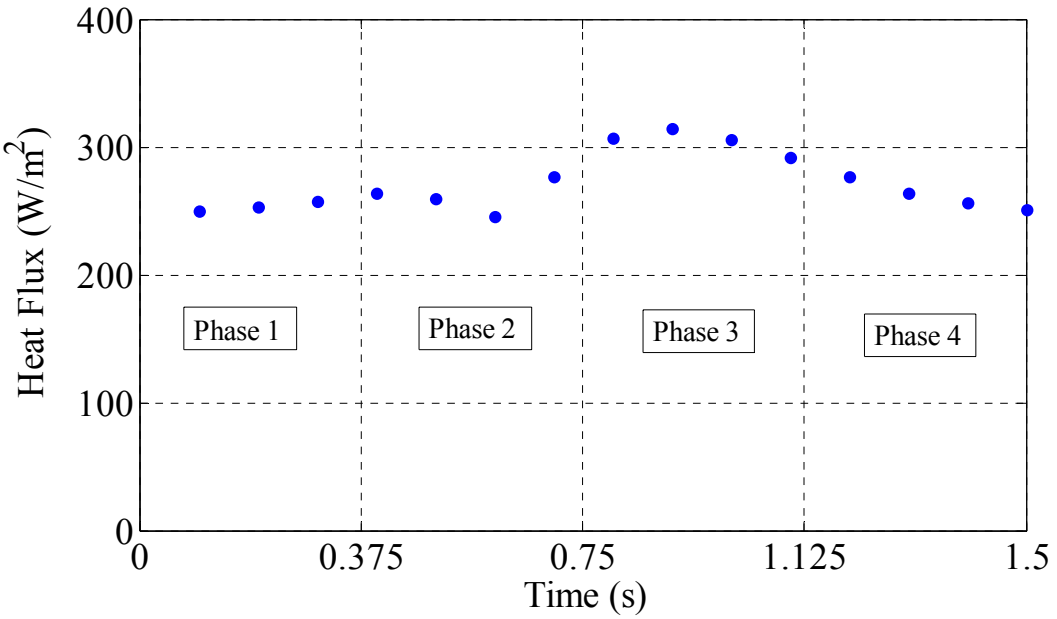

3.14(c) Base Region

Figure 3.14: Unsteady heat flux for three regions at a frequency of 0.665 Hz and an amplitude of 27 mm

3.5 Simulations

Simulations were run using ANSYS FLUENT to verify the heat transfer results. Dynamic meshes were employed using a user defined function. These simulations were not easy to implement due to the moving agitator wall and the deforming computational domain. The extent of the computational domain in the spanwise direction (shown in Figure 3.15(b)) was less than the span length in actual experiments to reduce the number of cells used. As can be seen in the Figure 3.15(a), there is a refined domain to increase the near wall resolution. We would have ideally liked to put more cells near the wall; however, the deforming domain posed restrictions on refining the grid too much beyond a point due to the computational time used and also deteriorating mesh quality. Computations were run for around 8 oscillation cycles so that the flow and heat transfer could reach a steady state. However, with each successive cycle, the mesh quality deteriorates due to

increasing skewness of the cells. This poses a restriction on the refinement we can get, because smaller the cell size, more is the skewness. As the skewness of the cells increases, the mesh quality deteriorates and the simulation does not run further. The computational domain has a total number of 1085950 cells and 1208532 nodes.

3.5.1 Heat Transfer

The heat transfer results from simulations do not show a good match with the experiments. This is because the near-wall mesh resolution is not as good as required. The best refinement that can be obtained away from the wall is 1 mm which is not sufficient to accurately calculate near-wall temperature profiles. Further refinement at the wall was attempted but ANSYS FLUENT could not mesh the domain as the total mesh size became too large. Also, even if such a fine mesh was possible, it would take huge computational time to run the simulation which was not practical. The more dense the mesh is, the more time is needed to remesh the domain at every time step due to deforming meshes. Thus, with a very fine mesh, one also runs into the problems of having negative cell volumes which leads to mesh failure.

The boundary conditions for the simulation have been shown in Figure 3.15(b). Computations were done with two different models-the laminar model, and the LES (Large Eddy Simulation) model available in FLUENT.

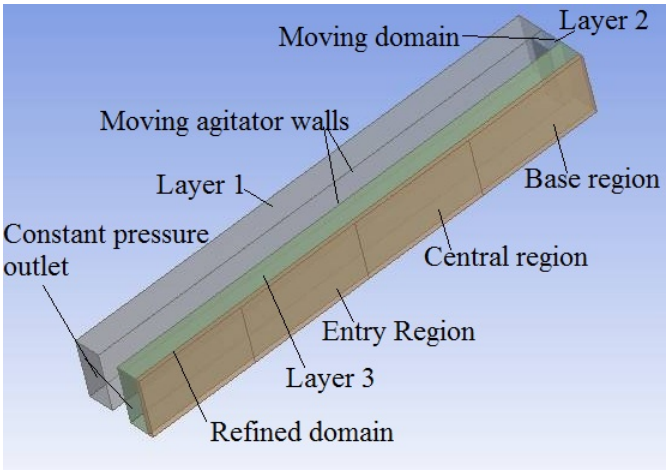

3.15(a) Channel with moving domains

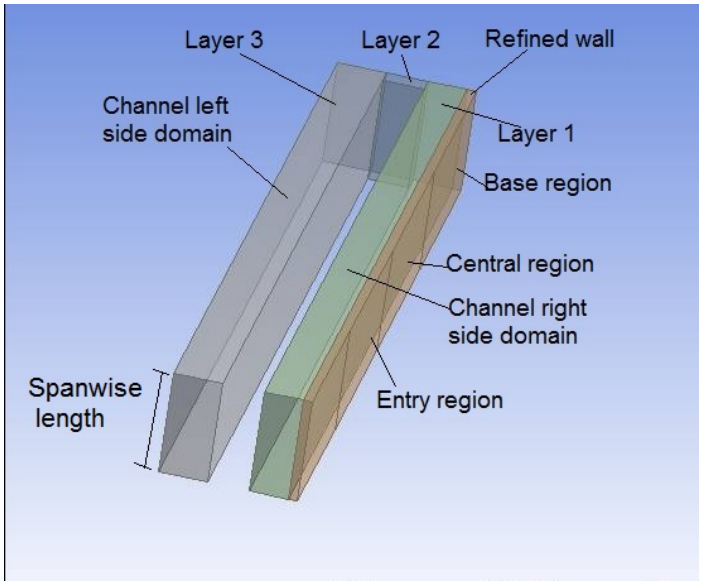

3.15(b) Channel domain with boundary conditions

Figure 3.15: Computational domain for the mock up channel

Table 3.3(a): Heat transfer coefficients (W/m^2K); comparisons of simulations and experiments with a laminar model

	Entry Region	Central region	Base Region
Simulation	4.81	4.6	12.73
Experiment	13.09	10.42	18.33

Table 3.3(b): Heat transfer coefficients (W/m^2K); comparisons of simulations and experiments with an LES model

	Entry Region	Central region	Base Region
Simulation	5.1	4.7	11.4
Experiment	13.09	10.42	18.33

3.5.2 Velocity Plots

Figure 3.16 shows the comparison of ensemble-averaged mean velocity for each of the three regions at a frequency of 0.665 Hz and an amplitude of 27 mm. The mean velocity curves for experiments and simulations overlap closely with each other. The simulations were run for around 8 cycles. This was not enough to compute the ensemble averaged fluctuating velocity. More cycles could not be run because the mesh quality deteriorated after around 7-8 cycles. As the mean velocity curves overlap closely, plots from simulations have been used for flow visualization. These plots have been presented in the later section.

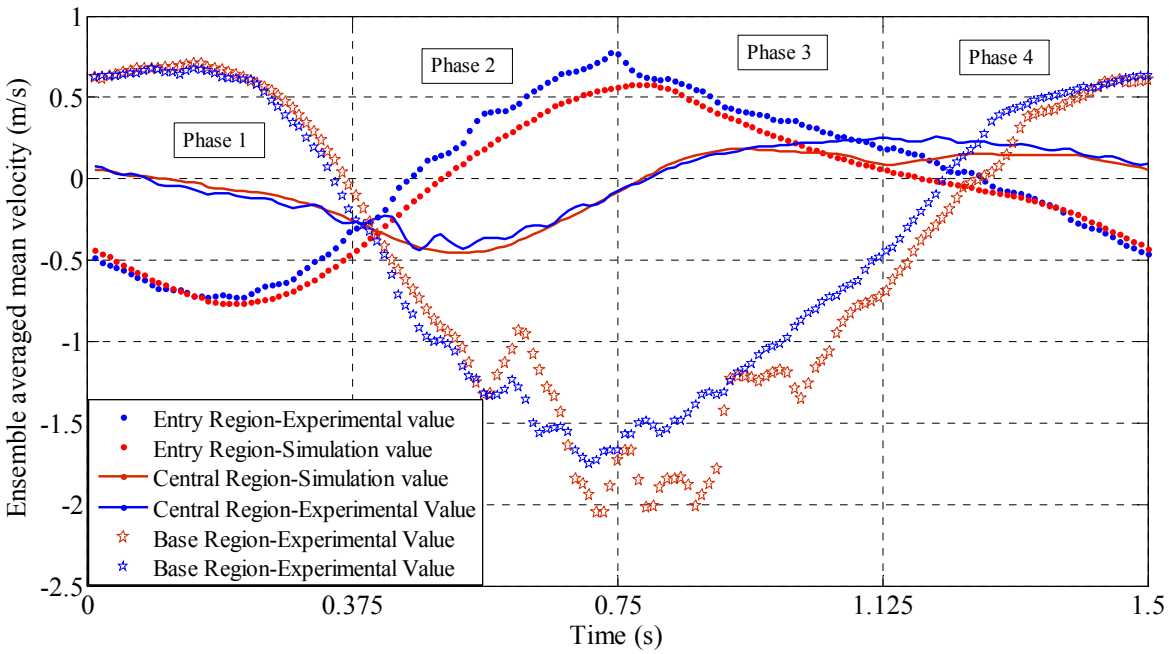

Figure 3.16: Ensemble averaged mean velocity comparison for experiments and simulations at a frequency of 0.665 Hz and an amplitude of 27 mm (mean to peak)

3.5.3 Flow Visualization

A flow visualization study by computation was done using ANSYS FLUENT to study the distribution of the wall-parallel component of velocity in the channel domain. Contours are plotted in Figure 3.17 for each of the four stages shown in Figure 3.1.These contours are plotted for a frequency of 0.665 Hz and an amplitude of 27 mm (mean to peak). These contours further help in understanding the velocity variations studied in the plots of sections 3.2.1, 3.2.2 and 3.2.3.

As can be seen in Figure 3.17, during phase 1, when the agitator just starts moving toward the right wall, half of the channel length has flow moving in the positive-y direction and the other half has flow moving in the negative-y direction. The change in direction is somewhere within the central region. Vortical activity starts to appear in the base region, due to the narrow gap between the agitator and the tip wall. At the beginning

of phase 2, velocities are low in the base region compared to velocities in the rest of the cycle. Velocities are higher left of the agitator plate than right. At the beginning of phase 3, flow is moving into the entry region in the positive direction with high velocities. This can also be seen in Figure 3.4. Within the central region, there is a change in the direction of the flow relative to that of the entry region. As explained earlier, this change is influenced by the streaking activity in the base region. At the beginning of phase 4, when the agitator begins to move from the left wall to the mean position, streaking in the base region has weakened.

The contour plots show that the agitator causes strong disturbances in the flow domain during the different stages of the cycle.

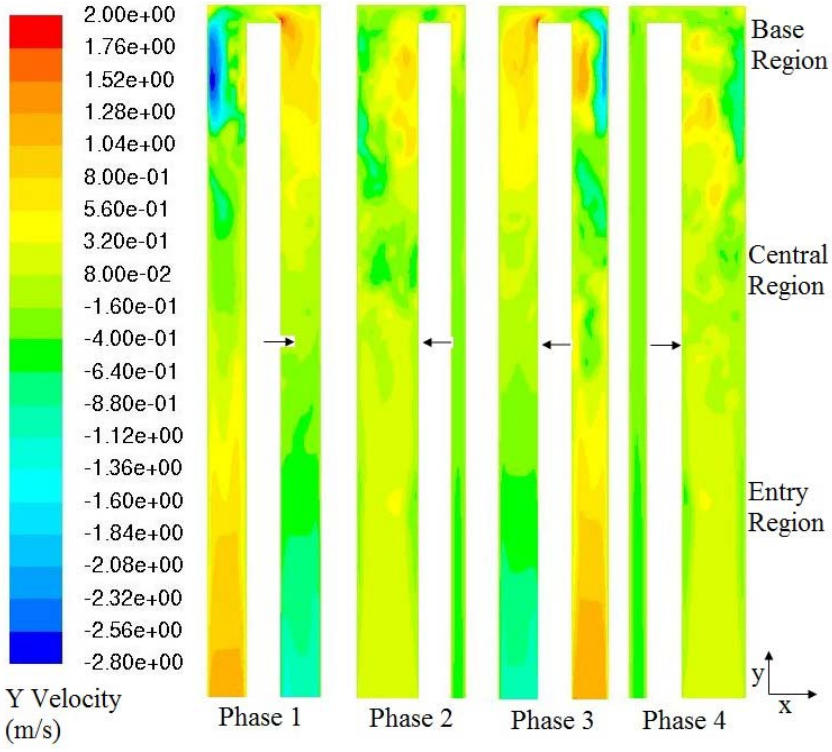

Figure 3.17: Y-velocity contours during different stages of agitator motion

Chapter 4

Velocity and Heat Transfer for the Case with Wall Attached Pin Fins

Heat transfer and velocity measurements were done on a channel wall augmented with pin fins. The pin fins were placed on the channel wall in a staggered manner. Pin fins were added to the heat transfer surface to assess the heat transfer enhancement that can be obtained on the augmented surface. Pin fins lead to an increase in the overall heat transfer surface and generate additional turbulence. Heat transfer coefficients based both on the total wetted area and the plain wall area have been calculated to compare the performance of the pin fin surface relative to the plain surface. Figure 4.1 shows the staggered arrangement of pin fins on a channel wall as fabricated for the heat transfer measurements.

The arrangement of pin fins for velocity measurements can be noted in Figure 4.2. As can be seen in Figure 4.2, a column of pins is missing. This was done to avoid blockage of laser beams by pin fins. Without removing a column of pins, it would not be possible to measure velocities since the gap between consecutive columns of pins was not wide enough to allow the laser beams to pass through. It was concluded that the measured velocity was giving information about the velocity field of the flow that had passed through the pin fin array immediately upstream. Figure 4.3 shows the intersection of laser beams between the pin fins for velocity measurements.

Figure 4.4 shows the arrangement of the laser probe on the channel wall for measurements of velocity in the presence of pin fins.

Figure 4.1: Staggered arrangement of pin fins on channel wall for heat transfer measurements

Figure 4.2: Arrangement of pin fins on channel wall for velocity measurements

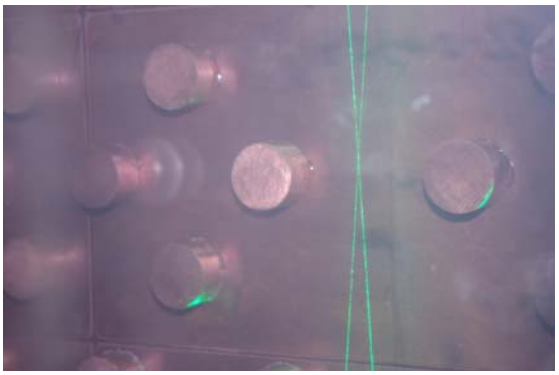

Figure 4.3: Laser beams intersecting between the pin fins for velocity measurements

Figure 4.4: Laser probe arrangement on channel wall augmented with pin fins

In this chapter, a comparison of plain wall and pin fin heat transfer results is presented. Comparison of velocity data are also discussed. Following that, the results of a parametric study carried out in the presence of pin fins are presented.

4.1 Heat Transfer in the Presence of Pin Fins

Figure 4.5(a) shows the variation of heat transfer coefficient with pin fins with agitation velocity for the entry region. To get the details of the agitator velocity and the corresponding amplitude and frequency values, one can refer to Table 3.2 in Chapter 3. As can be seen from Figure 4.5(a), if one computes the heat transfer coefficient in the presence of pin fins based on the projected area (flat plain wall area), one can see around 35-40% enhancement when compared with plain wall heat transfer coefficients. When the heat transfer coefficient is calculated based on the total wetted area, one can note around 5% enhancement in heat transfer coefficient when compared with the plain wall heat transfer coefficient, and an increase in area of around 30%. At a particular agitation velocity, the heat transfer coefficient in the presence of pin fins remains the same irrespective of the value of amplitude or frequency for the entry region. This was also concluded in Chapter 3 in the presence of a plain wall.

Figure 4.5(b) shows the heat transfer coefficient variation with agitation velocity in the presence of pin fins for the central region. For an amplitude of 27 mm, around 35% enhancement can be observed due to the addition of pin fins when the heat transfer coefficient is calculated based on the projected area. For an amplitude of 33 mm, around 25% enhancement can be observed when the heat transfer coefficient is calculated based on the projected area. When the heat transfer coefficient is calculated based on the total wetted area, a 3-4% enhancement can be observed in the case of 27 mm amplitude, whereas a slight decrease of around 3-4% can be noted when the amplitude is 33 mm. Thus, for central region, a lower oscillation amplitude might provide slightly more benefit in the presence of pin fins. However, this slight benefit observed for the lower-

amplitude case is also within the limits of experimental uncertainty. At a constant agitation velocity, which is governed by the product of frequency and amplitude, the heat transfer coefficient seems to be unaffected by a change in frequency or amplitude. This observation was also made for the plain wall case.

Figure 4.5(c) shows the heat transfer coefficient variation with agitation velocity for the base region. When the heat transfer coefficient is computed based on the projected area, an increase of around 25% can be observed both for amplitudes 27 mm and 33 mm. However, when the heat transfer coefficient is calculated based on the total wetted area, a decrease of around 4-5% can be observed when compared with the plain wall area. At a particular agitation velocity, the heat transfer coefficient is mainly governed by agitation velocity irrespective of the value of amplitude or frequency as was noted for other regions.

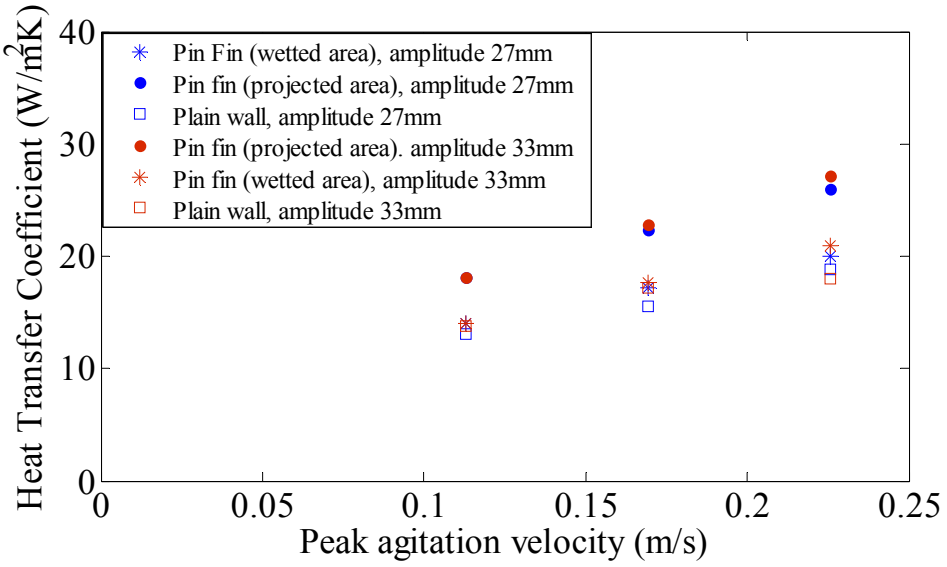

4.5(a) Entry Region

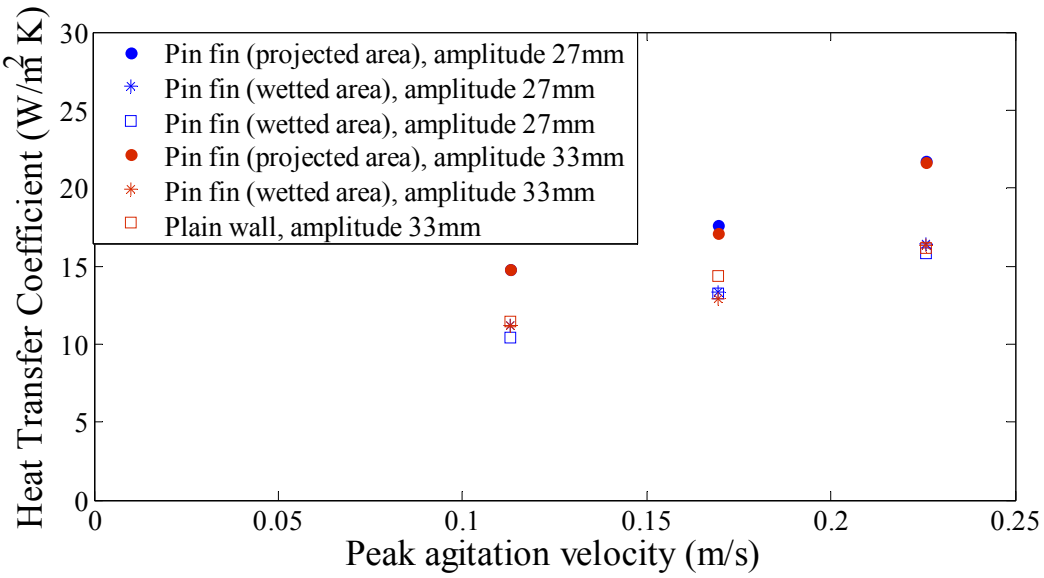

4.5(b) Central Region

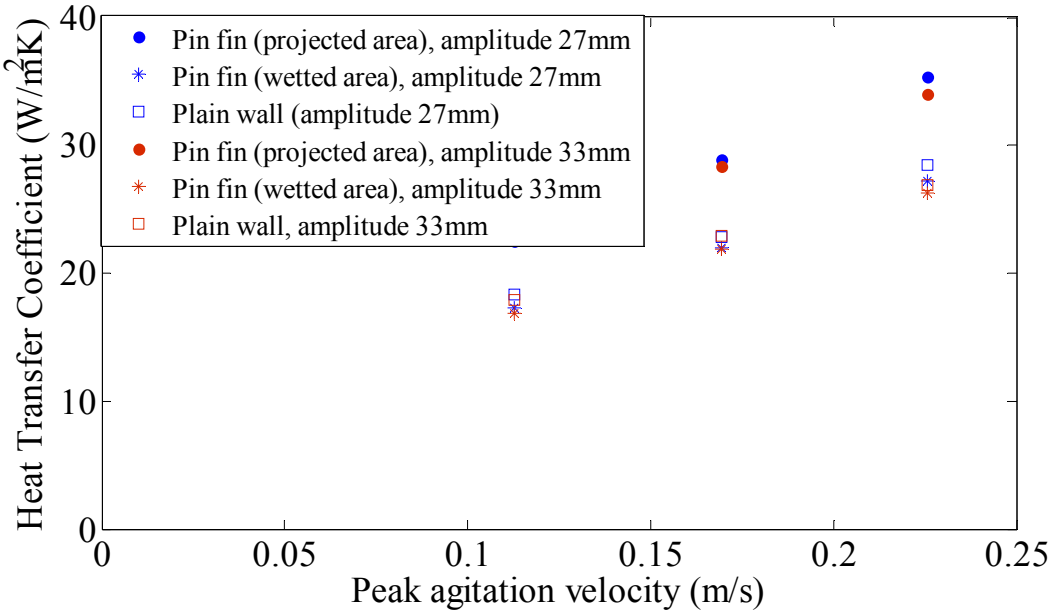

4.5(c) Base Region

Figure 4.5: Heat transfer coefficient vs. agitation velocity for channel augmented with pin fins

4.2 Velocity Comparison Plain Wall vs. Pin Fins

4.2.1 Entry Region

Figure 4.6(a) shows the ensemble averaged mean velocity plots for the entry region at a frequency of 0.665 Hz and an amplitude of 27 mm (mean to peak). The plot shows the ensemble averaged mean velocity at two wall-normal distances, 8 mm and 14 mm. Since the pin fin height is 10 mm, a wall normal distance of 8 mm is just 2 mm below the pin fins. As can be seen from the plot, the variation in velocity with wall-normal distance is more when the pin fins are added to the channel wall. The wall normal variation is less in the case of a plain wall. When the mean velocity profiles are compared at a wall-normal distance of 8 mm for a plain wall and a pin fin wall, one can see that the pin fin wall experiences some momentum loss. At a wall normal distance of 14 mm, less momentum loss is experienced in the case of pin fins when compared to that at a wall-normal distance of 8 mm.

When the mean velocity profiles are compared for a plain wall and a pin fin wall for the entry region at a frequency of 0.665 Hz and an of amplitude of 33 mm, Figure 4.7(a), one can see that the pin fin velocity profiles show less momentum loss, compared to the lower-amplitude case. One can also see increased variation in the mean velocity profile for the higher amplitude case. Thus, with higher amplitude, the agitator has the tendency to push the flow into the pin fin array. However, with the lower amplitude, the flow has a tendency to go over the top of the pin fins rather than go into the pin fin forest.

Figure 4.8(a) shows the fluctuation velocity comparison for pin fins and plain wall for the entry region at a frequency of 0.665 Hz and an amplitude of 27 mm. The pin fins show higher velocity fluctuation than in the plain wall case, in general. During phase 1, higher

fluctuation velocity is observed at a wall normal distance of 8 mm whereas during phase 3, higher fluctuation velocities were observed for a wall normal distance of 14 mm. During half of phase 1, the mean flow is decelerating for the plain wall case, and flow at a wall-normal distance of 8 mm experiences more momentum loss than that at a wall-normal distance of 14 mm; however, higher fluctuation velocities are observed at a wall-normal distance of 8 mm during part of phase 1. Thus, some of the mean flow momentum loss is compensated by increased mixing during phase 1 for a wall-normal distance of 8 mm for the pin fin wall. During the end of phase 2 and the beginning of phase 3, higher fluctuation velocities are observed at a wall-normal distance of 14 mm. At a wall-normal distance of 14 mm, the velocity profile is similar to the flat wall velocity profile except for that in phase 3; however, the reduced mean flow momentum for a wall-normal distance of 14 mm is compensated by an increased fluctuation velocity. Flow deceleration in general leads to increased turbulence, as was noted in Chapter 3, this turbulence production is enhanced in the presence of pin fins for different deceleration phases at different wall normal distances. Figure 4.9(a) shows the ensemble averaged fluctuation velocity profile comparison for plain wall and pin fin wall for a frequency of 0.665 Hz and an amplitude of 33mm. Phase 1 shows mean flow acceleration followed by deceleration. During this phase, the agitator is moving closer to the channel wall. As the agitator pushes flow into the pin fin array and comes close to the channel wall, there is an increase in velocity fluctuation. During phase 2, flow deceleration approaches faster for the pin fin wall case than for the plain wall case. Thus, the pin fin wall experiences an increase in fluctuation during phase 2. However, as the rapid flow deceleration continues for the pin fins during most of phase 3, the pin fin cases experience lower velocity

fluctuation levels than those of the plain wall cases. The observed mean velocity with pin fins is lower during phase 3, and thus, lower levels of fluctuation are found.

4.2.2 Central Region

Figure 4.6 (b) shows the variation of ensemble averaged mean velocity for the central region at a frequency of 0.665 Hz and an amplitude of 27 mm, both for the plain wall and the pin fin wall. As was discussed in Chapter 3, the central region being in the center of the channel gets influenced by the entry region and the base region flow characteristics. During phase 1, when the agitator is moving toward the channel wall, the velocity trends for a plain wall case and a pin fin wall case are the same at all wall-normal distances. During phase 2, it can be seen that the presence of pin fins speeds up the change in direction of flow from negative to positive when compared to that of the plain wall case. For the plain wall case, flow in the central region is more influenced by the fluid being drawn into the channel in the base region during phase 2. However, as can be noted from Figure 4.6(c), the strength with which the fluid is drawn into the channel in the base region during phase 2 weakens considerably due to the presence of the pin fins. Thus, the influence of the base region on the central region weakens, and the change in direction of fluid approaches faster when the pin fins are present, compared to that of the plain wall case. During phases 3 and 4, flow direction is positive, indicating that fluid is getting drawn into the channel in the central region. During phase 3, the agitator is moving from the mean position to the opposite channel wall, flow is entering the channel from the entry region and the central region is influenced by the entry region. The flow inside the pin fin array, at a wall normal distance of 8 mm, suffers a momentum loss and tends to slow down, however the core flow outside the pin fin array at a wall-normal distance of

14 mm, shows acceleration and has a magnitude greater than that for the plain wall. During phase 4, as the flow continues to move in the positive direction in the central region, flow at the wall normal distance of 8 mm shows acceleration but is still lower in magnitude than that of the plain wall case. Flow at a wall-normal distance of 14 mm shows deceleration, but continues to be higher in magnitude than that in the plain wall case. When the fluid is being drawn into the channel, the core flow outside the pin fin array shows increased velocity compared to that for the plain wall but the flow inside the pin fin array shows a loss of momentum in comparison to that of the plain wall case.

Figure 4.8(b) shows the variation of ensemble averaged RMS fluctuating velocity for the central region at a frequency of 0.665 Hz and an amplitude of 27 mm. As was noted earlier, during phase 1, when the agitator is coming toward the channel wall and flow is being pushed out of the channel, the central region mean flow characteristics for pin fin wall were similar to those of plain wall. The same trend is observed for the fluctuating velocity during phase 1. During phase 2, as the deceleration phase is accelerated due to the presence of pin fins, one can see a rise in the fluctuating velocity at a wall normal distance of 14mm for the pin fin case. This rise in fluctuating velocity starts to drop as the acceleration phase is approached during phase 3. During phase 3, flow in the central region shows deceleration followed by acceleration in phase 4 at a wall normal distance of 8mm. Thus, the fluctuating velocity rises during phase 3 and drops down during phase 4, at a wall normal distance of 8 mm. At a wall normal distance of 14 mm, deceleration begins in the middle of phase 3; thus, fluctuating velocity starts rising between phase 3, reaching a peak during phase 4 and starts dropping as the deceleration phase continues during phase 4.

Figure 4.7(b) shows the comparison of ensemble averaged mean velocity for a plain wall case and a pin fin wall case for the central region at a frequency 0.665 Hz and an amplitude of 33 mm. As was seen for the amplitude 27 mm case, for phase 1, as the agitator starts moving toward the right channel wall, flow escapes from the central region showing that it is influenced by the entry region. The plain wall and pin fin characteristics are the same at all wall normal distances during phase 1. The presence of pin fins speeds up the start of deceleration phase during phase 2 of the agitator motion. This was noticed for the amplitude of 27 mm case also, but in the case of higher amplitude, the start of the deceleration phase is even sooner. The base region mean velocity profile (Figure 4.7(c)), shows that in the presence of pin fins, the base region experiences significant momentum loss. That also indicates that the base region influence weakens in central region. When Figures 4.7(a) and 4.7(b) are compared, it can be seen that the central region is considerably influenced by the entry region during phases 2, 3 and 4.

When fluctuating velocity profiles are compared for the central region at an amplitude of 33 mm and a frequency of 0.665Hz in 4.9(b), it can be seen that the fluctuating velocity magnitude is higher during phase 3 when compared with that of plain wall. This could be attributed to higher velocity magnitude and stronger deceleration experienced in central region during phase 3.

4.2.3 Base Region

Figure 4.6(c) shows the variation of ensemble-averaged mean velocity for pin fin cases and plain wall cases at a frequency of 0.665 Hz and an amplitude of 27 mm. During phase 1, when the agitator starts moving toward the right channel wall, the flow direction for the plain wall is positive, showing that the fluid is escaping the channel through the

narrow tip gap region. At a wall-normal distance of 14 mm for pin fins, the same phenomenon is happening as seen in the plain wall case. However, at a wall-normal distance of 8 mm, the flow direction is positive but the velocity magnitude is lower. In the presence of pin fins, as the agitator moves toward the right wall, flow outside the pin fin array has accelerated and escapes through the tip gap region, but the flow inside the pin fin forest shows a delayed response to the agitator motion and takes time to accelerate. During phase 2, when the agitator moves from the right channel wall toward the center of the channel, flow gets drawn into the right side channel cavity over the narrow tip gap. In the absence of pin fins, the drawing in of the flow is stronger closer to the wall as can be seen by comparing the velocity profiles for wall normal distances 8 mm and 14 mm. However, in the presence of pin fins, the overall activity of drawing in of the fluid has weakened in the base region with the weakening being more prominent inside the pin fin forest. It appears that the presence of pin fins causes blockage to the flow in the base region. During phase 3, as the right side cavity continues to expand, flow is still drawn into the base region over the narrow tip gap, for plain wall case; however, in the presence of pin fins, flow is being pushed out of the base region, as indicated by the positive direction of flow. During phase 3, a significant increase in the velocity outside the pin fin array is observed in central region as discussed in section 4.2.2 and seen in Figure 4.6(b). It appears that, due to the presence of pin fins, the base region has significant blockage and flow characteristics start behaving as if there were only one open end of channel near the entry region. Thus, the vortical activity in the base region reduces and flow direction in the base region starts resembling what would be expected with the tip gap blocked.

Figure 4.8(c) shows fluctuating velocity characteristics for the base region for a case with a frequency of 0.665 Hz and an amplitude of 27 mm. During phase 1, the fluctuation velocity magnitude is higher for the pin fin case, with the location inside the pin fin array showing higher fluctuation levels than the location outside the pin fin array. As the agitator just starts moving toward the right channel wall, the mean flow outside the pin fin array is set into motion but the flow inside the pin fin array shows lower mean velocities and higher turbulence levels. Thereafter, for all other phases, it can be noted that the fluctuation velocity magnitude in the presence of pin fins is lower than in the absence of pin fins. This could be attributed to the blockage provided by the pin fins in the base region and the significantly reduced mean velocities due to the presence of pin fins during phases 2, 3 and 4.

Figure 4.7(c) shows the ensemble-averaged mean velocity variation for the base region for the case with a frequency of 0.665 Hz and an amplitude of 33 mm. During phase 1, when the agitator starts moving toward the right channel wall, flow characteristics are similar to those of the plain wall. The flow inside the pin fin array also shows quick acceleration and deceleration, thus following the core flow. This was not observed for the lower amplitude case, as seen in Figure in 4.6 (c). This could be attributed to the higher amplitude which makes the agitator come all the way to the pin fins thus affecting the flow inside the pin fin array more severely. During phase 2, flow is drawn in the right side channel cavity through the tip gap region. This drawing in of the flow shows rapid fluctuations in the higher amplitude case. However, during phases 3 and 4, the flow in the base region has low velocities compared to those for the pin fin case. For the plain wall case, flow direction is negative whereas for the pin fin case, flow direction is positive.

Had the pin fin not been there, flow in the base region would have had a negative direction showing the flow was being drawn into the channel cavity from the base region. However, due to the presence of the pin fins, this drawing in of the flow in the base region has been reduced. In fact, the flow direction is positive showing that the flow is being more influenced by the flow being drawn from the entry region. This, again, could be due the blockage provided by the pin fins. As the channel cavity is expanding during phase 3, the core flow has an opportunity to escape the pin fin area on the base region and go over it. This blockage in the base region is more severe for the higher-amplitude case.

Figure 4.9(c) shows the comparison of fluctuating velocity for the base region in the presence of pin fins for the higher-amplitude case. It can be seen that pin fins show higher fluctuating velocity levels only during phase 1 when the agitator pushes the flow into the pin fin array. In all other phases, the fluctuating velocity is close to the plain wall case; in fact, slightly lower than in the plain wall case.

From the above discussion, it appears that the agitator is effective in the base region case only during phase 1, when the agitator comes close to the channel wall and pushes the flow all the way into the pin fin forest. For all other phases, when the agitator is going away from the right wall so that the right side channel cavity is wider, the flow in the base region has a tendency to avoid the near-wall zone due to the blockage provided by the pin fins. It appears that the flow stagnates near the pin fin area and is more active away from the pin fins. Also, in the case of the plain wall, the narrow tip gap is significantly affecting the flow dynamics in the base region and the central region. However, due to the presence of pin fins, the flow behavior starts resembling more of a channel flow if it would have just one end open near the entry region.

As was discussed in section 4.1 and observed in Figure 4.5(c), when the heat transfer coefficient is calculated based on the wetted area in the base region, a drop is observed when compared to the plain wall case. This could be attributed to the momentum loss experienced in the presence of pin fins as has been discussed in this section.

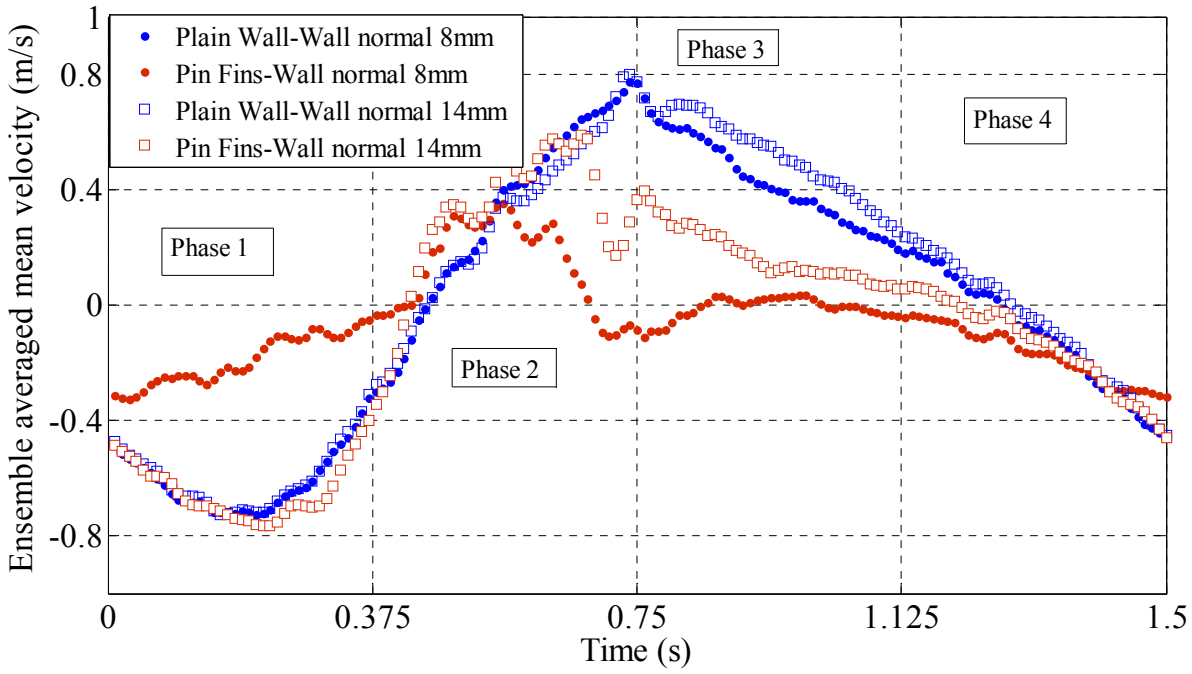

4.6(a) Entry Region

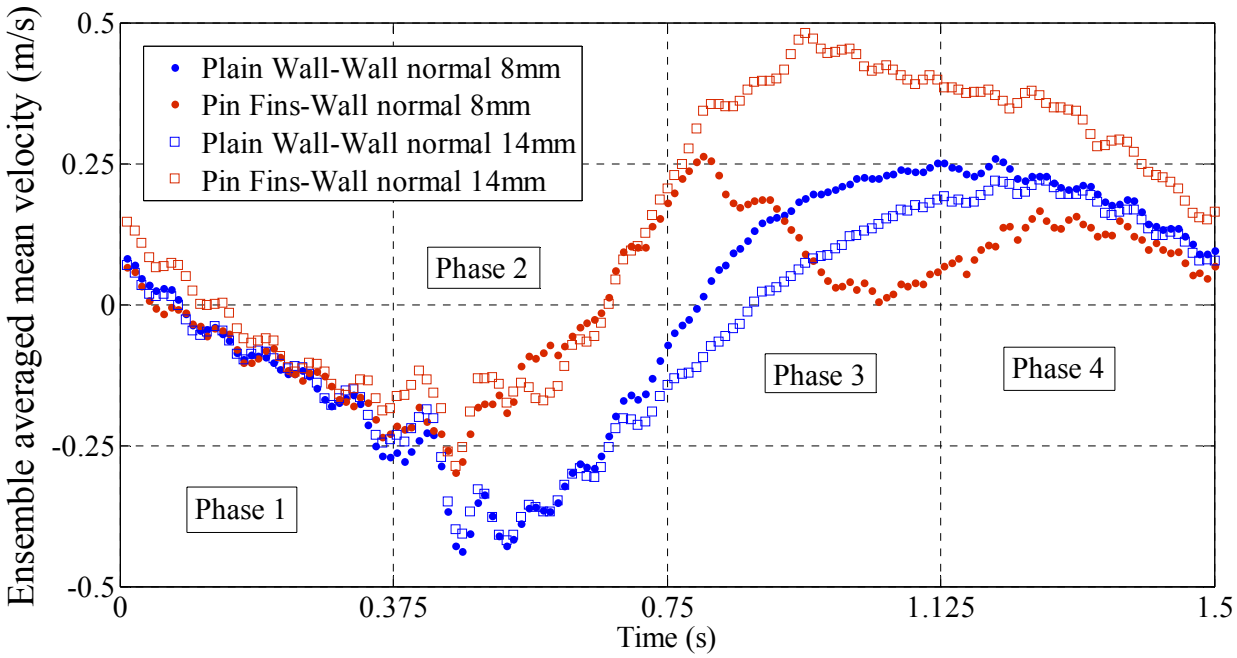

4.6(b) Central Region

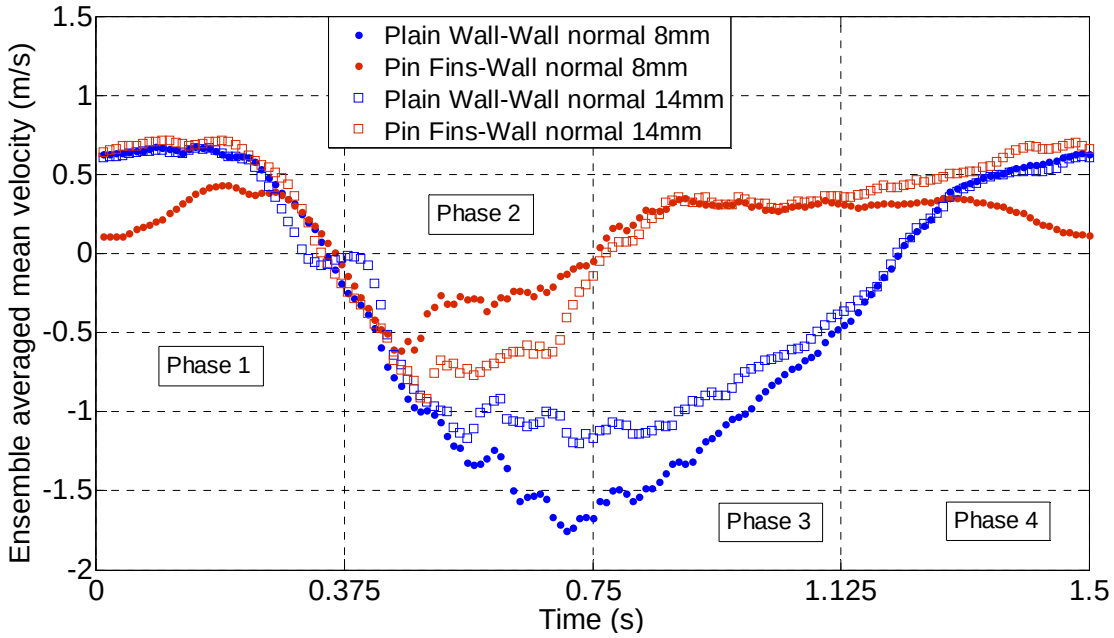

4.6(c) Base Region

Figure 4.6: Ensemble averaged mean velocity comparison for plain wall vs. pin fins at a frequency of 0.665 Hz and an amplitude of 27 mm

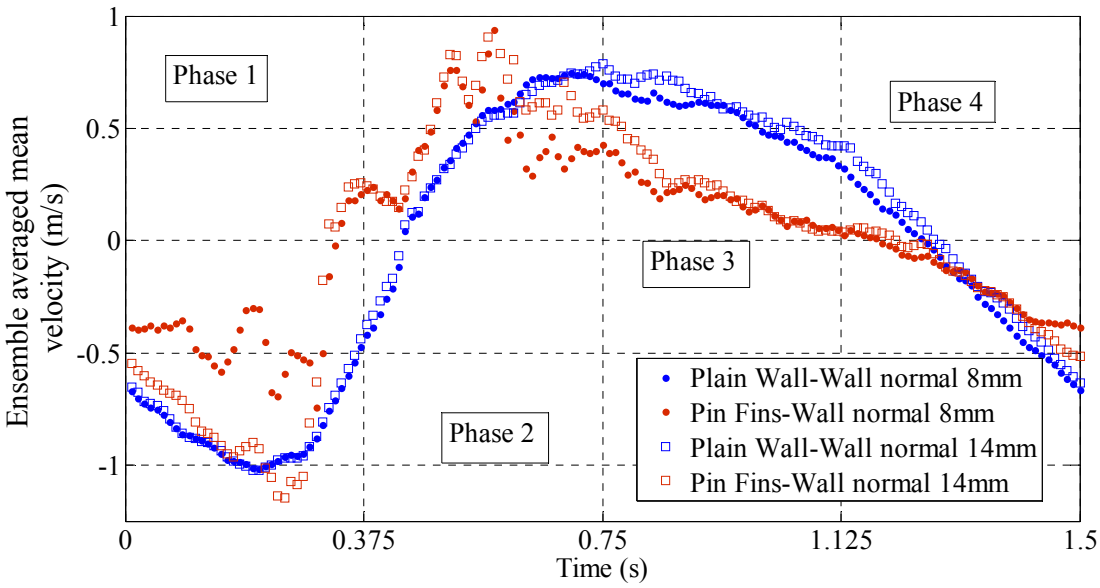

4.7(a) Entry Region

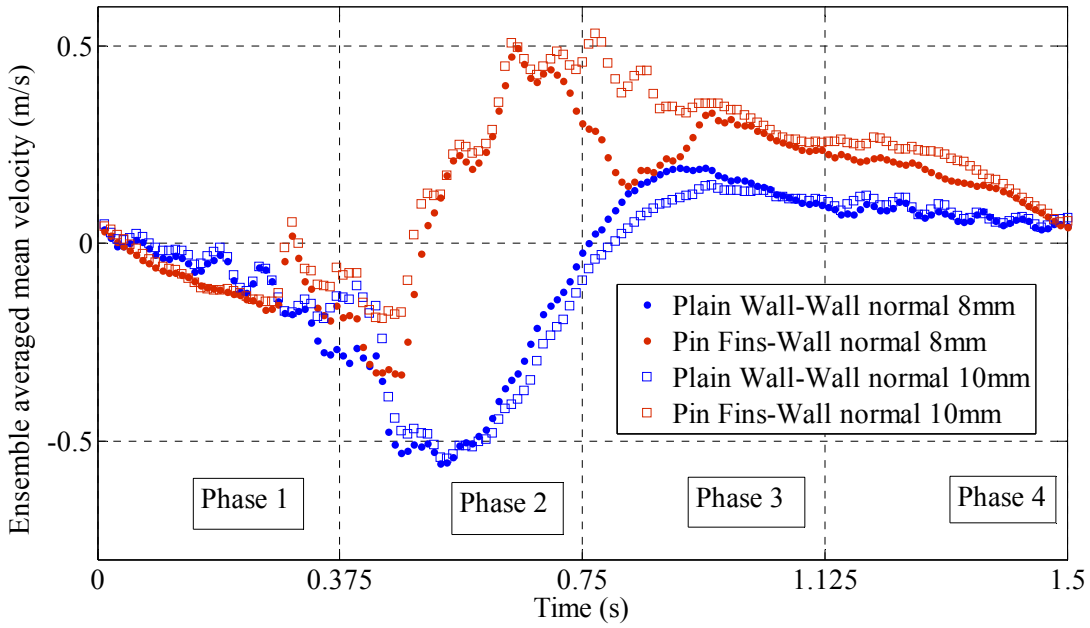

4.7(b) Central Region

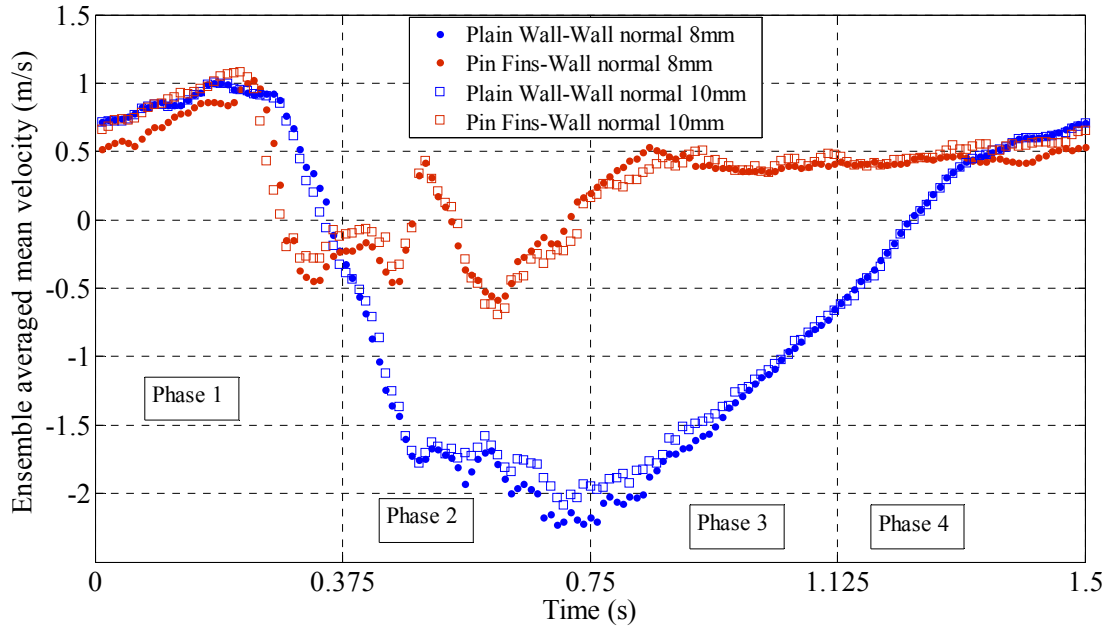

4.7(c) Base Region

Figure 4.7: Ensemble averaged mean velocity comparison for plain wall vs. pin fins at a frequency of 0.665 Hz and an amplitude of 33 mm

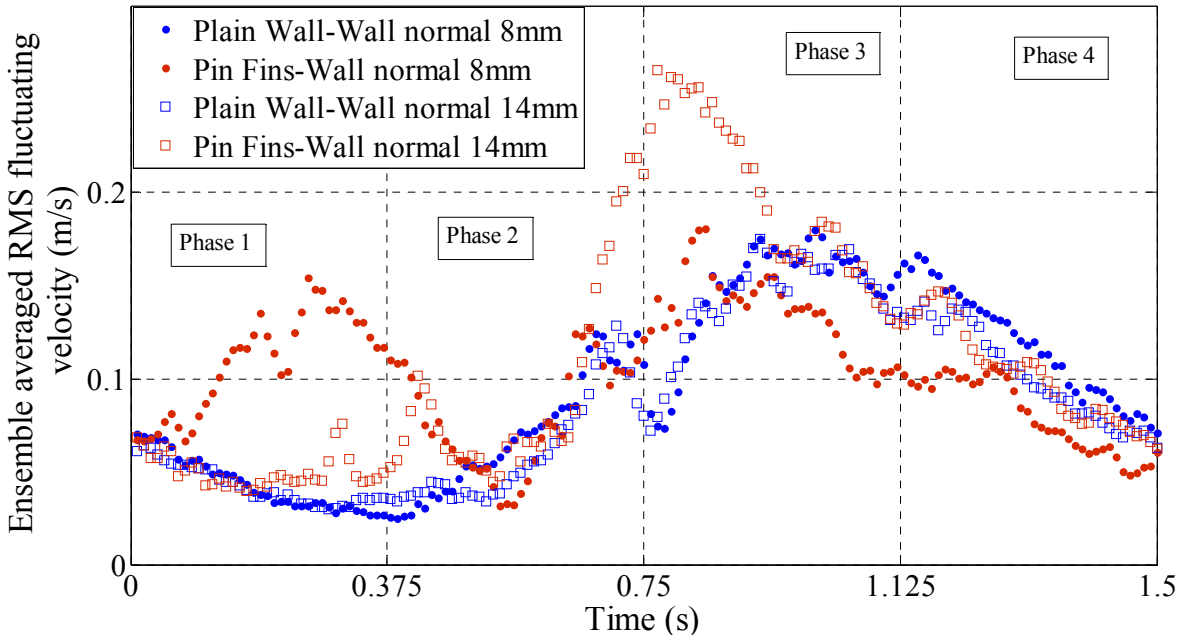

4.8(a) Entry Region

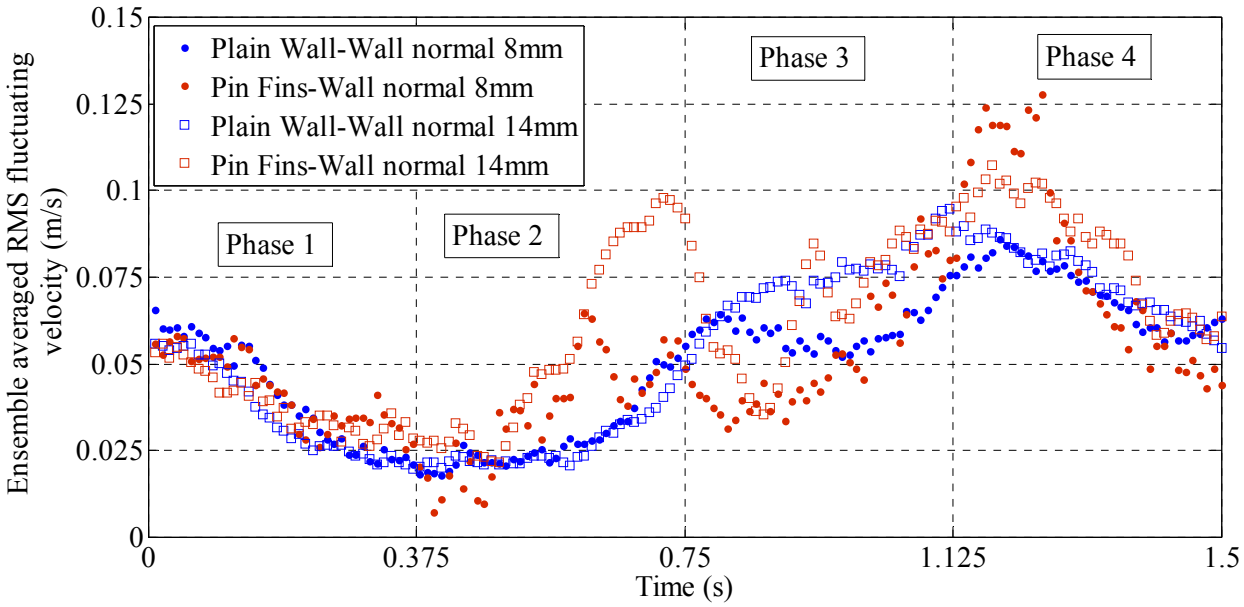

4.8(b) Central region

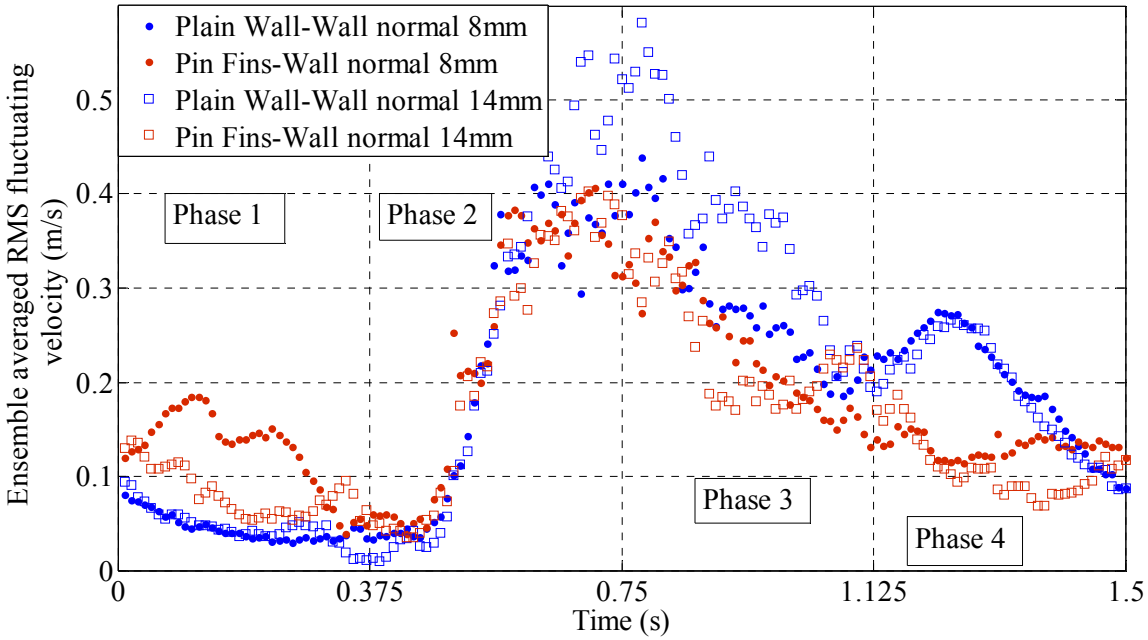

4.8(c) Base Region

Figure 4.8: Ensemble averaged RMS fluctuating velocity comparison for plain wall vs. pin fins at a frequency of 0.665 Hz and an amplitude of 27 mm

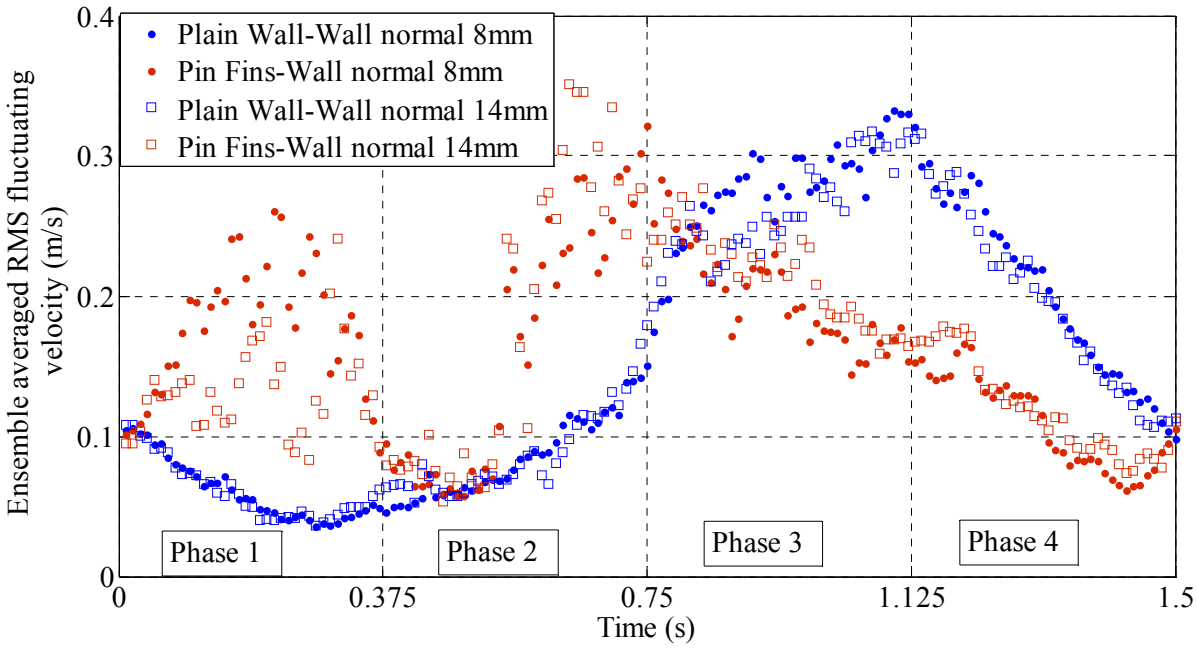

4.9(a) Entry Region

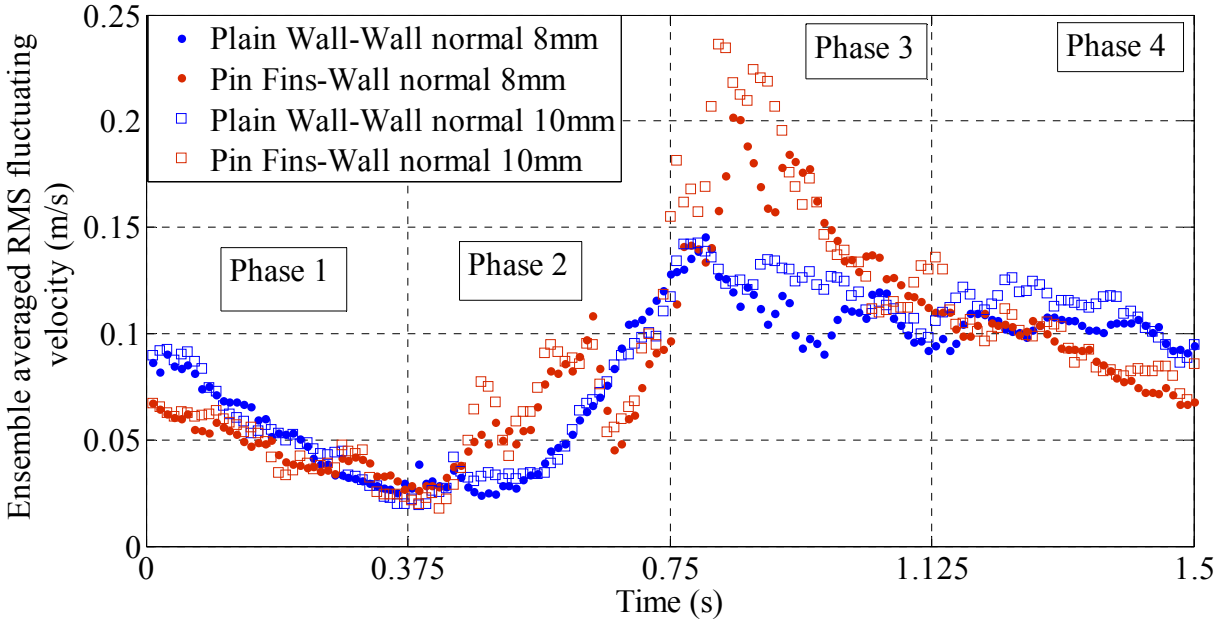

4.9(b) Central Region

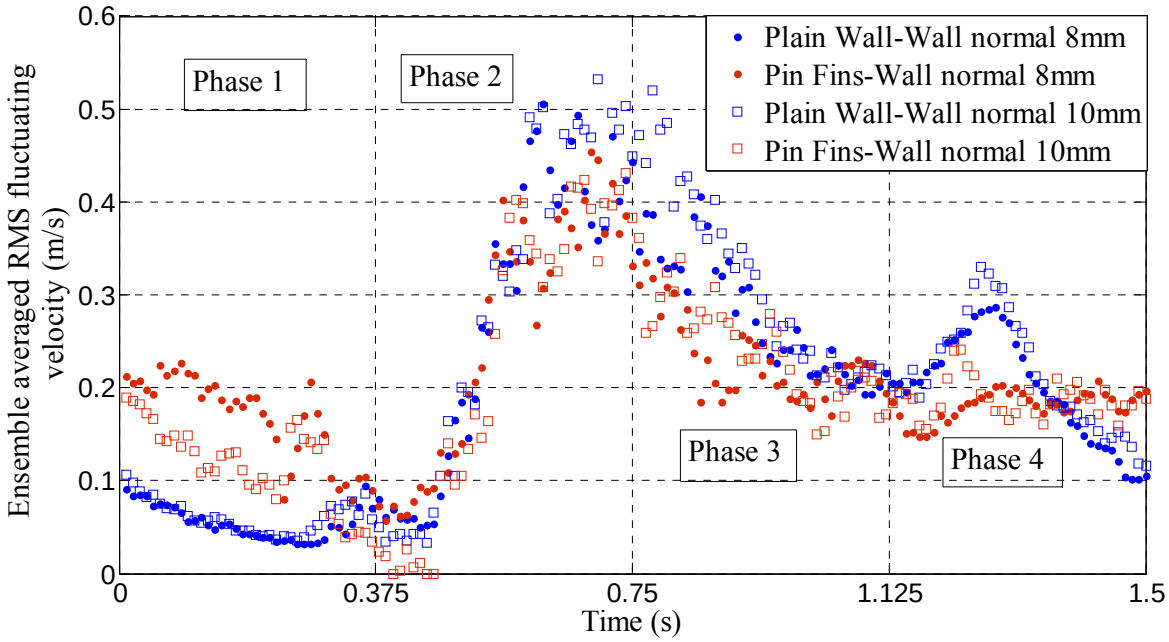

4.9(c) Base Region

Figure 4.9: Ensemble averaged RMS fluctuating velocity comparison for plain wall vs. pin fins at a frequency of 0.665 Hz and an amplitude of 33 mm

4.3 Frequency Study of cases with Pin Fins

4.3.1 Heat Transfer Coefficient Measurements

Heat transfer coefficient and velocity measurements were made at three different frequencies to study the effect of frequency on convective heat transfer in the presence of pin fins. Figure 4.10 shows the variation of heat transfer coefficient for entry region, central region and base region for three different frequencies. As can be seen from Figure 4.10, the heat transfer coefficient is highest in base region followed by the entry region and central region respectively. The heat transfer coefficient increases with increasing frequency as expected.

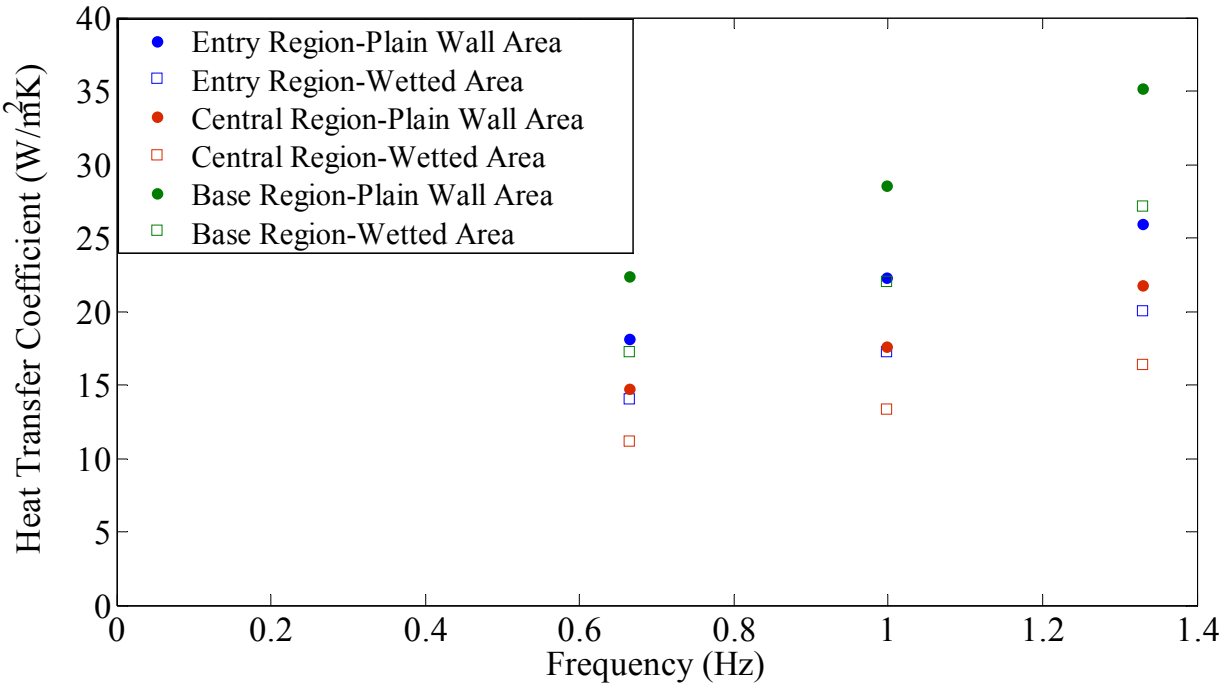

Figure 4.10: Heat transfer coefficient variation with frequency with pin fins

4.3.2 Entry Region Velocities

Figures 4.11(a) and 4.11(b) show the variation of ensemble averaged mean velocity for the entry region at two wall-normal distances of 8 mm and 14 mm. As can be seen, a change in frequency does not lead to a change in flow characteristics, it simply leads to a scaling of the velocities, even in the presence of pin fins. From Figure 4.11(a), it can be seen that during phase 3, the flow in the entry region has stagnated for almost all the three frequencies. During phase 3, the agitator is moving from the mean position toward the left wall and flow is being drawn into the entry region. From Figure 4.11(b), it can be seen that the flow outside the pin fin array is decelerating and the velocities are low. During this phase, when the velocities are low in the core flow, the entry region experiences very low velocities inside the pin fin array. Figure 4.12 shows the variation of ensemble-averaged RMS fluctuating velocity for the entry region with different

frequencies. The trends in all the phases are very consistent and change little with frequency, showing that a change in frequency affects turbulence production or decay only in terms of magnitude where turbulence production and decay scale with changes in frequency. Phase 1 has a higher turbulence inside the pin fin array than outside the pin fin array. If the mean velocity profiles are compared during phase 1, it can be seen that the flow inside the pin fin array goes through a more rapid deceleration phase than the flow outside the pin fin array, where flow first accelerates and then decelerates. The rapid deceleration inside the pin fin array during phase 1 leads to enhanced turbulence production.

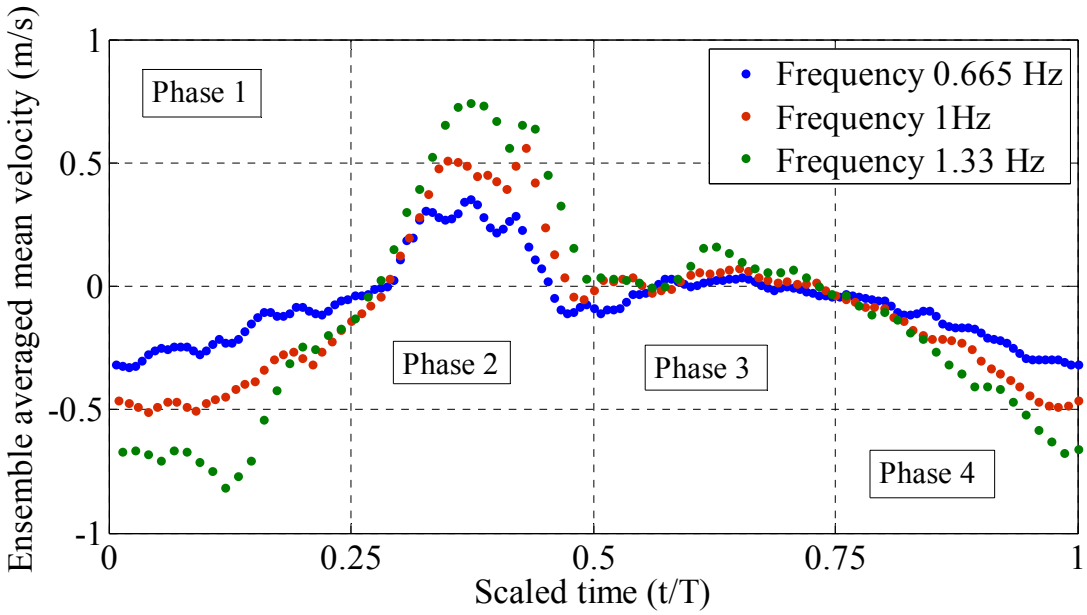

4.11(a) Wall normal distance 8 mm

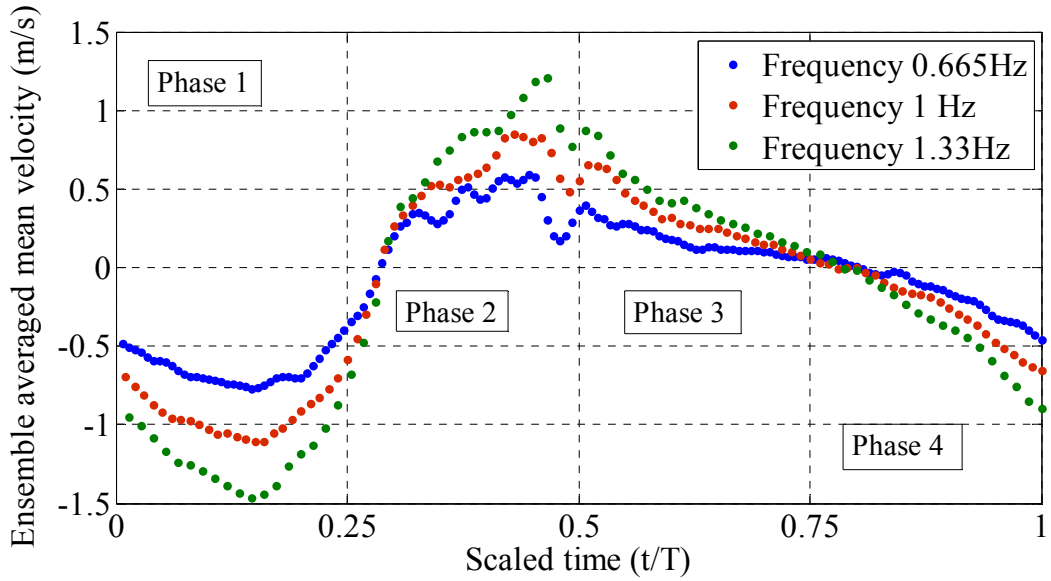

4.11(b) Wall normal distance 14 mm

Figure 4.11: Ensemble averaged mean velocity variation for entry region at different frequencies and amplitude 27 mm

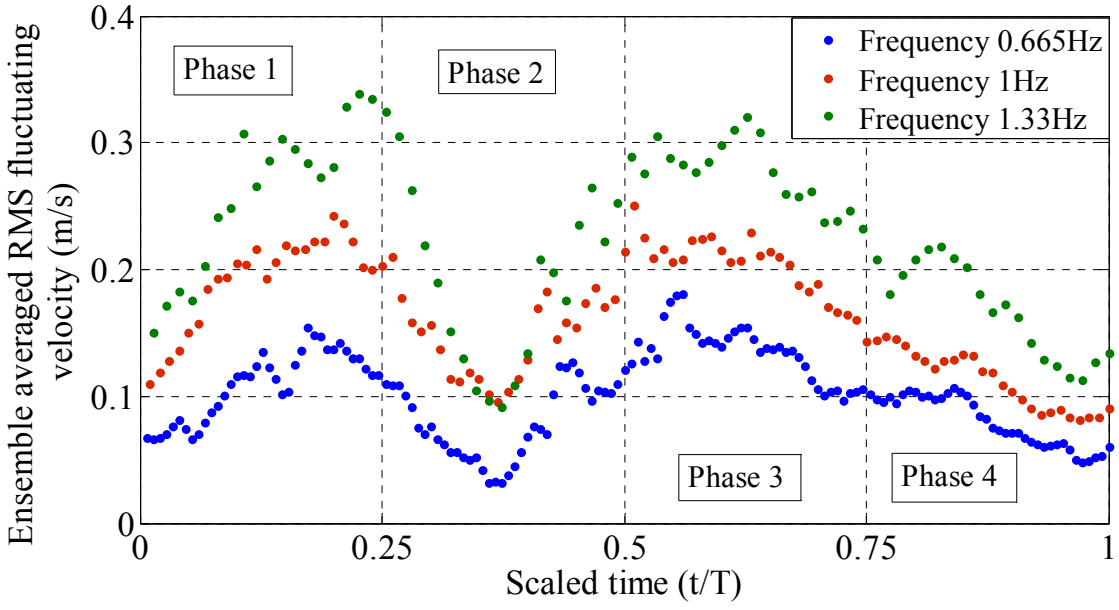

4.12(a) Wall normal distance 8 mm

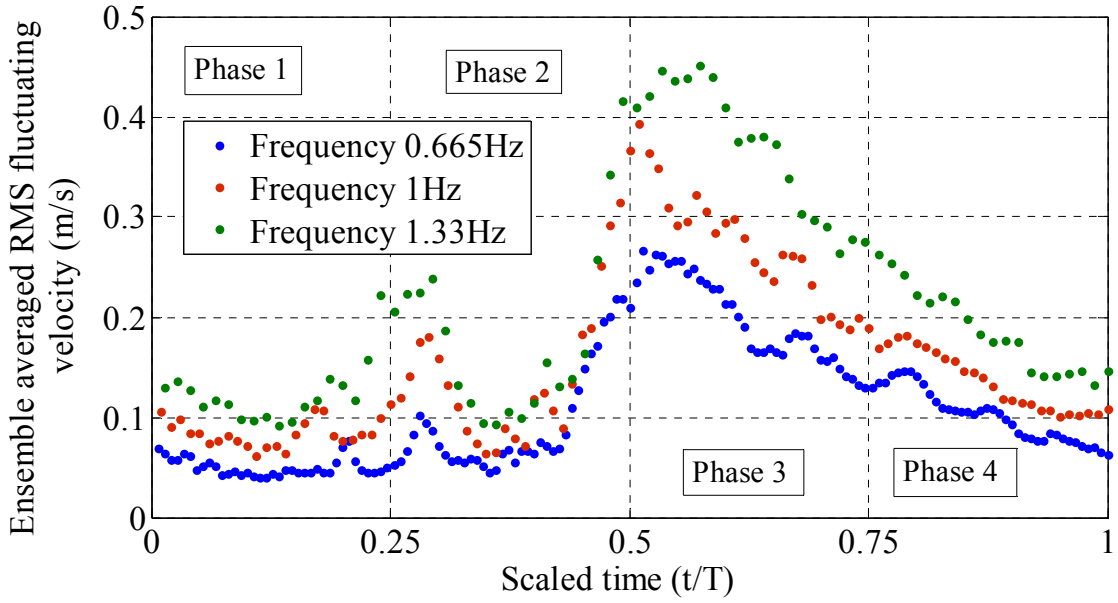

4.12(b) Wall normal distance 14 mm

Figure 4.12: Ensemble averaged RMS fluctuating velocity variation for entry region at different frequencies and amplitude 27 mm

4.3.3 Central Region Velocities

The variation of ensemble averaged mean velocity at different frequencies for the central region can be seen in Figures 4.13(a) and 4.13(b). As was noted for the entry region, for most part it can be seen that the mean velocity for central region also scales with frequency without significant differences in flow characteristics in any of the phases. The variation of ensemble averaged RMS fluctuating velocity for the central region can be seen in Figures 4.14(a) and 4.14(b). For turbulence production and decay too, as indicated by Figure 4.14, frequency leads to a scaling without changes in trends during agitator motion phases.

4.3.4 Base Region Velocities

The variation of ensemble-averaged mean velocity with frequency at two different wall-normal distances can be seen in Figures 4.15(a) and 4.15(b). The ensemble-averaged

mean velocity for the base region scales with the change in frequency. For most of the phases, the trends in the velocity remain the same, irrespective of frequency. The variation of ensemble-averaged RMS fluctuating velocity can be seen in Figures 4.16(a) and 4.16(b). At a wall normal distance of 8mm, which is inside the pin fin array, it can be seen that the ensemble averaged RMS fluctuating velocities scale with frequency for all the phases whereas at a wall normal distance of 14mm, it can be seen that during phase 1, the level of velocity fluctuation is the same, irrespective of the frequency level.

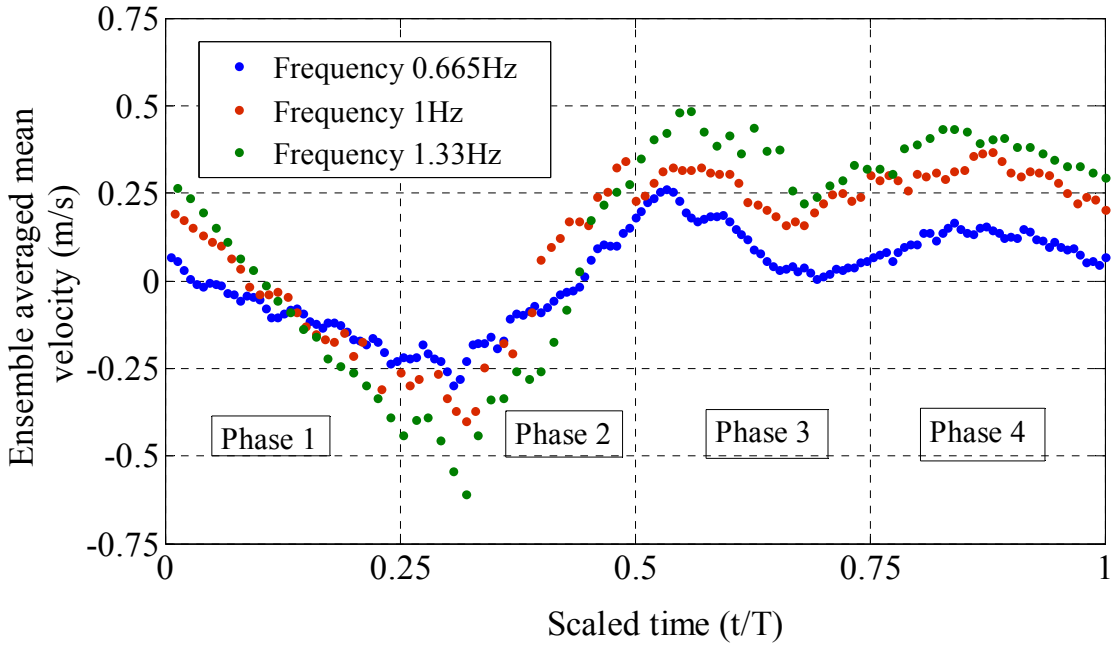

4.13(a) Wall normal distance 8 mm

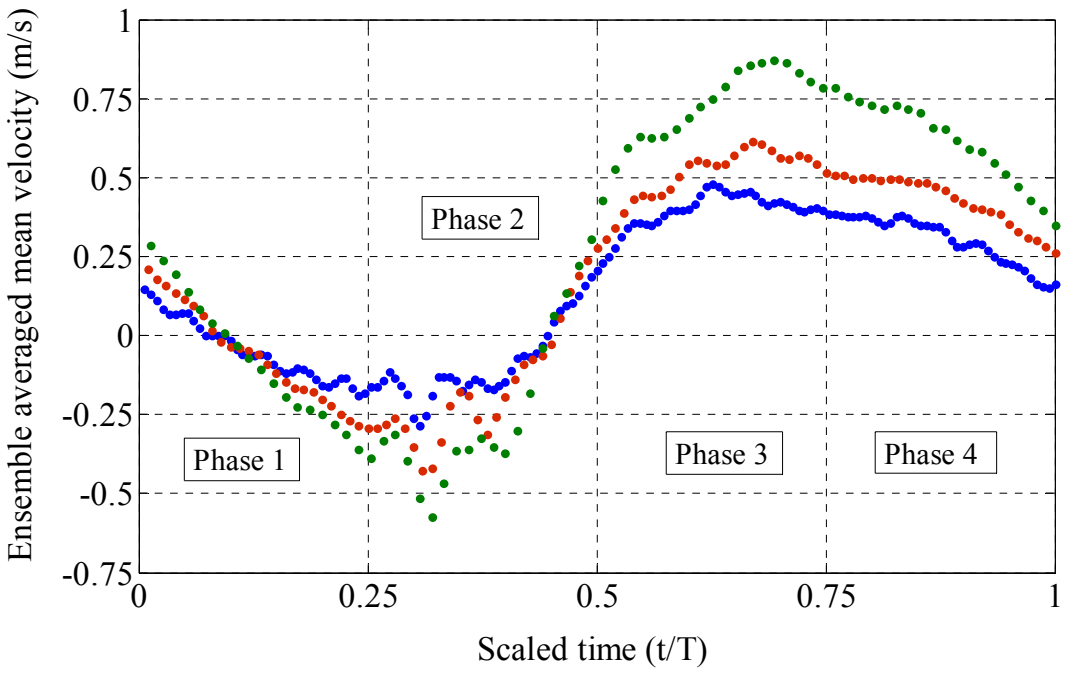

4.13(b) Wall normal distance 14 mm

Figure 4.13: Ensemble averaged mean velocity variation for central region at different frequencies and amplitude 27 mm

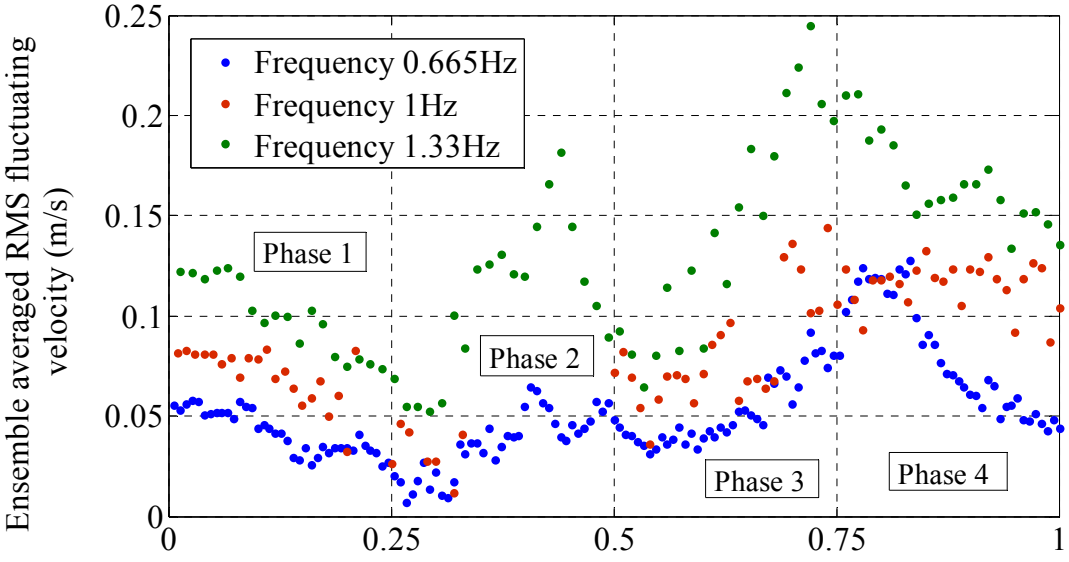

4.14(a) Wall normal distance 8 mm

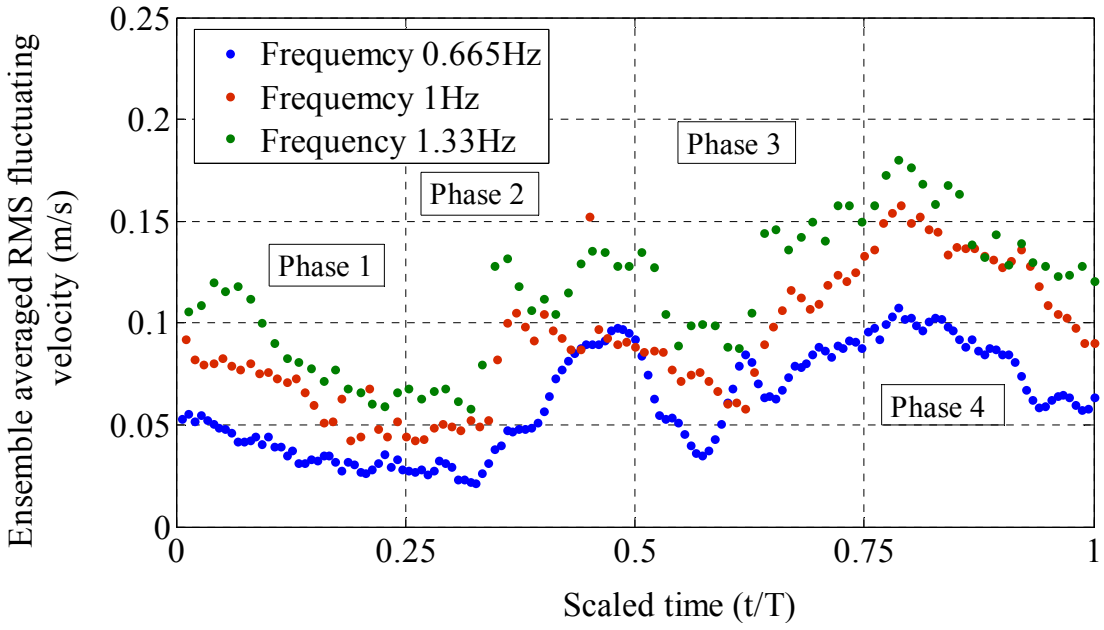

4.14(b) Wall normal distance 14 mm

Figure 4.14: Ensemble averaged RMS fluctuating velocity variation for central region at different frequencies and amplitude 27 mm

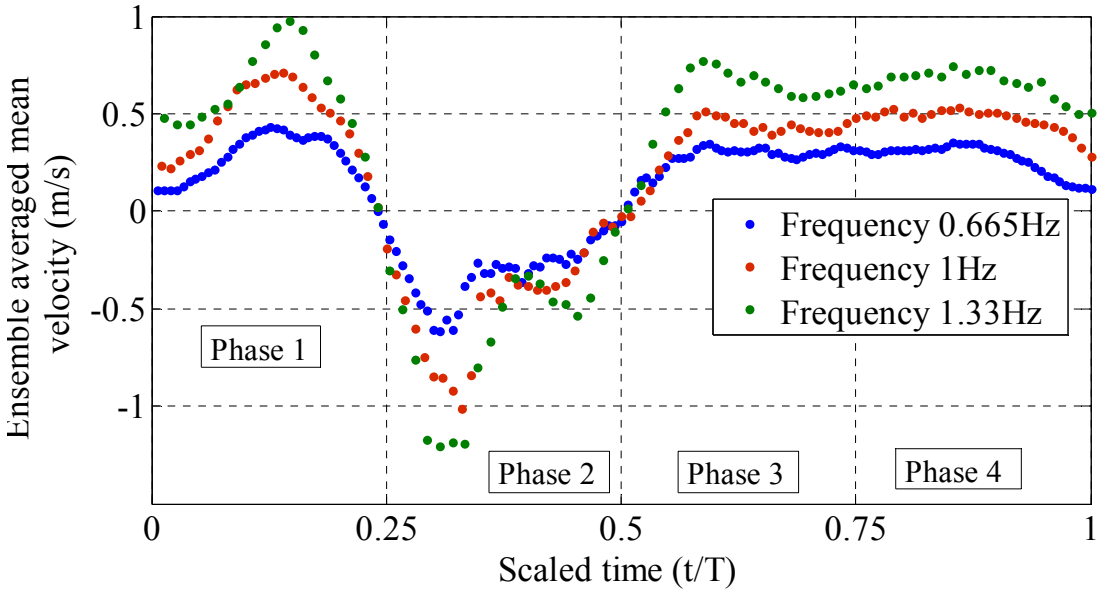

4.15(a) Wall normal distance 8 mm

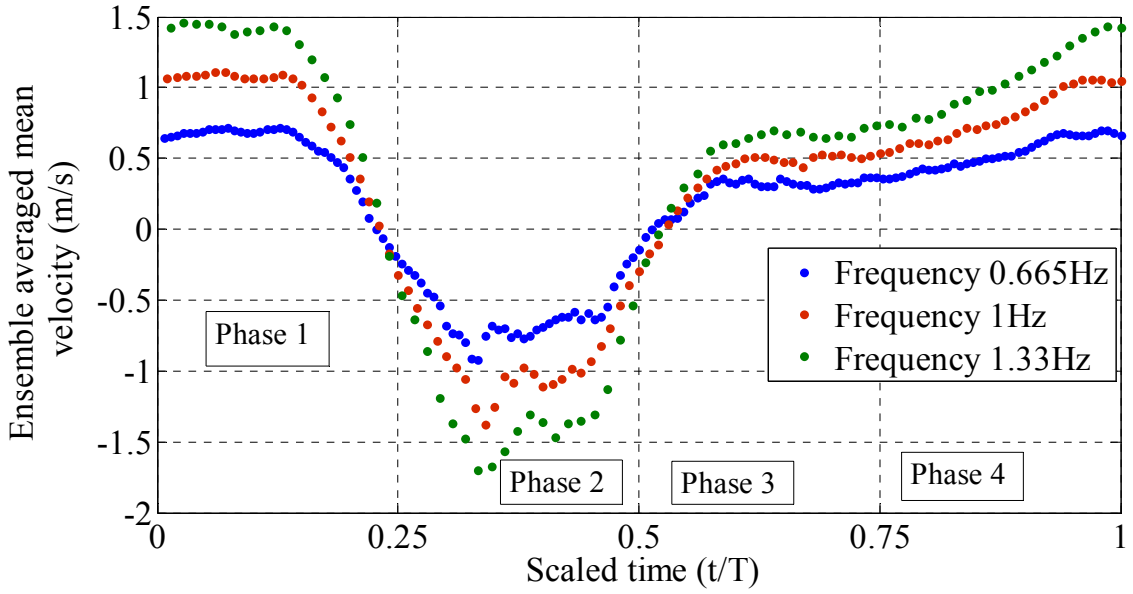

4.15(b) Wall normal distance 14 mm

Figure 4.15: Ensemble averaged mean velocity variation for base region at different frequencies and amplitude 27 mm

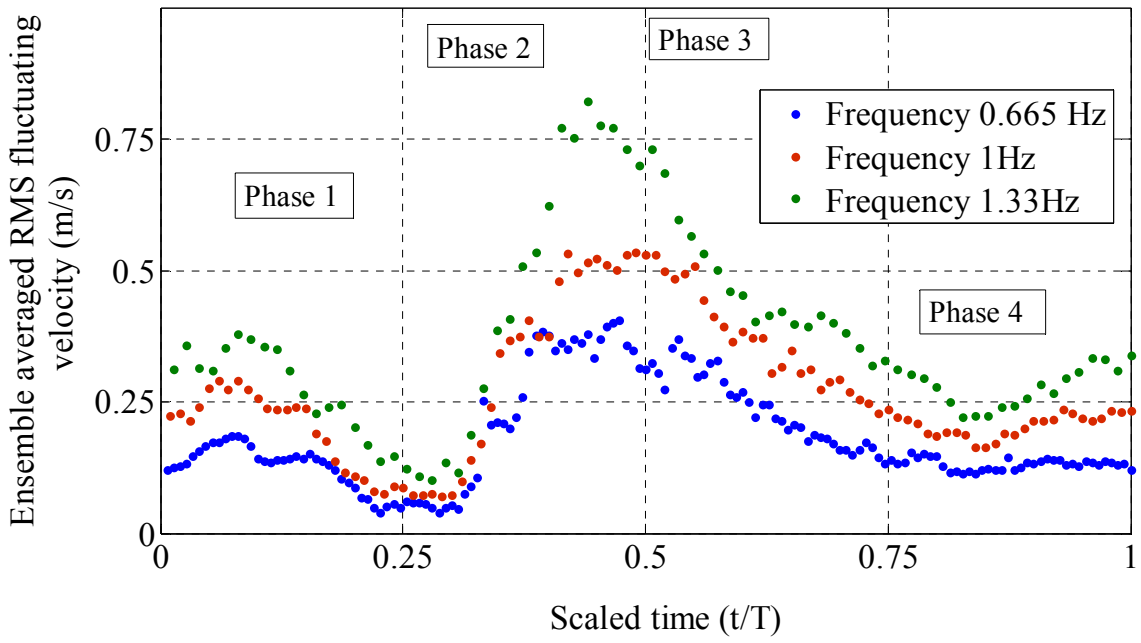

4.16(a) Wall normal distance 8 mm

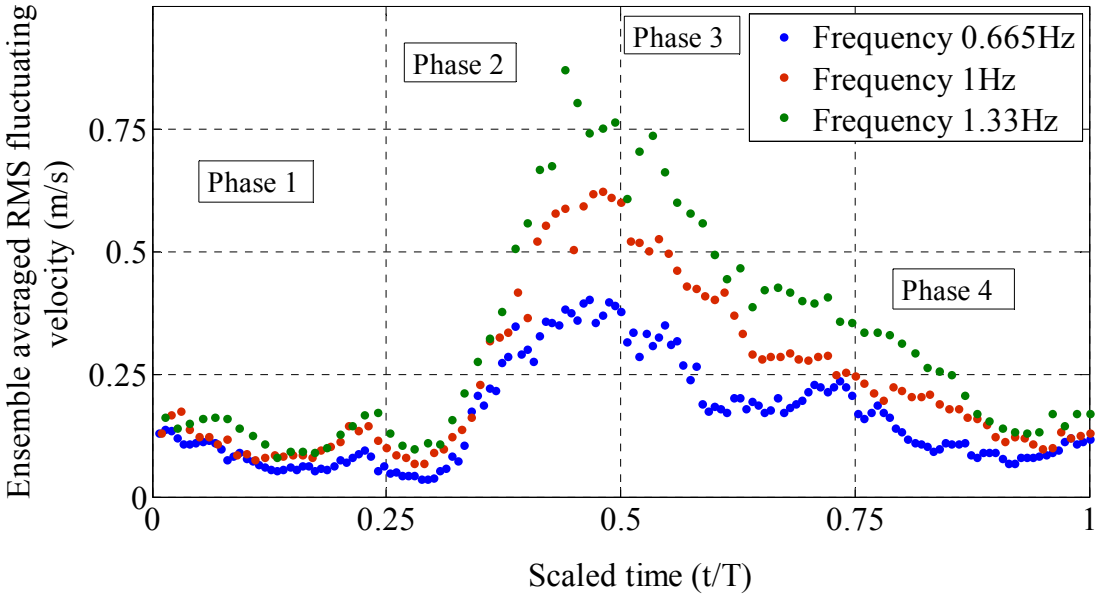

4.16(b) Wall normal distance 14 mm

Figure 4.16: Ensemble averaged RMS fluctuating velocity variation for base region at different frequencies and amplitude 27 mm

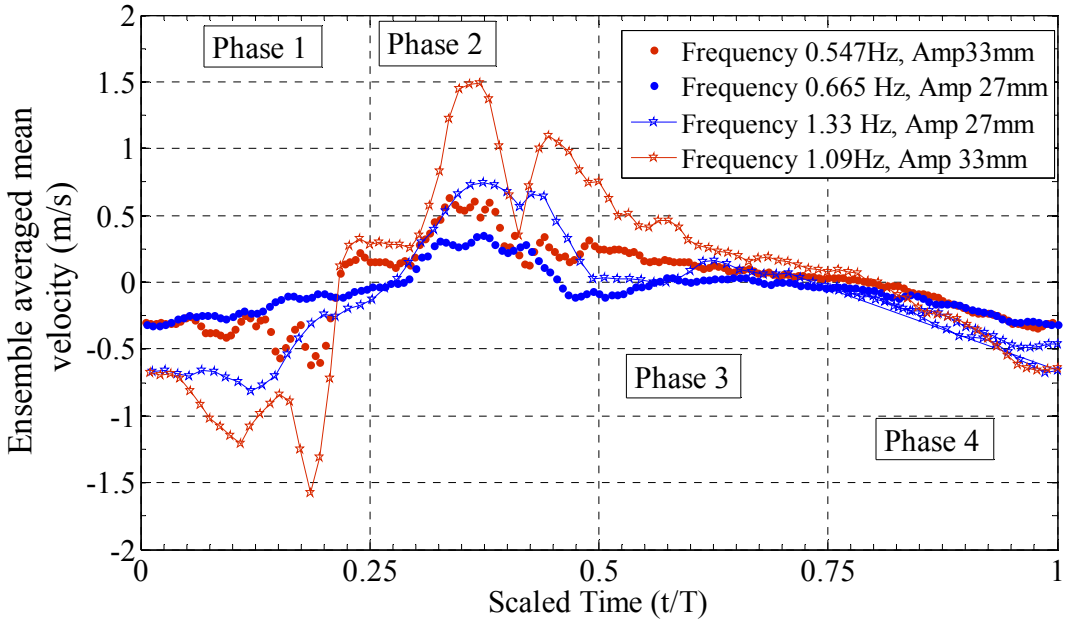

4.17(a) Entry Region

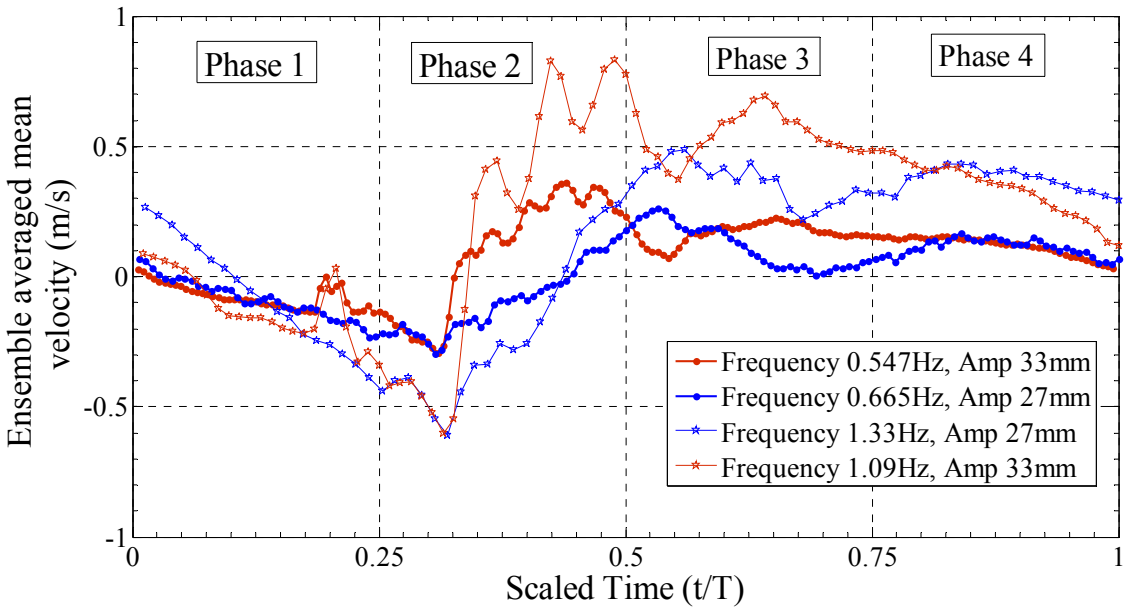

4.17(b) Central Region

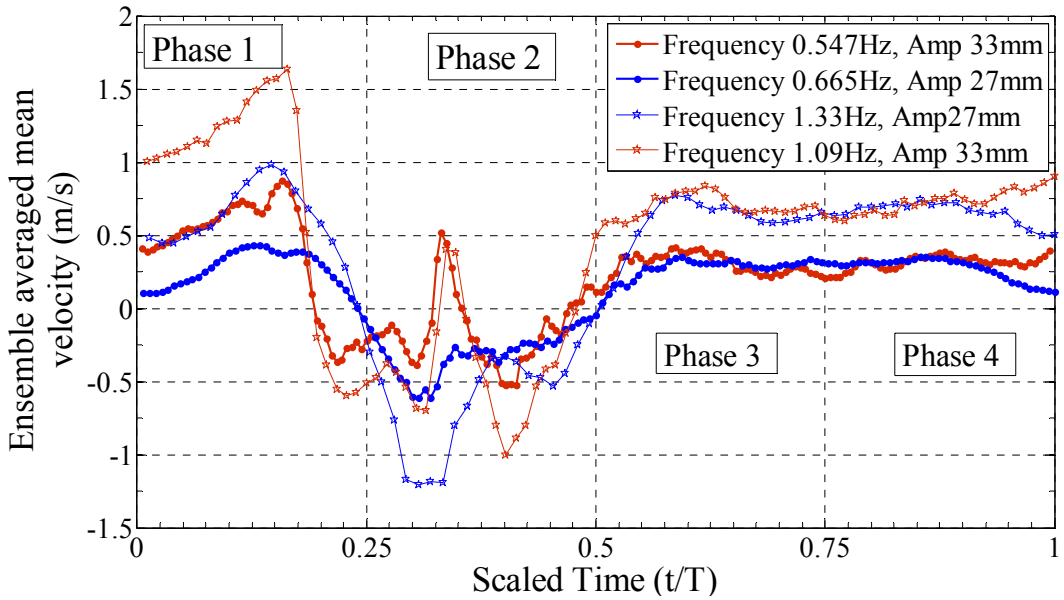

4.17(c) Base Region

Figure 4.17: Ensemble averaged mean velocity variation at fixed agitation velocities at wall normal distance 8 mm

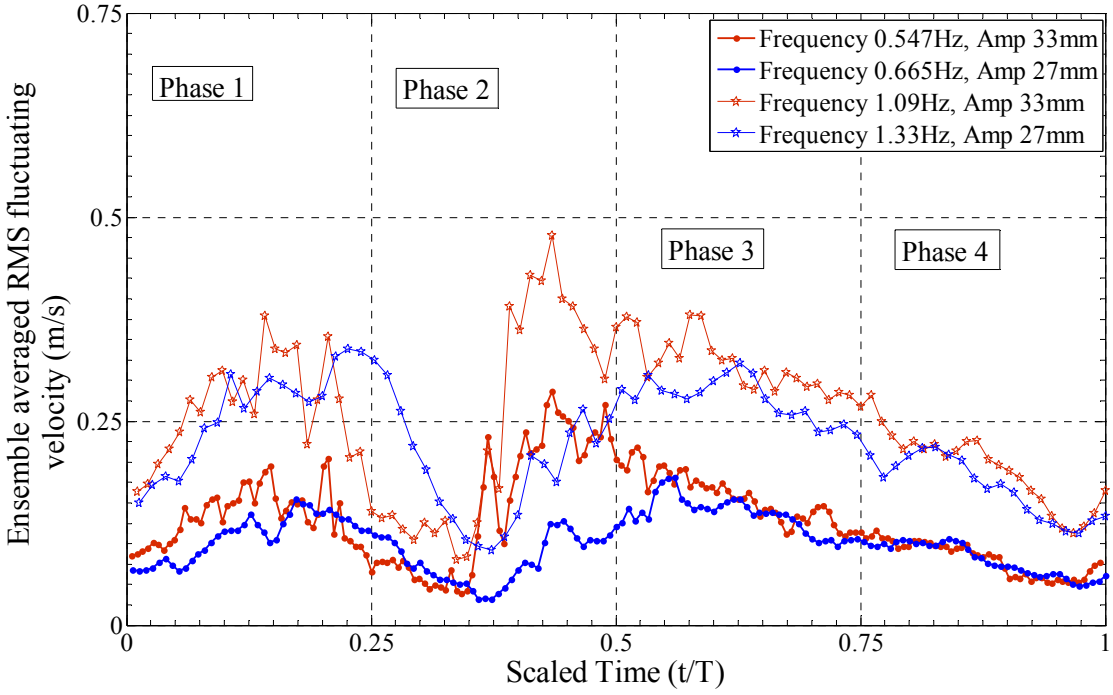

4.18(a) Entry Region

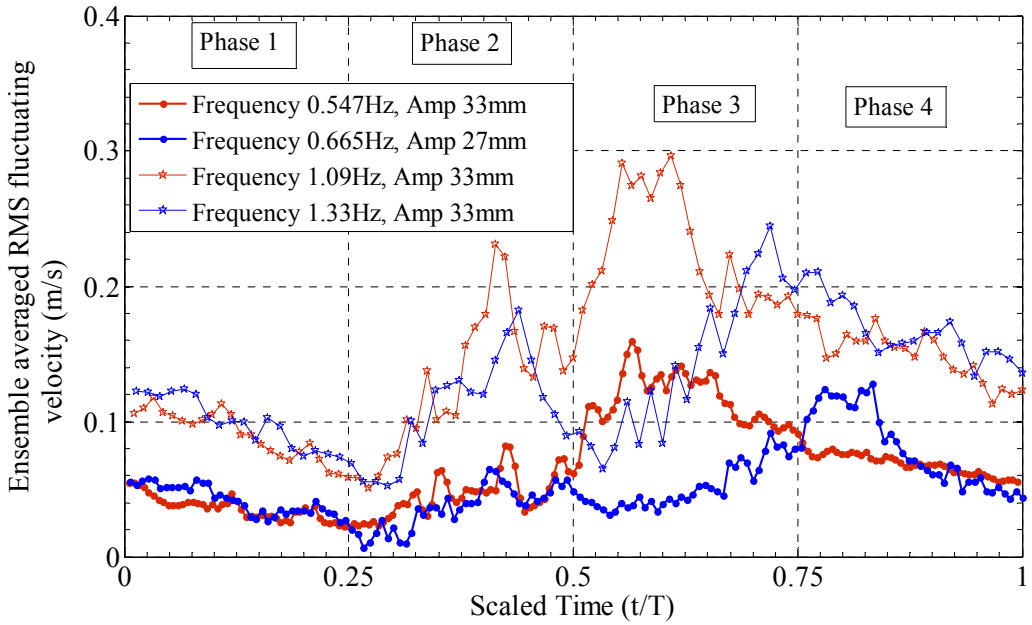

4.18(b) Central Region

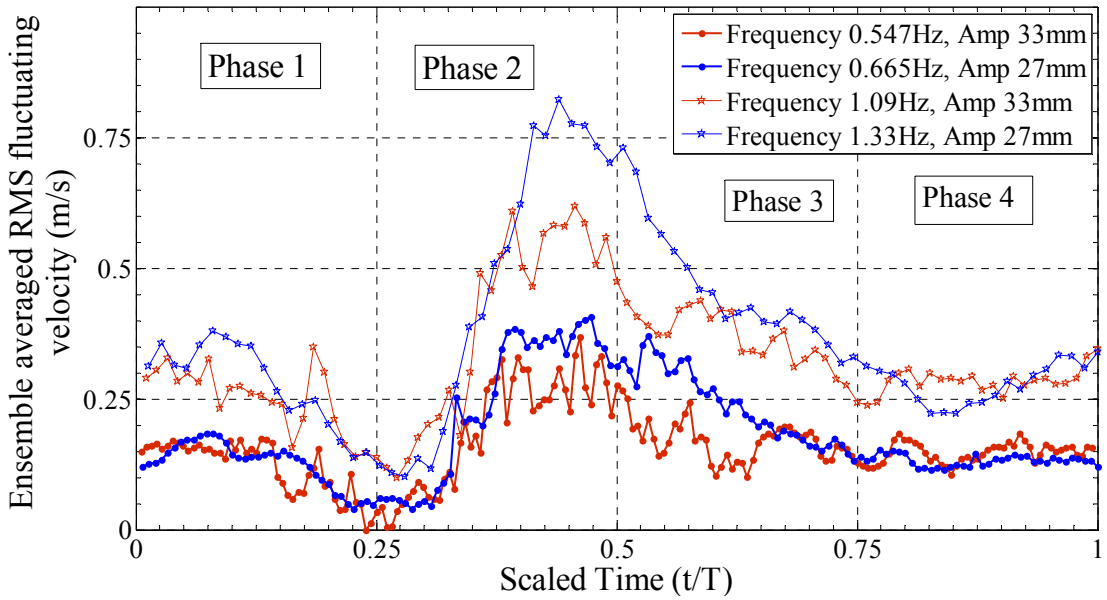

4.18(c) Base region

Figure 4.18: Ensemble averaged RMS fluctuating velocity variation at fixed agitation velocities at wall normal distance 8 mm

4.4 Agitation Velocity Study with the Pin Fin Surface

In the presence of pin fins, a heat transfer and velocity study was done to study the affect of agitation velocity by maintaining the product of amplitude and frequency constant. Figure 4.5 shows the variation of heat transfer coefficient for the entry region, central region and base region with the peak agitator velocity. The heat transfer coefficient was calculated based both on flat projected area and total wetted area. As was also noted in section 4.1, the heat transfer coefficient seems to be primarily governed by the agitation velocity, irrespective of the value of amplitude or frequency.

Figures 4.17(a), (b) and (c) show the variations of ensemble-averaged mean velocity at fixed agitation velocities for the entry region, central region and base region, respectively. As can be seen from Figure 4.17(a), for entry region and with a fixed

agitation velocity, amplitude of oscillation leads to higher velocities and higher variations in the mean velocity. Thus, inside the pin fin array, amplitude is more effective in creating flow disturbances and mixing. From Figure 4.17(a), it can be seen that higher velocities and fluctuations due to higher amplitudes of oscillation can be noted in phases 1 and 2. These are the phases during which the agitator is closer to the instrumented wall. During the latter half of phase 3 and all of phase 4, it can be seen that agitation velocity is the governing factor. This is so because the ensemble-averaged mean velocity plots for both the amplitudes overlap well during these phases. Figure 4.18(a) shows the variation of ensemble-averaged RMS fluctuating velocity for the entry region. During phases 1 and 2, the higher-amplitude case shows higher fluctuation velocities, whereas during phases 3 and 4, the fluctuation velocities for a particular agitation velocity are close to one another in value, irrespective of the value of the oscillation amplitude. As can be seen from both mean velocity and ensemble-averaged RMS fluctuation velocity results, amplitude seems to be more effective in mixing the flow inside the array during the phases (phases 1 and 2) when the agitator comes close to the right wall. However, the heat transfer results from Figure 4.5 show that neither amplitude nor frequency is more important in enhancing heat transfer so long as the agitation velocity is fixed. In that case, it appears that for the case with the higher oscillation amplitude, there is blockage to the flow over the top of the pin fins. For lower amplitude case, flow has more opportunity to go over the top of the pin fins. Thus, the increased velocity inside the pin fin array is offset by a decrease in velocity over the pin fin tops for the higher amplitude case. The net result is a same value for heat transfer coefficient at a particular agitation velocity, irrespective of the value of amplitude or frequency.

Figure 4.17(b) shows the variation of ensemble averaged mean velocity with agitation velocity for the central region. As can be seen, during phases 1 and 4, the mean velocity is more or less governed by the agitation velocity. However, during phases 2 and 3, amplitude seems to be more effective in increasing mean velocity magnitudes inside the pin fin array when compared to the lower amplitude case. When the fluctuating velocity trends are compared in Figure 4.18(b), it can be seen that except for phase 3, the fluctuation velocity for the central region remains the same at a particular agitation velocity irrespective of the value of amplitude or frequency. During phase 3, higher amplitude leads to higher fluctuations.

As can be seen in Figure 4.17(c), for base region, the ensemble averaged mean velocity is higher for the higher amplitude case during phases 1 and 2 when the agitator is close to the instrumented wall. This is because with the higher amplitude, the flow gets pushed all the way into the pin fin array. During phases 3 and 4, the mean velocity is more or less the same irrespective of the value of the agitation velocity. From Figure 4.18(c), it can be seen that higher frequency leads to higher fluctuation velocity during part of phase 2, but for most other phases, agitation velocity seems to be the governing factor in deciding the magnitude of the fluctuation velocity.

Chapter 5

Modeling Heat Transfer/Velocity Data

This chapter discusses a model to correlate the measured velocity and heat transfer data for the plain wall and pin fin wall case. The agitated flow has two major mixing mechanisms:

1) Unsteady sloshing of the flow characterized by the unsteady ensemble-averaged mean velocity. Due to the agitator oscillatory motion, the mean flow changes both in magnitude and direction. Thus, there is unsteadiness due to the mean flow motion.
2) Turbulence characterized by the RMS fluctuating velocity level. Besides the unsteadiness due to the mean flow, the fluctuating velocity among elements of the ensemble at every position within the cycle is considered to be the turbulence of the flow, which further aids mixing. It is considered to be turbulence because of its random nature, displaying different velocity values for different members of the ensemble.

Different regions in the agitated channel flow have different characteristics, as was mentioned in Chapter 3. Depending on the region, either the sloshing component (ensemble averaged mean velocity) might be dominating or the turbulence component (ensemble averaged RMS fluctuating velocity) might be the main effect toward heat transfer enhancement. Studies correlating heat transfer to free stream turbulence are scarce in the literature. Most of the studies are for nominally steady flows with high levels of free stream turbulence. The following study found in the literature to correlate heat transfer data with free stream turbulence has been used in this chapter.

- Study by Maciewjeski [55,56] in which they correlate Stanton number (St') with the turbulence level (u')

$$\frac{h}{\rho C_p u'} = St' \tag{5-1}$$

We have attempted to model our heat transfer-velocity data based on the above model. The modeling in the literature has been done for nominally steady, turbulent flow data. The agitated flow domain, being oscillatory, made it difficult to identify a representative velocity and turbulence level that would be suited for the entire oscillatory cycle in correlating time-averaged heat transfer coefficient against flow unsteadiness. However, we chose representative velocities and turbulence levels we thought would be best for the model. The details of the modeling are described in the section below.

5.1 Determining the Fluctuating Velocity for Use in the Maciejewski Model

Studies on correlating free stream velocity data to heat transfer data are rather scarce. In fact, more scarce are studies where the flow is oscillatory or unsteady and also has free stream turbulence. The agitated flow falls in this domain making it a complex case for heat transfer-velocity correlations. Maciejewski et al. [55,56] were able to correlate heat transfer data with a single u' predictor. They proposed that the heat transfer coefficient could be correlated with free stream turbulence This relationship is for flows with high levels of free stream turbulence. Maciejewski et al. [55, 56] extended the relationship to flows with lower levels of free stream turbulence. They introduced a new St', defined as

$$St' = \frac{h}{\rho C_p u'_{max}} \tag{5-2}$$

where u'_{max} is the maximum standard deviation in the streamwise component of velocity in the wall-affected region, i.e. the region near the surface that exhibits "law of the wall" behavior in the mean velocity profile, irrespective of the way turbulence was generated.

Since our flow is unsteady, we attempted to find an equivalent to u' for our flow. As explained in Chapter 2, using the LDV, velocity readings were collected at different times within a cycle. Around 70 cycles were measured for one complete measurement. A time step of 0.01s was chosen for averaging. The velocity $U_{t,i}$ was obtained by averaging all measured points between time (t-0.01)s and t for cycle i. Suppose the total number of cycles is n. The ensemble averaged mean velocity for a time t from the beginning of each cycle is obtained as

$$U_{mean}(t) = \frac{1}{n}\sum U_{t,i} \tag{5-3}$$

The ensemble averaged RMS fluctuating velocity U'_{RMS} is obtained as

$$U'_{RMS}(t) = \left(\frac{1}{n}\sum\left(U_t - U_{t,i}\right)^2\right)^{1/2} \tag{5-4}$$

The plot of $U_{mean}(t)$, the ensemble averaged mean velocity for each of the three regions at a frequency of 0.665 Hz and an amplitude (mean to peak) of 27 mm is as shown in Figure 5.1.

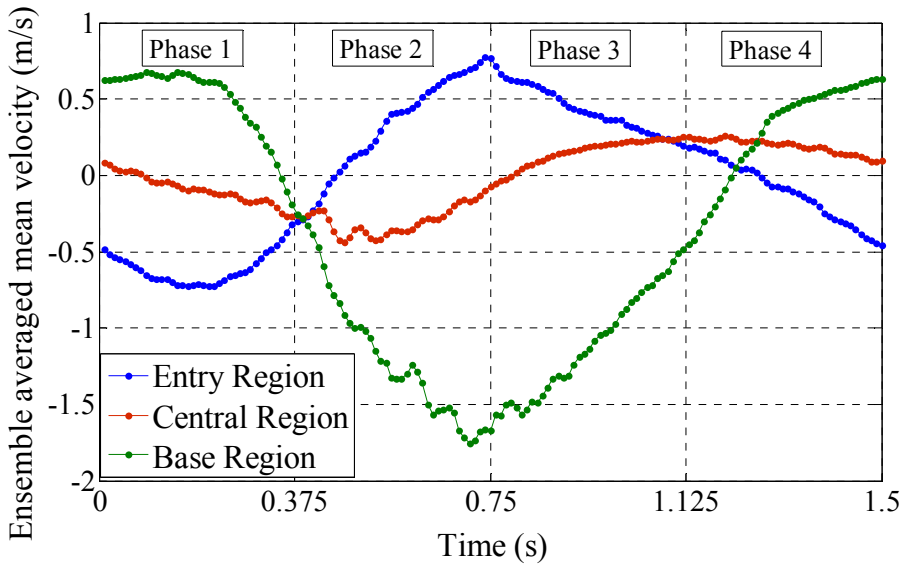

Figure 5.1: Variation of ensemble averaged mean velocity for the entry region, central region and base region at a frequency of 0.665 Hz and an amplitude of 27 mm

The plot of $U'_{RMS}(t)$ ensemble-averaged RMS fluctuating velocity for each of the three regions at a frequency of 0.665 Hz and an amplitude (mean to peak) of 27 mm is as shown in Figure 5.2.

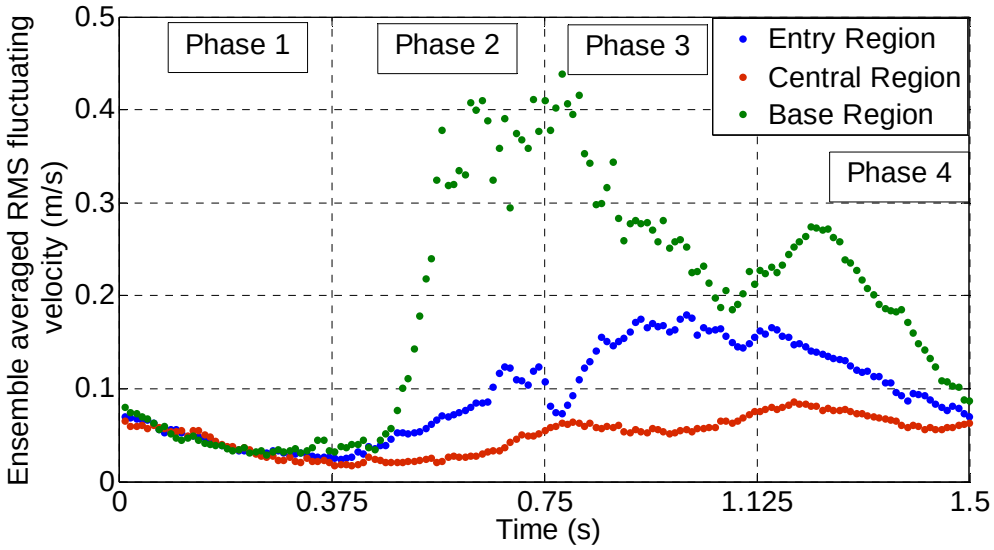

Figure 5.2: Variation of ensemble averaged RMS fluctuating velocity for entry region, central region and base region at a frequency of 0.665 Hz and an amplitude of 27 mm

The turbulence intensity at time instant t, Tu(t) is obtained as

$$Tu\ (t) = \frac{U'_{RMS}(t)}{U_{mean}(t)} \tag{5-5}$$

The variation of Tu_t is shown in Figure 5.3.

A u' predictor needs to be defined for our study. This u' predictor for our study has been defined as

$$u' = (U^2_{mean,RMS} + U'^2_{RMS,avg})^{1/2} \tag{5-6}$$

where $U_{mean,RMS}$ is the RMS variation of the mean velocity U_{mean}. The RMS variation can be calculated from Figure 5.1 and can be labeled $U_{mean,RMS}$. Similarly, $U'_{RMS,avg}$ is the average fluctuating velocity during a cycle. The average of the fluctuating velocity during a cycle from Figure 5.2 can be labelled $U'_{RMS,avg}$. Since, the mixing is caused both by the

sloshing component and the turbulent component, it was important to account for both these factors while defining u'. Similarly, characteristic turbulence intensity was defined for the unsteady flow. Since the flow is unsteady, a turbulence intensity that would be more characteristic and representative of the flow cycle was defined. The characteristic turbulence intensity for the flow cycle was defined as:

$$Tu = \frac{U'_{RMS,avg}}{U_{mean,avg}} \tag{5-7}$$

where $U_{mean,avg}$ is the average speed during a cycle.

The turbulence intensity has been listed in Table 5.1.

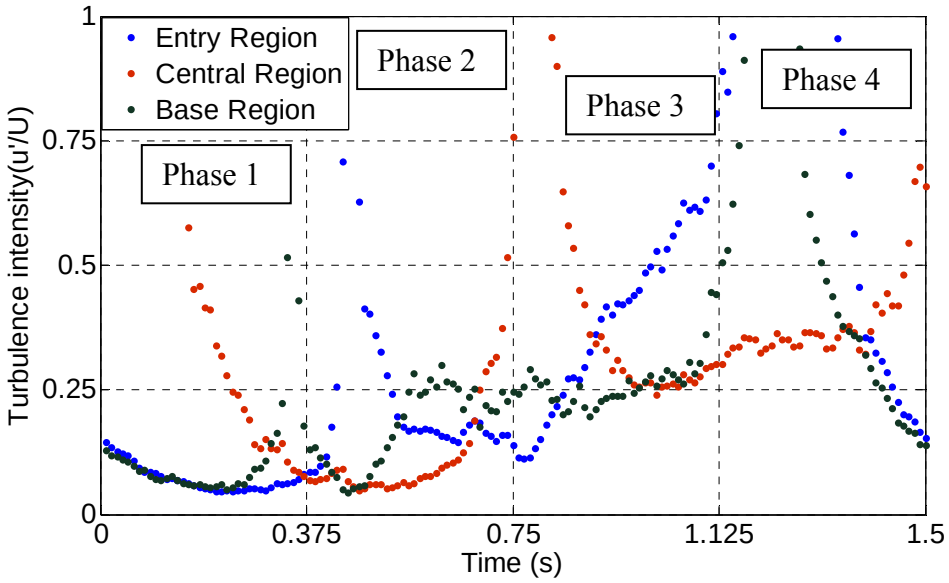

Figure 5.3: Variation of turbulence intensity for entry region, central region and base region at a frequency of 0.665 Hz and an amplitude of 27 mm

5.2 Stanton Number Modeling

A u' value was defined based on the above description. A St' value was extracted from the u' predictor described above (equation 5-6) and the velocity measurements. These data are summarized in the following table.

Table 5.1: St' value based on u' predictor, plain wall

Case	Frequency (Hz)/ Amplitude (mm)	$U_{mean,RMS}$	$U'_{RMS,avg}$	Tu	u' (m/s)	HTC (W/m^2K)	St'	% error
Entry Region	0.665 Hz / 27mm	0.459	0.0944	0.235	0.468	13.1	0.023	28
Entry Region	1 Hz / 27 mm	0.675	0.135	0.227	0.688	15.6	0.019	6
Entry Region	1.33 Hz / 27 mm	0.948	0.786	0.239	0.967	18.8	0.016	-11
Central Region	0.665 Hz /27 mm	0.213	0.050	0.267	0.219	10.4	0.039	116
Central Region	1 Hz / 27 mm	0.301	0.081	0.311	0.312	13.3	0.035	94
Central Region	1.33 Hz / 27 mm	0.748	0.127	0.357	0.758	15.8	0.017	-6
Base Region	0.665 Hz / 27 mm	0.841	0.189	0.238	0.862	18.3	0.018	0
Base Region	1 Hz / 27 mm	1.25	0.293	0.242	1.28	22.8	0.015	-16
Base Region	1.33 Hz / 27 mm	1.70	0.404	0.247	1.744	28.5	0.014	-22
Entry Region	0.547 Hz / 33 mm	0.510	0.127	0.284	0.526	13.8	0.022	22
Entry Region	0.82 Hz / 33 mm	0.73	0.180	0.277	0.752	17.2	0.019	6
Entry Region	1.1 Hz / 33 mm	0.927	0.234	0.956	0.927	18.1	0.016	-11
Central Region	0.547 Hz / 33 mm	0.202	0.062	0.367	0.212	11.5	0.045	150
Central Region	0.82 Hz / 33 mm	0.265	0.105	0.51	0.286	14.3	0.042	133
Central Region	1.1 Hz / 33 mm	0.345	0.119	0.439	0.365	16.2	0.037	105
Base Region	0.547 Hz / 33 mm	0.826	0.179	0.230	0.845	17.9	0.018	0
Base Region	0.82 Hz / 33 mm	1.39	0.253	0.190	1.41	22.9	0.013	-27
Base Region	1.1 Hz / 33 mm	1.845	0.331	0.186	1.876	26.9	0.012	-33

From Table 5.1, we can see that the average turbulence intensity for most cases is above 20%. For this range of turbulence intensities, the St' value should be around 0.018 [55,56]. The last column in Table 5.1 (% error) specifies the error with respect to St'

value of 0.018. It can be seen that the error is maximum in the central region followed by the entry region and the base region. The Maciejewski St' model performs best in the base region and the entry region followed by the central region, respectively. The mixing activity generated by turbulence is maximum in the base region followed by the entry region and central region respectively. The level of free stream turbulence u' is maximum in the base region followed by the entry region and central region respectively. That might be the explanation for the observation that the best performance of the St' model is in the base region and the entry region. As can be seen from Table 5.1, St' values in the central region are very high. Modeling of heat transfer dominated by turbulence level for steady flows is in itself very challenging. The agitated flow is more complex for it is unsteady, making modeling of the measured steady state heat transfer all the more difficult. Though, one would like to get the simplest possible correlation without taking into effect the frequency, length scale or other parameters, the flow phenomena in the agitated domain appear to be too complex to be correlated with a single predictor such as u' used in Maciejewski [55,56].

Table 5.2 shows the results of the Maciejewski model for pin fin case at a wall normal distance of 8 mm. The heat transfer coefficient has been calculated based on the wetted area. Table 5.3 shows the results of the Maciejewski model for pin fin case at wall normal distance 14 mm, for amplitude 27 mm (mean to peak). Table 5.4 shows the results of the Maciejewski model for pin fin case at wall normal distance 10 mm, for amplitude 33 mm. As can be seen from the tables, Maciejewski model does not do very well in the presence of pin fins. Identification of a representative velocity to model steady state heat transfer was not a simple task in the plain wall case. In case of pin fins, since the three

dimensionality of the flow increases, it is even more challenging to identify a velocity that is representative of the entire flow field. The point velocity measurement that we made might not be sufficient to be representative of the entire flow field in the case of pin fins and therefore does not work well in the model.

Table 5.2: St' value based on u' predictor, pin fin wall, wall normal distance 8 mm

Case	Frequency (Hz) / Amplitude (mm)	$U_{mean,RMS}$	$U'_{RMS,avg}$	Tu	u' (m/s)	HTC (W/m^2K)	St'	% error
Entry Region	0.665 Hz / 27 mm	0.167	0.101	0.251	0.195	14.0	0.060	231
Entry Region	1 Hz / 27 mm	0.288	0.163	0.675	0.331	17.2	0.043	139
Entry Region	1.33 Hz / 27 mm	0.419	0.338	0.658	0.475	20.0	0.035	94.17
Central Region	0.665 Hz / 27 mm	0.134	0.053	0.459	0.144	11.2	0.064	256
Central Region	1 Hz / 27 mm	0.210	0.085	0.377	0.227	13.3	0.049	170
Central Region	1.33 Hz / 27 mm	0.311	0.245	0.291	0.396	16.4	0.034	91
Base Region	0.665 Hz / 27 mm	0.369	0.184	0.663	0.412	17.3	0.035	93
Base Region	1 Hz / 27 mm	0.427	0.274	1.027	0.51	22.02	0.036	100
Base Region	1.33 Hz / 27 mm	0.580	0.373	0.611	0.689	27.2	0.033	81
Entry Region	0.547 Hz / 33 mm	0.078	0.130	0.559	0.152	14.02	0.077	326
Entry Region	0.82 Hz /33 mm	0.503	0.199	0.489	0.541	17.6	0.027	50
Entry Region	1.1 Hz / 33 mm	0.697	0.255	0.396	0.743	21.00	0.023	30
Central Region	0.547 Hz / 33 mm	0.151	0.068	0.450	0.166	11.2	0.056	210
Central Region	0.82 Hz / 33 mm	0.248	0.110	0.435	0.272	12.9	0.039	119
Central Region	1.1 Hz / 33 mm	0.361	0.148	0.385	0.390	16.3	0.035	92
Base Region	0.547 Hz / 33 mm	0.314	0.158	0.462	0.351	16.9	0.040	122
Base Region	0.82 Hz / 33 mm	0.909	0.199	0.374	0.931	21.9	0.019	8
Base Region	1.1 Hz / 33 mm	0.646	0.324	0.443	0.723	26.2	0.030	67

Table 5.3: St' value based on u' predictor, pin fin wall, wall normal distance 14 mm

Case	Frequency Hz/ Amplitude mm	$U_{mean,RMS}$	$U'_{RMS,avg}$	Tu	u' (m/s)	HTC (W/m^2K)	St'	% error
Entry Region	0.665 Hz/ 27 mm	0.396	0.111	0.333	0.411	14.0	0.028	57
Entry Region	1 Hz / 27 mm	0.593	0.159	0.313	0.614	17.2	0.023	29
Entry Region	1.33 Hz / 27 mm	0.781	0.216	0.701	0.810	20.0	0.021	14
Central Region	0.665 Hz / 27 mm	0.055	0.062	0.265	0.082	11.2	0.112	524
Central Region	1 Hz / 27 mm	0.753	0.245	0.231	0.791	13.3	0.014	-23
Central Region	1.33 Hz / 27 mm	0.458	0.180	0.391	0.492	16.4	0.028	54
Base Region	0.665 Hz / 27 mm	0.495	0.163	0.336	0.521	17.3	0.028	53
Base Region	1 Hz / 27 mm	0.753	0.245	0.231	0.791	22.02	0.023	28
Base Region	1.33 Hz / 27 mm	1.01	0.322	0.327	1.055	27.2	0.021	19

Table 5.4: St' value based on u' predictor, pin fin wall, wall normal distance 10 mm

Case	Frequency (Hz) / Amplitude (mm)	$U_{mean,RMS}$	$U'_{RMS,avg}$	Tu	u' (m/s)	HTC (W/m^2K)	St'	% error
Entry Region	0.547 Hz/33 mm	0.179	0.131	0.383	0.222	14.02	0.052	191
Entry Region	0.82 Hz/ 33mm	0.671	0.193	0.351	0.698	17.6	0.021	16
Entry Region	1.1 Hz/ 33mm	0.881	0.247	0.288	0.915	21.00	0.019	6
Central Region	0.547 Hz/ 33mm	0.160	0.071	0.411	0.175	11.2	0.053	193
Central Region	0.82 Hz/ 33mm	0.259	0.115	0.399	0.283	12.9	0.038	110
Central Region	1.1 Hz/33mm	0.360	0.149	0.359	0.390	16.3	0.035	92
Base Region	0.547 Hz/ 33 mm	0.282	0.158	0.422	0.323	16.9	0.043	141
Base Region	0.82 Hz/ 33mm	0.671	0.193	0.351	0.698	21.9	0.026	44
Base Region	1.1 Hz/ 33mm	0.694	0.310	0.394	0.760	26.2	0.029	59

5.3 Model Performance

When results of Table 5.1 are compared, it can be seen that Maciejewski's St' model performs best in the entry region and the base region. The overall error percentage in the entry region for St' value is less than 25%. The performance of the model in base region is good, but at lower frequencies. At lower frequencies, the error percentages are low (less than 25%) but at higher frequencies, the error percentages are high (30-35%). The central region Stanton number values are unreasonably overpredicted using the Maciejewski model. As was seen from the heat flux plots in Chapter 2, the central region was basically convection dominated than turbulence dominated. When we use the Maciejewski model for the central region and attribute the average speed to turbulence, it is equivalent to overpredicting the contribution due to turbulence on heat transfer. Maciejewski model performance must be modified in the case of pin fins. Due to increased three dimensionality of the flow, measurement of the selected single component of velocity at a point might not be representative of the entire flow field for application to heat transfer-velocity modeling.

5.4 Conclusions

The flow characteristics in the agitated domain in all the three regions is different from each other and complex. A single correlation does not work well for all the three regions. The entry region and base region could be correlated reasonably well with Maciejewski's correlation using the value offered by Maciejewski. Central region could not be correlated so well with the model and its recommended value. The Maciejewski model does not perform well in the presence of pin fins.

Chapter 6

Actual Scale Simulations

Numerical simulations have been used for an efficient heat sink design. In this heat sink design, the overall heat sink geometry, given by the channel height, fin thickness, and total length and width of the heat sink base is fixed. The total flow rate is also fixed. Thus, increasing the number of channels in the heat sink will lead to an increase in area but a decrease in width of each channel. The width of a single channel has been found to affect the heat transfer coefficient and also the power needed to drive the agitator. In this study, numerical methods have been used to find the optimal channel width and number of channels that provide the best thermal performance with agitation and throughflow and with the minimum power consumption to drive the agitator assembly.

6.1 Numerical Simulation Setup

A single channel is simulated to represent the whole heat sink. Computing a single channel makes the computation less expensive (Figure 6.1). This can be done due to symmetry. The inlet condition to the channel is defined as a velocity inlet with constant and uniform velocities and temperature (300K) flow. The walls of the channels are defined as uniform temperature walls (320K) and the agitator is defined with adiabatic moving walls. User-defined functions and dynamic meshes are employed to simulate movement of the agitator. A constant value of pressure is specified at the outlet.

Fluid flow and heat transfer inside the channel were calculated using a transient pressure-based solver. The realizable κ-ε turbulence model, with enhanced wall treatment near the walls, was used to capture the turbulence characteristics. As discussed in the following

section 6.1.1, this choice of model gave a good match with experimental results. The SIMPLE algorithm was used to solve pressure-velocity coupling. The convergence criterion was chosen as 10^{-4} for continuity, turbulence, and momentum equations and a criterion of 10^{-6} was used for the energy equation. Table 6.1 shows the parameters for all five cases being studied. Fin height (H=24 mm), fin thickness (w_{fin}=1 mm), channel length (L=50 mm), agitator thickness (t=1mm), minimum distance between the agitator and the channel wall (δ_{min}=0.5mm) and the clearance between the agitator and the fin base (δ_{tip}=1mm) have been kept constant for all the cases. The total flow rate (31.5 CFM) for the heat sink is also the same for all the cases. Keeping the total flow rate constant, increasing channel width leads to a decrease in the total number of fins and thus affects the flow rate per channel and inlet velocities. As can be seen in Table 6.1, under these conditions, the inlet velocities are different for all five cases. The minimum distance (δ_{min}) between the agitator and the channel wall is the same for each case, considering that for a practical case, one would be limited by the clearance between the channel and the agitator when the agitator is closest to the channel wall. Once the minimum distance δ_{min} is fixed, knowing the channel width and the agitator thickness, one can calculate the amplitude for each case. The frequency of oscillation was kept constant at 1000Hz for all the cases, since for a single channel of the heat sink, Yeom et al. [36] were able to achieve such high frequencies. Their results demonstrated heat transfer coefficients as high as 300W/m^{2}K.

6.1.1 Validation of the Numerical Model

Yeom et al. [36] carried out an experimental study with a channel of the heat sink being cooled by throughflow and agitation. The channel in their study simulated a portion of an

air cooled heat sink. They studied several cases by varying the throughflow velocity, agitation amplitude and agitation frequency. Numerical simulations were conducted for three different experimental cases of specified frequency, amplitude and throughflow velocity. The numerical scheme was able to simulate experimental heat transfer results within 8%. After validation of the numerical scheme, it was used to simulate the single channel cases for the current study.

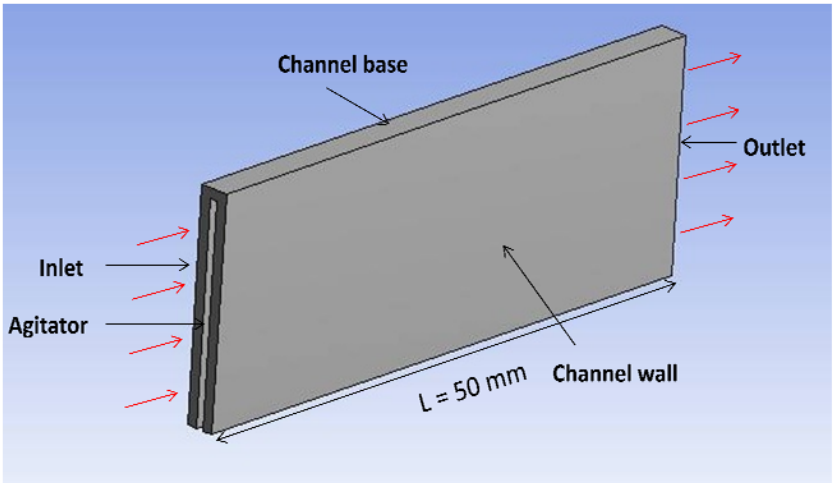

Figure 6.1: Numerical model for simulation of single channel

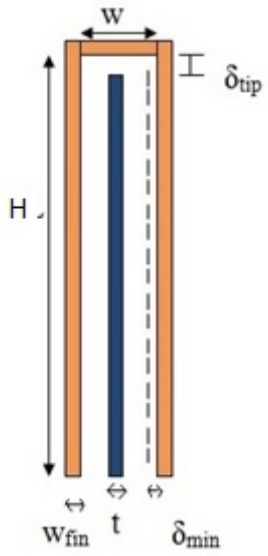

Figure 6.2: Channel in two dimensional view

Table 6.1: Parameters for cases being studied

Case	1	2	3	4	5
Channel height H (mm)	24	24	24	24	24
Channel thickness W_{fin} (mm)	1.0	1.0	1.0	1.0	1.0
Channel length L (mm)	50	50	50	50	50
Channel width w (mm)	2.9	3.4	3.9	4.4	4.9
Total heat sink width (mm)	114	114	114	114	114
Number of channels	29	26	23	21	19
Amplitude (mm)	0.45	0.7	0.85	1.2	1.45
Frequency (Hz)	1000	1000	1000	1000	1000
Total flow rate (CFM)	31.5	31.5	31.5	31.5	31.5
Inlet velocity (m/s)	11.2	9.9	9.3	8.7	8.4

Table 6.2: Grid independence study

Grid Size (total number of cells)	Heat Transfer Coefficient (W/m^2K)
939575	369
1358970	359
1727448	375

6.1.2 Grid Independence Study

A study was done by varying the mesh size to establish grid independence. Heat transfer coefficients were computed for different mesh sizes. A grid independence study was done for case 2, shown in Table 6.1. The heat transfer coefficients for different mesh sizes are

listed in Table 6.2. From Table 6.2, it can be seen that the maximum difference between any two cases is less than 4%. Thus, grid independence was established.

6.2 Data Reduction

The average heat transfer coefficient for a single channel is used for calculating the overall thermal resistance of the heat sink. It is defined as:

$$h_{single} = \frac{q}{A_{single}\Delta T} \tag{6-1}$$

where q is the power input to the heated wall obtained from the numerical simulation and A_{single} is the total convective heat transfer area for a single channel. The temperature difference, ΔT, is the channel log mean temperature difference defined as:

$$\Delta T = \frac{(T_{channel\_in} - T_{air\_in}) - (T_{channel\_out} - T_{air\_out})}{\ln[(T_{channel\_in} - T_{air\_in}) - (T_{channel\_out} - T_{air\_out})]} \tag{6-2}$$

$T_{channel\_in}$ and T_{air_in} have been specified as boundary conditions in the numerical simulation. The air outlet temperature, T_{air_out}, has been calculated using an energy balance method. The total heat flux dissipated from the channel can be obtained from the numerical simulation. Thus, knowing the mass flow rate and heat flux, using energy balance one can calculate the temperature drop across the channel and obtain T_{air_out}.

The power needed to drive the agitator assembly is also obtained from numerical simulation. The instantaneous power needed to drive the agitator assembly is calculated as:

$$P_t = p_t * V_t * A_{agitator} \tag{6-3}$$

where p_t is the surface averaged static pressure on the agitator surface, V_t is the agitator velocity and $A_{agitator}$ is the area of the agitator surface. The power computed from above is averaged during a cycle to report the power consumption for a particular case.

6.3. Results and Discussion

6.3.1 Heat Transfer Results

The heat transfer performance values of different cases under the same operating frequency have been compared. Table 6.3 shows the heat transfer coefficient variation with channel width. As can be seen from the table, the heat transfer coefficient increases as the channel width increases. As mentioned earlier, the minimum distance (δ_{min}) between the agitator and the wall is kept the same for all five cases, which requires that the amplitude of oscillation of the agitator increases with increasing channel width. The peak velocity of the agitator is governed by the product of frequency and amplitude of the agitator. The peak agitator agitation velocity can be given as:

$$V_{peak} = 2\pi af \tag{6-4}$$

where V_{peak} is the peak agitation velocity, a is the amplitude of oscillation and f is the frequency of oscillation. As the channel width increases, the agitation velocity increases due to the increasing amplitude, frequency being constant for all cases. Increasing agitation velocity increases flow agitation near the wall, thus enhancing heat transfer. The increase in channel width also leads to generation of larger scale vortices which subsequently enhance heat transfer.

Figure 6.3 shows the heat flux distribution on the channel wall for channel widths of 2.9 mm and 4.9 mm. The boundaries of the channel have been marked on the figure to specify inlet, outlet and the channel base. For reference, one can look at Fig. 6.1. As can be seen in Figure 6.3, wider channels have higher heat flux dissipation. The heat flux is higher at the entry of the channel and at the end where a narrow gap (δ_{tip}) exists between the agitator tip and the channel wall. This is due to flow separation and reattachment at

the entry of the channel and generation of vortices in the narrow tip gap region. The vortex generation in the narrow tip gap region is further explained in section 6.3.2.

Table 6.3: Agitation velocity and heat transfer coefficient variation with channel width

Case	Channel Width (mm)	Aspect Ratio (L/W)	Peak Agitation velocity (m/s)	Heat Transfer Coefficient (W/m^2K)
1	2.9	8.1	2.8	311
2	3.4	6.9	4.4	359
3	3.9	6.0	5.3	374
4	4.4	5.4	7.5	486
5	4.9	4.8	9.1	577

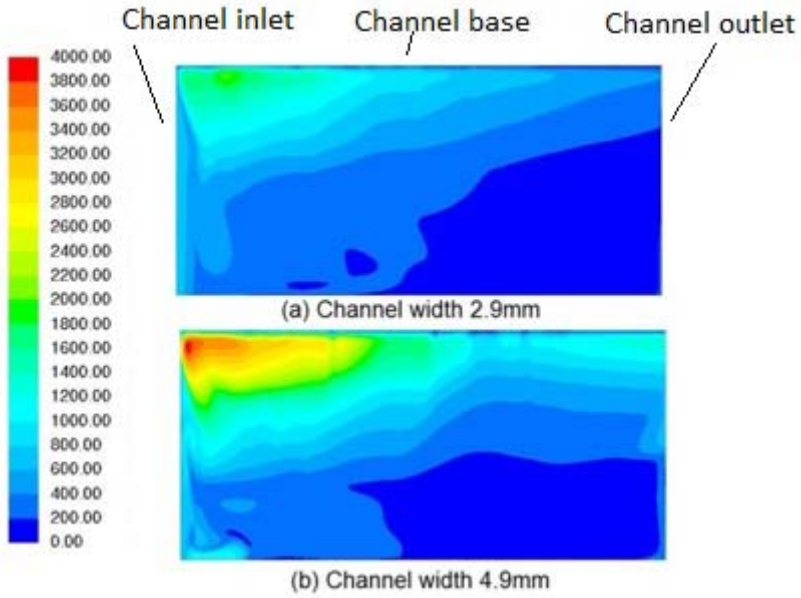

Figure 6.3: Heat flux (W/m^2) distribution comparison for channels with different widths

Figure 6.4 shows the effective thermal resistance vs. channel aspect ratio for the heat sink after using heat transfer coefficient data for a single channel from Table 6.3 and extending it to other channels in the heat sink. Effective thermal resistance for the heat sink can be calculated as

$$R_{th} = \frac{1}{h_{single} A_{total}} \tag{6-5}$$

where R_{th} is thermal résistance for the heat sink, h_{single} is the convective heat transfer coefficient computed for single channel, A_{total} and is the total convective area of the heat sink

As can be seen from Figure 6.4, low aspect ratio channels that are wider lead to lower thermal resistance in the heat sink. Lower aspect ratio channels have more flow mixing, leading to higher heat removal for a single channel. However, when the channel aspect ratio is lower, the total number of channels in the heat sink is also reduced. Thus, as the aspect ratio starts increasing, one first notices an increase in thermal resistance, followed by a small decrease and finally, an increase again. There is a tradeoff between two competing effects, enhanced heat transfer due to higher agitation velocities when the channels are wider, but reduced total heat transfer area due to a decrease in the total number of channels in the heat sink. According to the thermal resistance results in Figure 6.4, the desirable case would be channels with lower aspect ratios. However, to find an optimal strategy, one needs to look at the coefficient of performance (COP), that is the ratio of thermal power removed to the power input to drive the agitator assembly. This will be discussed in a later section.

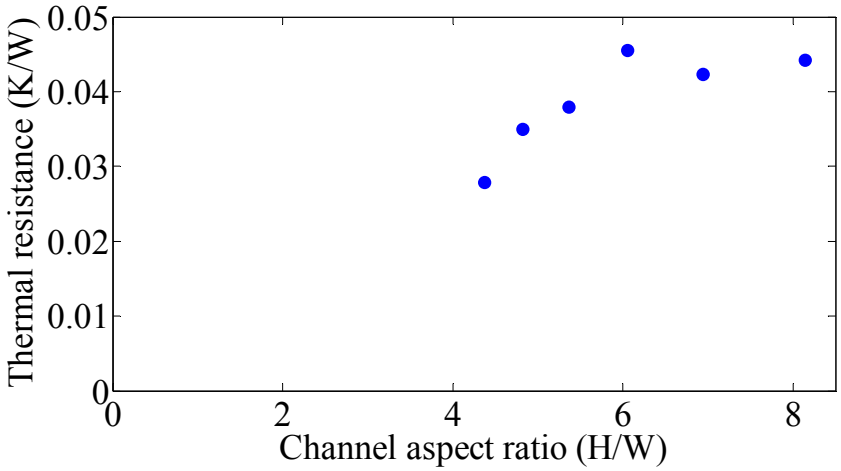

Figure 6.4: Thermal resistance variation with channel aspect ratio

6.3.2 Turbulence Generated

To explain the observed heat transfer trends, turbulence plots have been extracted from the numerical simulation. Figures 6.5 and 6.6 show turbulence kinetic energy plots at five different instants within one agitation cycle for two cases with different channel widths. As can be seen from Figs. 6.5 and 6.6, higher levels of turbulence are generated in wider channels. The scales of turbulence kinetic energy in the legends are different for the two figures. This was done so that the distribution of turbulence along the channel could be observed effectively for both the cases. The level of turbulence generated is high near the base of the channel where a narrow gap (δ_{tip}) exists between the agitator and channel base. Velocities are high in the narrow gap (δ_{tip}) between the agitator and the channel base, which leads to an increase in heat transfer in this region. This narrow gap also leads to generation of vortices. The vortices are able to penetrate more along the channel wall length in the case of a wider channel than for a narrower channel, as can be seen by comparing plots 6.5 and 6.6. This can explain the observed enhancement in convective heat transfer as the channel width increases.

6.3.3 Power Input to Drive the Agitators

The power needed to drive a single agitator for the various cases is shown in Fig. 6.7. Figure 6.8 shows the power needed to drive the agitator assembly for the entire heat sink as the channel aspect ratio increases. This power is needed to drive the agitator against the fluid pressure forces. The power needed to drive the agitator assembly is significantly higher for low aspect ratio channels. As discussed earlier, for low aspect ratio channels, the agitation velocities are higher, which leads to considerable enhancement in heat transfer.

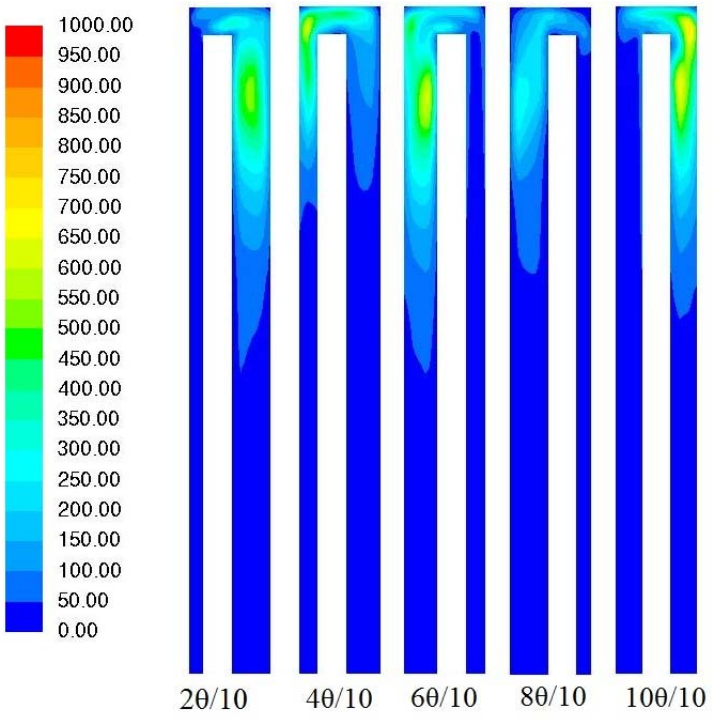

Figure 6.5: Turbulence kinetic energy (m^2/s^2) plot for the case with a channel width of 2.9 mm at five different instants within one cycle (θ is cycle time)

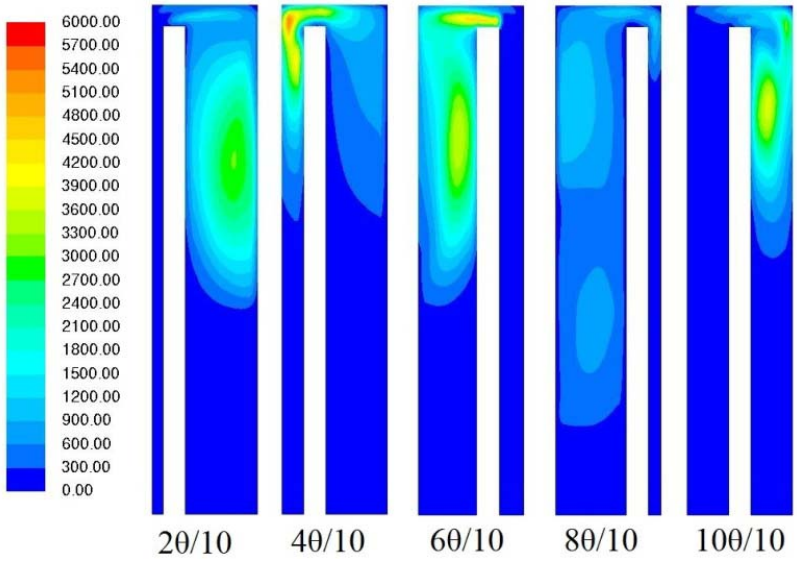

Figure 6.6: Turbulence kinetic energy (m^2/s^2) plots for the case with a channel width of 4.9 mm at five different instants within one cycle (θ is cycle time)

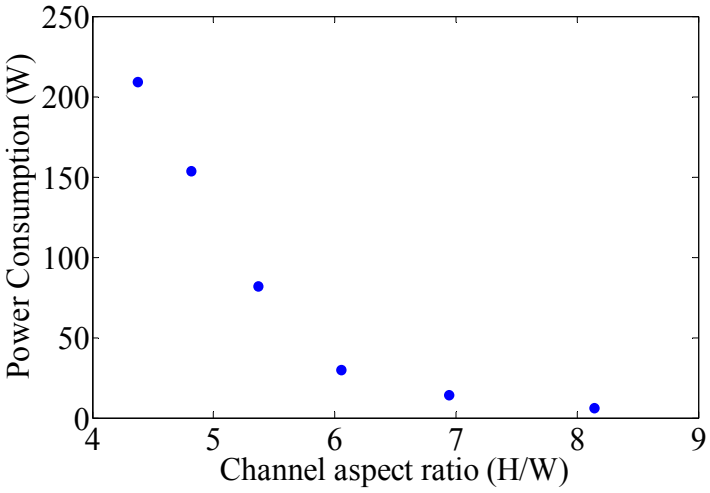

Figure 6.7: Power input to drive a single agitator as the channel aspect ratio increases

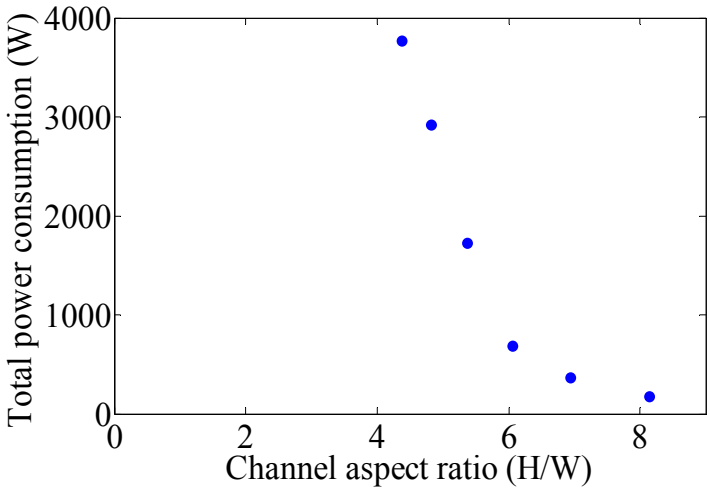

Figure 6.8: Power input to drive the agitator assembly as the channel aspect ratio increases

However, one pays the price for the heat transfer enhancement by pumping in more power to drive the agitator assembly faster. Huang et al. [98] carried out a numerical study to estimate the power needed to drive active devices in air cooled heat sinks. It was found that the fluid power (with the drive inefficiencies extracted) needed to drive such devices was proportional to the cube of the velocity of the moving part. Thus, with continually increasing agitation velocity, the power requirement for driving the agitators is very large. The large amount of power input required makes it desirable to find a strategy in designing heat sinks which can give low thermal resistance with low agitation velocities

6.4 Coefficient of Performance

To find the optimal agitator design, the coefficient of performance (COP) has been compared for different cases.

$$COP = \frac{P_{thermal}}{P_{agitator}} \tag{6-6}$$

The Coefficient Of Performance (COP) has been defined as the ratio of thermal power ($P_{thermal}$) removed from the heat sink when the peak surface temperature is 15K higher than the air inlet temperature to the power input to drive the agitator assembly ($P_{agitator}$). Figure 6.9 shows the variation of COP with channel aspect ratio.

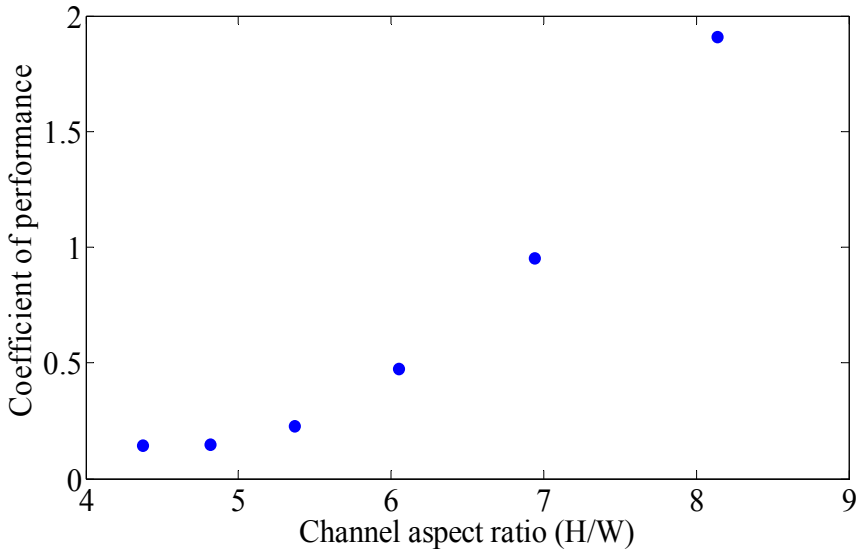

Figure 6.9: Variation of channel Coefficient of Performance (COP) with channel aspect ratio

As can be seen from Fig. 6.9, the coefficient of performance increases as the channel aspect ratio increases. Thus, heat sinks with narrower channels have higher coefficients of performance. As explained earlier, the thermal performance of wider channels was better due to higher agitation velocities but one pays a significant price for the improved thermal performance in terms of the power needed to drive the agitator assembly. For narrower channels, although the thermal performance is less than with the wider channels, there is a significant drop in the amount of power needed to drive the agitator assembly. Thus, a heat sink with a higher aspect ratio and, thus, longer, narrower

channels exhibits a better coefficient of performance than a heat sink with wider channels.

6.5. Conclusions

This study numerically investigated the design of a heat sink with agitated channels. The channel aspect ratio plays an important part in the design since it affects the total number of channels for a fixed size heat sink and also convective heat transfer enhancement obtained due to agitation. The flow rate for the entire heat sink has been kept constant at 31.5 CFM for all the cases. Also, the frequency of agitation was kept constant at 1000 Hz for all cases. Under these conditions it was found that for wider channels, the heat transfer coefficient is higher. This is due to higher agitation velocities that can be obtained in wider channels due to higher amplitude of oscillation. Also, there is strong vortical activity between the agitator tip and channel base. The effect of this activity is greater in a wider channel, both in terms of magnitude and length of the channel wall that is influenced by it. The thermal resistance for wider-channel heat sink was found to be lower.

A study was also done to compute the total amount of power needed to drive the agitator assembly. It was found that though wider channels lead to lower thermal resistance, they cause very high power consumption. The high power consumption was attributed to higher agitation velocities. Power consumption increases with the third power of the agitation velocity. When a coefficient of performance study was done to compare the ratio of thermal power removed from the heat sink to the power input needed to drive the agitator assembly, it was found that narrower channels were favored. Thus, it was

concluded that under the design parameters mentioned in Table 6.1, the optimal strategy would be to move towards heat sinks with narrower channels.

For future design purposes, a good strategy would be to keep the agitation velocities constant for all cases. In this study it was found that by maintaining constant frequency, wider channels have higher agitation velocities which lead to large power consumption levels. Future design studies could be done by keeping the agitation velocities across all cases constant, so that wider channels would have higher amplitudes but lower operational frequencies. In that way the power consumption for the wider channels would be reasonable and one could then compare the thermal performance for wider and narrower channels.

The contents in this Chapter have been reproduced from the following publication with permission from ASME

S. Agrawal, L. Huang, T. Simon, M. North, T. Cui, "Effects of Channel Aspect Ratio on Convective Heat Transfer in an Electronics Cooling Heat Sink having Agitation and Fan Induced Throughflow," ASME Summer Heat Transfer Conference-17182, Minneapolis, USA, July 2013

Chapter 7

Conclusions

7.1 Agitator Performance in Plain Wall Region

A translating agitator blade can provide high heat transfer enhancement inside a channel. The agitator, with its movement back and forth, disturbs the flow sufficiently to generate increased mixing. Test data that show the flow unsteadiness and the heat transfer enhancement due to the unsteadiness are generated in a test facility that isolates, as well as one can, unsteadiness effects by having minimal steady, mean convection. This study has application in electronics cooling where the channels of the heat sink can be cooled by translationally oscillating plates called agitators. A translating blade could be oscillated in a channel through which there is a mean through-flow. The oscillation would generate unsteadiness and turbulence leading to strong mixing and augmentation of heat transfer. This is the arrangement that this research team has used in the design of a next generation heat sink for electronics cooling. The present study lends insight into the agitation effects while attempting to isolate them from the effects of mean channel through-flow.

A mock up unit to demonstrate the effectiveness of agitation for convective cooling in a channel was fabricated. The channel domain was spatially resolved into three regions, namely the entry region, central region and the base region. The entry region is at the channel entrance where the flow enters and leaves the channel. The central region is in the center of the channel. The base region is near the channel base.

In the entry region, the flow is an unsteadily-driven channel flow and an abrupt entry flow. In the central region, the flow is an unsteadily-driven channel flow in one direction and a highly turbulent flow washed from the base region in the other direction. The central region shows the lowest heat transfer rates. The sloshing velocities are lowest in magnitude in this region. This region does experience some streaking activity; however, it is not strong enough to generate heat transfer rates as high as those in the base region. In the base region, the flow is a channel flow in one direction and a jetting and highly vortical flow in the other direction. The highest velocities and turbulence levels are found in the base region due to the narrow tip gap between the agitator tip and tip wall. This narrow gap leads to generation of strong vortices. The heat transfer rates are also the highest in this region, which is as expected, based on the velocity data. The three regions have considerably different unsteadiness characteristics.

In the entry region and the base region, increases in turbulence are found toward the end of the acceleration phase and are carried over to the deceleration phase. Decay of turbulence starts at the end of the deceleration phase. The central region is basically a convection dominated region.

A parametric study was carried out to quantify the effects of different parameters like frequency, amplitude and agitator velocity on heat transfer and the velocity field. It was found that the heat transfer coefficient increases with an increase of frequency, which was expected. The ensemble-averaged mean velocity and the ensemble-averaged RMS fluctuating velocity simply scaled with a change in frequency. No change in flow characteristics was found with a change in frequency.

An increase in amplitude lead to an increase in heat transfer coefficient for the entry region and base region with the increase in the central region being less significant. For the entry region, an increase in mean velocity was found with a change in amplitude, with variations in flow characteristics. An increase in turbulence production was found during the deceleration phase with an increase in amplitude. For the central region, an increase in mean velocity was found during a certain phase of the agitator motion for higher amplitudes whereas for other phases the lower amplitude case showed higher velocities. It was observed that the fluctuating velocity increased with an increase in amplitude. For the base region, higher amplitude cases showed an increase in mean velocity without changes in flow characteristics during different phases. No increase in fluctuating velocity was observed with an increase in amplitude for the base region.

A study was done to test the effect of agitation velocity on heat transfer coefficient and velocity. For this, different cases were run such that the product of amplitude and frequency remained constant to maintain a constant agitation velocity. In general, it was found that the agitation velocity was the governing factor in determining the heat transfer coefficient. This was also supported by the ensemble-averaged mean velocity plots and the ensemble-averaged RMS fluctuating plots.

Experiments were run to measure unsteady heat flux for each of the three regions; entry region, central region and base region. It was found the unsteady heat flux values for the entry region and base region were turbulence dominated whereas the unsteady heat fluxes of central region were convection dominated.

7.2 Agitator Performance in the Presence of Pin Fins

Velocity and heat transfer measurements were also done on a channel wall augmented with pin fins. When the heat transfer coefficients for entry region were compared with the plain wall heat transfer coefficients based on projected area, an increase of 35-40% was reported. Based on the total wetted area, an increase of around 5% was noticed in heat transfer coefficient accompanied with a 30% increase in area. When the heat transfer coefficients (based on projected area) for pin fin case for the central region were compared with plain wall case, it was found that an increase of 35% was observed for an amplitude of 27 mm, whereas an increase of around 25% was observed for the amplitude case 33 mm. Based on the total wetted area, an increase of 3-4% was observed for the amplitude case 27 mm and a decrease of 3-4% was observed for the amplitude case 33 mm. For the base region, an increase of around 25% was found in heat transfer coefficient for pin fins when the heat transfer coefficient was computed based on projected area. When the heat transfer coefficient was compared based on the total wetted area, a decrease of around 5% was found when compared to the plain wall case.

At a particular agitation velocity, the heat transfer coefficient for pin fins was found to be constant irrespective of the values of amplitude and frequency for all the three regions. This was also observed for the plain wall case.

Velocity measurements were made at different wall-normal distances with pin fins on the channel wall. Velocity profiles in the pin fin and plain-wall cases were compared for all the three regions. Closer to the wall; that is, inside the pin fin array, more momentum loss was experienced as compared to outside the pin fin array. Flow blockage was experienced in the presence of pin fins in the base region.

The effects of frequency on heat transfer coefficient and velocity fields were studied. It was found that the heat transfer coefficients increased with an increase in frequency. For the most part, the velocities simply scaled with changes in frequency without any changes in flow characteristics except for the base region during phase 1, when the level of velocity fluctuation remained invariant with changes in frequency.

7.3 Modeling of Heat Transfer Data

An attempt to model the heat transfer coefficient with velocity in the case of the plain wall and pin fin wall was made. The agitated flow has two major mixing mechanisms - sloshing velocity and fluctuating velocity. The Maciejewski model available in the literature was used for modeling. The Maciejewski model, which uses a single u' predictor worked well for the base region and the entry region. The central region was overpredicted using the Maciejewski model. It appears that the central region, which was convection dominated could not be correlated with a turbulence model. The Maciejewski model did not work well for the pin fin case. It appears that the single point velocity measurement for pin fins was not a good representation of point velocity measurement for modeling, since in the case of pin fins, the three dimensionality of the flow increases.

7.4 Actual Scale Simulations

ANSYS Fluent numerical simulations were run in support of the design of the heat sink. The overall heat sink geometry, that is the length, height and width of the heat sink were kept fixed. The total cross flow rate was also fixed. The width of a single channel of the heat sink was varied for the different cases being studied. With the width, the total number of channels in the heat sink also varies. A heat sink with a wider channel has lesser total number of channels than a heat sink with narrower channels. It was found

that, though the thermal performance was better in the case of wider channels, due to increased agitation velocities, one pays a huge price in terms of the power needed to drive the agitator. Thus, the coefficient of performance is better for the heat sink with narrower channels.

7.5 Proposal for Future Work

The agitator contributes to sufficient mixing and turbulence activity inside a channel domain. In combination with throughflow, it can be used in cooling of heat sinks for electronics cooling applications.

This study explored the effectiveness of an agitator in a mock up experiment by studying agitation alone with smooth wall and wall augmented with pin fins. Future studies could be done to study the effectiveness of an agitator in conjunction with throughflow in a mock up experiment. In the presence of throughflow, studies could be done to find an optimal combination of throughflow speed and agitation speed that would lead to maximum heat transfer enhancement.

Studies could also be done to investigate the effect of the configuration of agitator such as the effectiveness of having single long agitator vs. multiple short agitators. The agitator shape in this experiment was rectangular. Studies could be done to find if a geometric modification like including notches at the agitator tip could lead to the generation of additional vortices.

This study demonstrated the high heat transfer that could be obtained with an agitator. Future studies could be aimed at configuration and geometric optimization to obtain more benefit from this technique. Some suggestions have been listed above.

References

[1] G. E. Moore, “Cramming More Components onto Integrated Circuits,” Proceedings of the IEEE, 86(1), pp. 82-85, 1998

[2] I. Mudawar, “Assessment of High Heat Flux Thermal Management Schemes”, IEEE Transactions on Components and Packaging Technologies, 24(2), pp 122-141, 2001

[3] B. Agostini, M. Fabbri, J. E. Park, L. Wojtan, J. R. Thome, B. Michel, “State of the Art of High Heat Flux Cooling Technologies,” Heat Transfer Engineering, 28(4), pp258-281, 2007

[4] R. Mahajan, “Cooling a Microprocessor Chip,” Proceedings of the IEEE, 94(8), 1476-1486, 2006

[5] R. C. Chu, “ A Review of IBM Sponsored Research and Development Projects for Computer Cooling,” Fifteenth Annual Semiconductor Thermal Measurement and Management Symposium, San Diego, USA, 151-165, 1999

[6] M. J. Ellsworth, Jr, L. A. Campbell, R. E. Simons, M. K. Iyengar, R. R. Schmidt, R. C. Chu, “The Evolution of Water Cooling for Large Server Systems: Back to the Future”, Proceedings of the 2008 ITHERM Conference, Orlando, FL, USA, 266-274, 2008

[7] M. J. Ellsworth, G. F. Goth, R. J. Zoodsma, A. Arvelo, L. A. Campbell, W. J. Anderl, “An Overview of the IBM Power 775 Supercomputer Water Cooling System”, Journal of Electronic Packaging, 134(2), 020906(1-9), 2012

[8] R. S. Prasher, J. Y. Chang, I. Sauciuc, S. Narasimhan, D. Chau, G. Chrysler, A. Myers, S. Prstic, C. Hu, “Nano and Micro Technology-Based Next-Generation Package-Level Cooling Solutions”, Intel Technology Journal, 9(4), 285-296, 2005

[9] P. Naphon, O. Khonseur, “Study on the Convective Heat Transfer and Pressure Drop in Microchannel Heat Sink,” International Communications in Heat and Mass Transfer, 36(1), 39-44, 2009

[10] X. L. Xie, W. Q. Tao, Y. L. He, “Numerical Study of Turbulent Heat Transfer and Pressure Drop Characteristics in a Water Cooled Minichannel Heat Sink,” Journal of Electronic Packaging, 129(3), 247-255, 2007

[11] J. R. Thome, “State of the Art Overview of Boiling and Two Phase Flows in Microchannels,” Heat Transfer Engineering, 27(9), 4-19, 2006

[12] M. B. Bowers, I. Mudawar, “Two Phase Electronic Cooling Using Mini Channel and Micro Channel Heat Sinks: Part 1-Design Criteria and Heat Diffusion Constraints,” Journal of Electronic Packaging, 116(4), 290-297, 1994

[13] M. B. Bowers, I. Mudawar, “Two Phase Electronic Cooling Using Mini Channel and Micro Channel Heat Sinks: Part 2-Flow Rate and Pressure Drop Constraints,” Journal of Electronic Packaging, 116(4), 298-305, 1994

[14] I. Mudawar, “Two Phase Microchannel Heat Sinks: Theory, Applications and Limitations,” Journal of Electronic Packaging, 133, 041002(2011)

[15] M. Fabbri, V. K. Dhir, “Optimized Heat Transfer for High Power Electronic Cooling Using Arrays of Microjets,” Journal of Heat Transfer, 127(7), 760-769, 2005

[16] S.P. Jang, S. J. Kim, “Fluid Flow and Thermal Characteristics of a Microchannel Heat Sink Subject to an Impinging Air Jet,” Journal of Heat Transfer, 127(7), 770-779, 2004

[17] M. K. Sung, I. Mudawar, "Single Phase Hybrid Micro channel/Micro jet Impingement Cooling," International Journal of Heat and Mass Transfer, 51(17-18), 4342-4352, 2008

[18] M. K. Sung, I. Mudawar, "Experimental and Numerical Investigation of Single Phase Heat Transfer using a Hybrid Jet-Impingement/Micro-Channel Cooling Scheme," International Journal of Heat and Mass Transfer, 49(3-4), 682-694, 2006

[19] M. K. Sung, I Mudawar, "Single Phase and Two Phase Hybrid Cooling Schemes for High Heat Flux Thermal Management of Defense Electronics," Journal of Electronic Packaging, 131(2), 021013(1-10), 2009

[20] Y. Fan, P.S. Lee, L. W. Jin, B. W. Chau, "A Simulation and Experimental Study of Fluid Flow and Heat Transfer on Cylindrical Oblique Finned Heat Sink," International Journal of Heat and Mass Transfer, 61, 62-72, 2013

[21] V. Egan, J. Stafford, P. Walsh. E. Walsh, "An Experimental Study on the Design of Miniature Heat Sinks for Forced Convection Air Cooling," Journal of Heat Transfer, 131(7) 071402(1-9), 2009

[22] T. Y. Kim, S. J. Kim, "Fluid Flow and Heat Transfer Characteristics of Cross Cut Heat Sinks," International Journal of Heat and Mass Transfer, 52(23-24), 5358-5370, 2009

[23] K. Yang, C. Chiang, Y. Lin, K. Chien, C. Wang, "On the Heat Transfer Characteristics of Heat Sinks: Influence of Fin Spacing at Low Reynolds Number Region," International Journal of Heat and Mass Transfer, 50(13-14), 2667-2674, 2007

[24] P. D. Quinones, L. S. Mok, “Multiple Fan-Heat Sink Cooling System With Enhanced Evaporator Base: Design, Modeling and Experiment,” Journal of Electronic Packaging, 131(3), 031009(1-8), 2009

[25] V. Egan, P. A. Walsh, E. Walsh, R. Grimes, “Thermal Analysis of Miniature Low Profile Heat Sinks With and Without Fins”, Journal of Electronic Packaging, 131(3), 031004(1-11), 2009

[26] Sheng-Fu Liu, Ren-Tsung Huang, Wen-Jenn Sheu, Chi-Chuan Wang, “Heat Transfer by a Piezoelectric Fan on a Flat Surface Subject to the Influence of Horizontal/Vertical Arrangement”, International Journal of Heat and Mass Transfer, 52(11-12), 2565-2570, 2009

[27] T. Acikalin, S. V. Garimella, A. Raman, J. Petroski, “Characterization and Optimization of the Thermal Performance of Miniature Piezoelectric Fans”, International Journal of Heat and Fluid Flow, 28(4), 806-820, 2007

[28] M. Kimber, S. V. Garimella, “Measurement and Prediction of the Cooling Characteristics of a Generalized Vibrating Piezoelectric Fan”, International Journal of Heat and Mass Transfer 52(19-20), 4470-4478, 2009

[29] M. Kimber, S. V. Garimella, “Cooling Performance of Arrays of Vibrating Cantilevers”, Journal of Heat Transfer, 131, 11401(1-8), 2009

[30] T. Acikalin, S. V. Garimella, “Analysis and Prediction of the Thermal Performance of Piezoelectrically Actuated Fans”, Heat Transfer Engineering, 30(6), 487-498, 2009

[31] Chien-Nan Lin, “Analysis of Three-Dimensional Heat and Fluid Flow induced by Piezoelectric Fan”, International Journal of Heat and Mass Transfer, 55(11-12), 3043-3053, 2012

[32] H. K. Ma, H. C. Su, C. L. Liu, W. H. Ho, “Investigation of a Piezoelectric fan Embedded in a Heat Sink”, International Communications in Heat and Mass Transfer, 39, 603-609, 2012

[33] T. Y.Kim, Dong-Kwon Kim, S. J. Kim, “Scroll heat sink: A Novel Heat Sink with the Moving Fins inserted between the Cooling Fins,” International Journal of Heat and Mass Transfer, 51(13-14), 3267-3274, 2008

[34] J. Kim, S. J. Kim, “Heat Transfer Characteristics of a Centrifugal Heat Sink,” International Journal of Heat and Mass Transfer, 56(1-2), 188-196, 2013

[35] J. M. Allison, W. L. Staats, M. McCarthy, D. Jenicek, A. K. Edoh, J. H. Lang, E. N. Wang, J. G. Brisson, “ Enhancement of Convective Heat Transfer in an Air Cooled Heat Exchanger using Interdigitated Impeller Blades,” International Journal of Heat And Mass Transfer 54(21-22), 4549-4559, 2011

[36] T. Yeom, T. W. Simon, L. Huang, M. North, T. Cui, “Piezoelectric Translational Agitation for Enhancing Forced-Convection Channel-Flow Heat Transfer,” International Journal of Heat and Mass Transfer, 55(25-26), 7398-7409, 2012

[37] Y. Yu, T. W. Simon, S. Agrawal, M. North, T. Cui, “A Computational Study of Active Heat Transfer Enhancement of Air Cooled Heat Sinks by Actuated Plates,” Proceedings of ASME International Mechanical Engineering Congress and Exposition, Denver, USA, IMECE 64526, 2011

[38] Y. Yu, T. W. Simon, M. Zhang, T. Yeom, M. North, T. Cui, “ Enhancing Heat Transfer of Air Cooled Heat Sinks using Piezoelectrically driven Agitators and Synthetic Jets,” Proceedings of ASME International Mechanical Engineering Congress and Exposition, Denver, USA, IMECE 64544, 2011

[39] T. Yeom, T. W. Simon, Y. Yu, M. North, T. Cui, "Convective Heat Transfer Enhancement on a Channel Wall with a High Frequency, Oscillating Agitator," Proceedings of ASME International Mechanical Engineering Congress and Exposition ,Denver, USA, IMECE 64379, 2011

[40] T. Yeom, T. W. Simon, Y. Yu, M. Zhang, S. Agrawal, L. Huang, T. Zhang, M. North. T. Cui, " An Active Heat Sink System with Piezoelectric Translational Agitators and Micro Pin Fin Arrays" Proceedings of ASME International Mechanical Engineering Congress and Exposition, Houston, Texas, IMECE 88449, 2012

[41] Y. Yu, T. W. Simon, M. North, T. Cui, "Comparison of Heat Transfer Enhancement by Actuated Plates in Heat Sink Channels," Proceedings of the ASME 2012 Summer Heat Transfer Conference, Puerto Rico, HT 58280, 2012

[42] S. Agrawal, T. Simon, M. North, T. Cui , "An Experimental Study on the Effects of Agitation on Forced-Convection Heat Transfer," ASME International Mechanical Engineering Congress and Exposition, Denver, USA, IMECE 64558, 2011

[43] S. Agrawal, T. Simon , M. North, T. Cui , "An experimental study on the effects of agitation in generating flow unsteadiness and enhancing convective heat transfer,"ASME Summer Heat Transfer Conference, Puerto Rico, HT-58273, 2012

[44] W. Bauer, J. Wenisch, J. B. Heywood, "Averaged and Time Resolved Heat Transfer of Steady and Pulsating Entry Flow in Intake Manifold of a Spark Ignition Engine," International Journal of Heat and Fluid Flow, 19(1), 1-9, 1998

[45] D. H. Davidson, R. O. Parker, "Heat Transfer to a Laminar Incompressible Fully Developed Pulsating Flow between Parallel Flat Plates," Journal of the Franklin Institute, 29(1), 57-78, 1971

[46] D. X. Jin, Y. P. Lee, D. Y. Lee, “Effects of the Pulsating Flow Agitation on the Heat Transfer in a Triangular Grooved Channel,” International Journal of Heat and Mass Transfer, 50(15-16), 3062-3071, 2007

[47] S. Qiu, T. W. Simon, “Measurements of Heat Transfer and Fluid Mechanics within an Oscillatory Flow in a Pipe,” Fundamentals of Heat Transfer in Forced Convection, Winter Annual Meeting, ASME HTD-Vol. 285,1-8, 1994

[48] S. A. Gbadebo, S. A. M. Said, M. A. Habib, “Average Nusselt Number Correlation in the Thermal Entrance Region of Steady and Pulsating Turbulent Pipe Flows,” Heat and Mass Transfer, 35(5), 377-381, 1999

[49] A. E. Zohir, M. A. Habib, A. M. Attya, A. I. Eid, “An Experimental Investigation of Heat Transfer to Pulsating Pipe Air Flow with Different Amplitudes,” Heat Mass Transfer 42(7), 625-635, 2006

[50] M. A. Habib, A. M. Attya, S. A. M. Said, A. I. Eid, A. Z. Aly, “Heat Transfer Characteristics and Nusselt Number Correlation of Turbulent Pulsating Pipe Air Flows,” Heat and Mass Transfer, 40(3-4), 307-318, 2004

[51] U. Akdag, M. Ozdemir, A. F. Ozguc, “Heat Removal from Oscillating Flow from in a Vertical Annular Channel,” Heat and Mass Transfer, 44(4), 393-400, 2008

[52] A. A. Al Haddad, Nourah Al-Binally, “Prediction of Heat Transfer Coefficient in Pulsating Flow,” International Journal of Heat and Fluid Flow, 10(2), 131-133, 1989

[53] A. R. Barker, J. E. F. Williams, “Transient Measurements of the Heat Transfer Coefficient in Unsteady, Turbulent Pipe Flow,” International Journal of Heat and Mass Transfer, 43(17), 3197-3207, 2000

[54] K. Azar, "Enhanced Cooling of Electronic Components by Flow Oscillation," Journal of Thermophysics and Heat Transfer, 6(4), 700-706, 1992

[55] P. K. Maciejewski, R. J. Moffat, "Heat Transfer With Very High Free-Stream Turbulence: Part 1-Experimental Data," Journal of Heat Transfer, 114(4), 827-833, 1992

[56] P. K. Maciejewski, R. J. Moffat, " Heat Transfer With Very High Free-Stream Turbulence: Part 2-Analysis of Results," Journal of Heat Transfer, 114(4), 834-839, 1992

[57] M. J. Barrett, D. K. Hollingsworth, "Heat Transfer in Turbulent Boundary Layers Subjected to Free Stream Turbulence-Part 1: Experimental results", Journal of Turbomachinery, 125(2), 232-241, 2003

[58] M. J. Barrett, D. K. Hollingsworth, "Heat Transfer in Turbulent Boundary Layers Subjected to Free Stream Turbulence-Part 2: Analysis and Correlation", Journal of Turbomachinery, 2003, 125(2), 242-251, 2003

[59] S. Qiu, T. W. Simon, "Measurements of Heat Transfer and Fluid Mechanics within an Oscillatory Flow in a Pipe," Fundamentals of Heat Transfer in Forced Convection, Winter Annual Meeting, ASME HTD-Vol. 285, 1-8, Winter Annual Meeting, 1994

[60] J. C. Simonich, P. Bradshaw, "Effect of Free Stream Turbulence on Heat Transfer through a Turbulent Boundary Layer," Journal of Heat Transfer, 100(4), 671-677, 1978

[61] M. F. Blair, "Influence of Free Stream Turbulence on Turbulent Boundary Layer Heat Transfer and Mean Profile Development, Part 1-Experimental Data," Journal of Heat Transfer 105(1), 33-40, 1983

[62] M. F. Blair, "Influence of Free Stream Turbulence on Turbulent Boundary Layer Heat Transfer and Mean Profile Development, Part 2-Analysis of Results," Journal of Heat Transfer 105(1), 41-47, 1983

[63] K. A. Thole, D. G. Bogard, "High Free Stream Turbulence Effects on Turbulent Boundary Layers," Journal of Fluids Engineering, 118, 276-284, 1996

[64] K. A. Thole, D. G. Bogard, "Enhanced Heat Transfer and Shear Stress due to High Free-Stream Turbulence," Journal of Turbomachinery, 117(3), 418-424, 1995

[65] F. E. Ames, "The Influence of Large Scale High Intensity Turbulence on Vane Heat Transfer," Journal of Turbomachinery 119, 23-30, 1997

[66] I. P. Castro, "Effects of Free Stream Turbulence on Low Reynolds number Boundary Layers," Journal of Fluids Engineering 106, 298-306, 1984

[67] J. S. Carullo, K. A. Thole, L. J. Zhang, H. K. Moon, S. Nasir, R. D. Cress, W. F. Ng, "The Effects of Free Stream Turbulence, Turbulence Length Scale, and Exit Reynolds Number on Turbine Blade Heat Transfer in a Transonic Cascade," Journal of Turbomachinery, 133(1) 011030(1-11), 2011

[68] S. He, J. D. Jackson, "A Study of Turbulence under Conditions of Transient Flow in a Pipe," Journal of Fluid Mechanics, 408, 1-38, 2000

[69] M. Hino, M. Kashiwayanagi, A. Nakayama, T. Hara, "Experiments on the Turbulence Statistics and the structure of a reciprocating oscillatory flow," Journal of Fluid Mechanics, 131, 363-400, 1983

[70] R. Akhavan, R. D. Kamm, A. H. Shapiro, "An Investigation of Transition to Turbulence in Bounded Oscillatory Stokes Flows Part 1. Experiments", Journal of Fluid Mechanics 225, 395-422, 1991

[71] T. S. Zhao, P. Cheng, "Experimental Studies on the Onset of Turbulence and Frictional Losses in an Oscillatory Turbulent Pipe Flow," International Journal of Heat and Fluid Flow, 17(4), 356-362, 1996

[72] K. H. Ahn, M. B. Ibrahim, “Laminar/Turbulent Oscillating Flow in Circular Pipes,” International Journal of Heat and Fluid Flow 13(4), 340-346, 1992

[73] Ann M. Anderson, R. J. Moffat, “A New Type of Heat Transfer Correlation for Air Cooling of Regular Arrays of Electronic Components”, Thermal Modeling and Design of Electronic Systems and Devices, HTD-Vol. 153, 27-39, ASME 1990

[74] R. A. Wirtz, W. Chen, “Laminar-Transitional Convection from repeated ribs in a channel”, Heat Transfer in Electronic Equipment, HTD-Vol. 171, 89-94, ASME 1991

[75] S. V. Garimella, P. A. Eibeck, “Onset of Transition in the Flow over a Three Dimensional Array of Rectangular Obstacles”, Thermal Modeling and Design of Electronic Systems and Devices, HTD-Vol.153, 1-6, ASME 1990

[76] P. T. Roeller, J. Stevens, B. W. Webb, “Heat Transfer and Turbulent Flow Characteristics of Isolated Three Dimensional Protrusions in Channels”, Thermal Modeling and Design of Electronic Systems and Devices, HTD-Vol.153, 7-13, ASME 1990

[77] S. Chien Siw, M. K. Chyu, T.I-P Shih, M. A. Alvin, “ Effects of Pin Detached Space on Heat Transfer and From Pin Fin Arrays”, ASME Turbo Expo, Glasgow, GT 2010-23227, 2010

[78] K. A. Moores, Y.K. Joshi, “Effect of Tip Clearance on the Thermal and Hydrodynamic Performance of a Shrouded Pin Fin Array”, Journal of Heat Transfer, 125(6), 999-1006, 2003

[79] E. Small, S.M. Sadeghipour, M. Asheghi, “ Heat Sinks with Enhanced Heat Transfer Capability for Electronic Cooling Applications”, Journal of Electronic Packaging, September 2006, Vol. 128/285

[80] C. Silva, E. Marotta, L. Fletcher, “Flow Structure and Enhanced Heat Transfer in Channel Flow With Dimpled Surface: Applications to Heat Sinks in Microelectronic Cooling”, Journal of Electronic Packaging, 129(2), 157-166, 2007

[81] R. F. Huang, S. W.Chang, Kun-Hung Chen, “Flow and Heat Transfer Characteristics in Rectangular Channels With Staggered Transverse Ribs on Two Opposite Walls”, Journal of Heat Transfer, 129(12), 1732-1736, 2007

[82] Kai-Shing Yang, Ching-Ming Chiang, Yur Tsai Lin, Kuo-Hsiang Chien, Chin-Chuan Wang, “On the heat transfer characteristics of heat sinks: Influence of fin spacing at low Reynolds number region”, International Journal of Heat and Mass Transfer, 50(13-14), 2667-2674, 2000

[83] M.A. Elyyan, D. K. Tafti, “Large Eddy Simulation Investigation of Flow and Heat Transfer in a Channel With Dimples and Protusions”, Journal of Turbomachinery, 130(4), 041016(1-9), 2008

[84] A. Korichi, L. Oufer, “Unsteady Heat Transfer and Pressure Drop in Channels with Obstacles mounted on the Upper and Lower Walls,” Numerical Heat Transfer, Part A-48, 711-729, 2005

[85] F. E. Ames, L. A. Dvorak, “Turbulent Transport in Pin Fin Arrays: Experimental Data and Predictions,” Journal of Turbomachinery, 128(1), 71-81, 2005

[86] J. Armstrong, D. Winstanley, “A Review of Staggered Array Pin Fin Heat Transfer for Turbine Cooling Applications,” Journal of Turbomachinery, 110(1), 94-103, 1988

[87] Suh-Jenq Yang, “A Numerical Investigation of Heat Transfer Enhancement for Electronic Devices using an Oscillating Vortex Generator,” Numerical Heat Transfer, Part A-42, 269-284, 2002

[88] A. Korichi, L. Oufer, “Heat Transfer Enhancement in Oscillatory Flow in Channel with Periodically Upper and Lower Wall Mounted Obstacles,” International Journal of Heat and Fluid Flow, 28(5), 1003-1012, 2007

[89] M. E. Lyall, K. A. Thole, A. Kohli, A. A. Thrift, “Heat Transfer from Low Aspect Ratio Pin Fins,” Journal of Turbomachinery, 133(1), 011001(1-10), 2010

[90] S. V. Garimella, P. A. Eibeck, “Heat Transfer Characteristics of an Array of Protruding Elements in Single Phase Forced Convection,” International Journal of Heat and Mass Transfer, 33 (12), 2659-2669, 1990

[91] K. Azar, C. D. Mandrone, “Effect of Pin Fin Density of the Thermal Performance of Unshrouded Pin Fin Heat Sinks,” Journal of Electronic Packaging ,116(4), 306-309, 1994

[92] M. Liu, D. Liu, S. Xu, Y. Chen, “Experimental Study on Liquid Flow and Heat Transfer in Micro Square Pin Fin Heat Sink,” International Journal of Heat and Mass Transfer, 54(25-26), 5602-5611, 2011

[93] S. Y. Won, G. I. Mahmood, P. M. Ligrani, “Spatially-Resolved Heat Transfer and Flow Structure in a Rectangular Channel with Pin Fins,” International Journal of Heat and Mass Transfer, 47(8-9), 1731-1743, 2004

[94] E. D. Larson, E. M. Sparrow, “Performance Comparisons among Geometrically different Pin-Fin Arrays situated in an Oncoming Longitudinal Flow,” International Journal of Heat and Mass Transfer, 25(5), 723-725, 1982

[95] S. A. Lawson, A. A. Thrift, K. A. Thole, A. Kohli, “Heat Transfer from Multiple Row Arrays of Low Aspect Ratio Pin Fins,” International Journal of Heat and Mass Transfer, 54(17-18), 4099-4109, 2011

[96] M. A. Tahat, R. F. Babus'Haq, S. D. Probert, "Forced Steady-State Convections from Pin Fin Arrays," Applied Energy 48, 335-351, 1994

[97] C. Wang, Y. Yu, T. Simon, T. Cui, "Microfabrication of Short Pin Fins on Heat Sink Surfaces to augment Heat Transfer Performance," Itherm-2012 Paper no. 2012_3050

[98] Huang L., Agrawal S., Simon T., Zhang M., Yeom T., North M., Cui T., "Fluid damping and power consumption of active devices used in cooling electronics," IMECE 2012-88627, Houston, USA, November 2012

[99] S. Agrawal, L. Huang, T. Simon, M. North, T. Cui, "Effects of Channel Aspect Ratio on Convective Heat Transfer in an Electronics Cooling Heat Sink having Agitation and Fan Induced Throughflow," ASME Summer Heat Transfer Conference-17182, Minneapolis, USA, July 2013

[100] Hugh W. Coleman, W. Glenn Steele, "Experimentation and Uncertainty Analysis for Engineers", Second Edition, John Wiley & Sons, Inc., New Jersey, 1999

[101] Frank Incropera, David DeWitt, Theodore Bergman, Adrienne Lavine, "Fundamentals of Heat and Mass Transfer", Fifth Edition, John Wiley & Sons, New Jersey, 2007

[102] J. P. Holman, "Heat Transfer", Eighth Edition, McGraw Hill, Inc., New York, 1997

[103] W. Kays, M. Crawford, B. Weigand, "Convective Heat and Mass Transfer", Fourth Edition, Mc Graw Hill, International Edition, 2005